Karlsruher Institut für Technologie

Schriftenreihe
Kontinuumsmechanik im Maschinenbau

19

Hannes Erdle

Modeling of Dislocation - Grain Boundary Interactions in Gradient Crystal Plasticity Theories

KIT Scientific Publishing

Hannes Erdle

Modeling of Dislocation - Grain Boundary Interactions in Gradient Crystal Plasticity Theories

Schriftenreihe
Kontinuumsmechanik im Maschinenbau
Band 19

Karlsruher Institut für Technologie (KIT)
Institut für Technische Mechanik
Bereich Kontinuumsmechanik

Hrsg. Prof. Dr.-Ing. habil. Thomas Böhlke

Eine Übersicht aller bisher in dieser Schriftenreihe erschienenen Bände finden Sie am Ende des Buchs.

Modeling of Dislocation - Grain Boundary Interactions in Gradient Crystal Plasticity Theories

by
Hannes Erdle

KIT Scientific Publishing

Karlsruher Institut für Technologie
Institut für Technische Mechanik
Bereich Kontinuumsmechanik

Modeling of Dislocation - Grain Boundary Interactions in Gradient Crystal Plasticity Theories

Zur Erlangung des akademischen Grades eines Doktor-Ingenieurs von der KIT-Fakultät für Maschinenbau des Karlsruher Instituts für Technologie (KIT) genehmigte Dissertation

von Hannes Erdle, M.Sc.

Tag der mündlichen Prüfung: 29. März 2022
Hauptreferent: Prof. Dr.-Ing. Thomas Böhlke
Korreferent: Prof. Dr.-Ing. Samuel Forest

Impressum

Scientific Publishing

Karlsruher Institut für Technologie (KIT)
KIT Scientific Publishing
Straße am Forum 2
D-76131 Karlsruhe

KIT Scientific Publishing is a registered trademark of Karlsruhe Institute of Technology.
Reprint using the book cover is not allowed.

www.ksp.kit.edu

Print on Demand 2022 – Gedruckt auf FSC-zertifiziertem Papier

ISSN 2192-693X
ISBN 978-3-7315-1196-0
DOI 10.5445/KSP/1000146388

Zusammenfassung

Die Formulierung und Implementierung neuartiger Materialmodelle auf der Mikroskala polykristalliner Materialien, z.B., kubisch flächenzentrierte Metalle, gibt ein tiefgründiges Verständnis inner- und interkristalliner Effekte. Dies erlaubt eine genauere Vorhersage physikalischer Effekte, welche das Verhalten des Materials auf der makroskopischen Skala beeinflussen. Im Kontext der erweiterten Kontinuumsmechanik wird eine Plastizitätstheorie basierend auf physikalischen Effekten von Versetzungen hergeleitet. Die erforderlichen Annahmen werden konstruiert um eine Theorie äquivalent zu einem Modellansatz basierend auf dem Prinzip virtueller Kräfte zu erhalten. Es wird eine orientierungsabhängige Fließbedingung der Korngrenzen entwickelt. Mittels einer analytischen Lösung eines dreiphasigen periodischen Laminates wird die Aufstauung der Versetzungen an Korngrenzen und der Transport über die Korngrenzen hinweg untersucht. Dies ist von besonderem Interesse bei der Untersuchung der plastischen Verformung von Metallen. Der sich ergebende Zusammenhang der Festigkeit und der Korngröße ist konsistent mit der Materialtheorie der Versetzungen. Im Gegensatz zum üblich verwendeten Ansatz der Fließbedingung der Korngrenzen besteht der neu entwickelte Ansatz die Konsistenzprüfung der Einkristalllösung für den Grenzfall aufeinandertreffender Gleitsysteme. Für missorientierte Körner ergibt sich ein diskontinuierlicher Verlauf der plastischen Abgleitung, was eine besondere Behandlung in der Anwendung mittels Finiter Elemente erfordert. Die Fließbedingung der Korngrenzen wird an scharfen Grenzschichten mittels diskontinuierlicher Ansatzfunktionen ausgewertet. Hierfür

wird ein physikalisch vereinfachtes, numerisch effizientes Modell unter Annahme großer Deformationen eingeführt. Um die weitreichenden Interaktionen der Versetzungen zu erfassen, enthält das Modell eine Gradientenspannung, welche auf den Gradienten der akkumulierten plastischen Abgleitung beschränkt ist. Es wird ein Ansatz formuliert um den rechnerischen Nutzen akkumulierter Feldvariablen in einem physikalisch motivierten Framework basierend auf dem Transport von Versetzungen aufrecht zu erhalten. Mittels anteiliger Verteilung des planaren Gradienten der akkumulierten plastischen Abgleitung auf die einzelnen Gleitsysteme wird ein numerisch effizientes Framework für die mechanismusbasierte Modellierung der Kristallplastizität konstruiert. Der Einfluss der Modellparameter auf die mechanische Antwort einer Laminatstruktur und einer Faser-Matrix Struktur wird in dreidimensionalen Finiten Elemente Simulationen untersucht. Die sich ergebenden Verteilungen der plastischen Abgleitung und der Versetzungsdichte sind konsistent mit experimentellen Untersuchungen und zeigen die Notwendigkeit auf, Energieterme und Fließregeln basierend auf Versetzungstheorien für die Modellierung der Interaktionen von Versetzungen und Korngrenzen zu nutzen.

Summary

For polycrystalline materials, e.g., face-centered cubic metals, the formulation and implementation of novel material models on the microscale gives a deeper understanding of inner- and inter-crystalline effects. This allows more precise prediction of physical effects which influence the material on the macroscopic scale. A physically-based dislocation theory of plasticity is derived within an extended continuum mechanical context. The required assumptions are constructed in order to obtain an equivalence to a model approach based on the principle of virtual power. An orientation dependent grain boundary flow rule is introduced. With an analytical solution of a three-phase periodic laminate the dislocation pile-up at grain boundaries and transmission through the grain boundaries is investigated, which is of special interest during the plastic deformation of metal materials. The observed dependence of the material strength on the grain size is consistent with underlying dislocation theories. In contrary to the common approach of grain boundary modeling the introduced grain boundary flow rule passes the single crystal consistency check for the limit case of coinciding slip systems. For misaligned grains a discontinuous slip distribution is obtained, which requires special treatment in the finite element application. The grain boundary flow rule is evaluated at sharp interfaces using discontinuous trial functions. Hereby, a physically simplified, numerically efficient approach is introduced in the finite strain setting. The model is restricted to one gradient-stress, associated with the gradient of the accumulated plastic slip, in order to account for long range dislocation interactions. An approach is

formulated in order to regain the computational benefit of accumulated plastic field variables within a physically motivated framework based on dislocation transport. By prorating the in-plane gradient of the accumulated plastic slip on the individual slip systems a numerically efficient framework for mechanism based modeling of crystal plasticity is constructed. The influence of model parameters on the mechanical response of a laminate grain structure and a fiber-matrix composite material is investigated in three-dimensional finite element simulations. The evolving distributions of plastic slip and dislocation density are consistent to experimental observation and show the importance of energy expressions and flow rules based on underlying dislocation theories for the modeling of dislocation-grain boundary interactions.

Acknowledgments

First of all, I would like to express my gratitude to Prof. Thomas Böhlke for offering me the position as an academic employee, for the supervision of my doctoral thesis and for all the support during the last years. Furthermore, I would like to thank Prof. Samuel Forest for co-advising this work, and for the offer of the research stay at Mines ParisTech including all the helpful discussions.

I also would like to thank all my colleagues at the Institute of Engineering Mechanics for the pleasant working environment, Nicola Simon from IAM-WK for the collaborations and Katrin Darscheid who supported my work for the present thesis.

Wholeheartedly, I want to thank my mother Gerlinde, my sister Kathrina, as well as Bernd and Kai for their encouragement and support. I would like to express my appreciation and gratitude to my friends Sophie and Simon who have always been a major source of cheerfulness when things would get a bit discouraging.

Finally, I would like to acknowledge the support by the German Research Foundation (DFG) within the projects 'Process Chains in Sheet Metal Manufacturing' of the DFG Research Group 1483, 'Dislocation based Plasticity' of the DFG Research Group 1650, 'Targeted Use of Forming Induced Residual Stresses in Metal Components' of the DFG Priority Programme SPP 2013, as well as the support by the state of Baden-Württemberg through bwHPC.

Karlsruhe, May 2022 Hannes Erdle

Contents

Chapter 1

Introduction

1.1 Motivation and research objectives

In this work the dislocation-induced plastic deformation of polycrystalline face-centered cubic (FCC) metals is considered. During the plastic deformation dislocations arise inside the bulk material and are transported on slip systems through the inner crystalline structure. The transport of dislocations, however, is hindered by the presence of grain boundaries (GBs). The pile-up of dislocations at and their transition across GBs has a significant impact on the overall material behavior. Therefore, the modeling of the dislocation-GB interactions is of utmost interest. Discrete dislocation dynamics or molecular dynamics simulations can be performed to investigate the movement of dislocations and interactions of dislocations with obstacles or with each other. For the application of polycrystalline structures, however, these methods are not applicable due to the high computational cost. In a continuum mechanical approach plastic slips, which result from the accumulation of several gliding dislocations, are considered. In crystal plasticity frameworks the mechanical behavior of the material is modeled with the construction of constitutive laws for the evolution of plastic slips based on underlying dislocation theories.

Classical continuum theories, however, fail to reproduce dependency of the material strength on the grain size, which is observed experimen-

tally for polycrystalline materials. A phenomenological approach is given by the introduction of a grain size dependency of the slip system yield strength, i.e., the stress which is required to act on a slip system for the activation of plastic slip evolution. As concluded by Zhu et al. (2008), however, each of these models explains size effects in different strain regions, under different initial conditions and for different deformation mechanisms. In order to model a physically based size-dependent behavior of polycrystalline metallic materials, the plastic slips are introduced as additional degrees of freedom (DOF). A close connection exists between the gradient of plastic slip and the density of geometrically necessary dislocations (GND), cf. Ashby (1970). Since the early work of Aifantis (1987) many gradient plasticity frameworks have been developed. The formulation of models which are optimal with regard to the dispute between physical correctness and implementability is an active field of current research. Besides applications in finite element (FE) simulations analytical solutions can be constructed to clarify the influence of energy expressions and dislocation-GB interactions.

Within the thesis, several originalities were developed, whereas the main highlights are:

- The construction of a gradient crystal plasticity framework based on an extended balance equation. The comparison to a model approach based on the principle of virtual power is performed. The required assumptions are formulated in order to obtain an equivalence between both approaches.
- The formulation of a GB flow condition based on the geometric dislocation tensor. The flow condition couples plastic slips at GBs by a misorientation function of adjacent slip system. The flow condition describes the orientation dependent resistance of a GB. This allows to model the pile-up of dislocations and the activation of GB slip, i.e., the transmission of dislocations across the GB.

- The construction of an analytical solution for the distribution of plastic slip and the displacement field of a periodic three-phase laminate structure. The analytical solution is used for a comparison of the GB flow condition approach to a common approach based on the assumption of independent slips at the GB. The analytical solution gives an insight into the GB behavior for misaligned grains, the consistency check for the limiting case of a vanishing misorientation and the investigation of size effects.
- The application of shape function enrichment in the FE implementation of gradient crystal plasticity frameworks. This method allows for discontinuous solution fields at interfaces and is well-suited for the modeling of dislocation transmission across GBs.
- The extension of a numerically efficient gradient crystal plasticity framework based on the accumulated plastic slip to finite strains and discontinuous solution fields. The model accounts for the pile-up of dislocations at GBs and the transmission of dislocations across GBs by a GB energy dependent on the jump and mean value of plastic slip. The FE implementation provides insight into the GB behavior of a periodic laminate structure and the investigation of material parameter influences.
- The development and implementation of a finite strain gradient crystal plasticity framework that accounts for a semi-phenomenological dislocation transport mechanism. A physically motivated dislocation transport equation is constructed while preserving the computational benefit of accumulated field variables. The model is based on a dislocation energy which is obtained by a statistical theory of dislocations. This allows for a semi-phenomenological treatment of dislocations within the context of gradient crystal plasticity.

1.2 Outline of the thesis

In Chapter 2 an introduction of dislocations and dislocation-based plasticity is given. Fundamental informations on the origin of dislocations and strengthening mechanisms associated with dislocation multiplication and dislocation-GB interactions are briefly presented.

In Chapter 3, fundamentals of classical continuum mechanics such as kinematics and basic assumptions of small strain and finite strain frameworks are presented. Based on mechanical and thermodynamical balance relations for a material divided by a singular surface the Clausius-Duhem inequality is obtained for regular and singular points.

This provides the basics for Chapter 4, in which a gradient crystal plasticity theory is derived by an extension of balance equations. Potential relations and boundary conditions for both, bulk material and GBs, are obtained. A comparison to a model approach based on the principle of virtual power is made. Simplifying assumptions and their implication on the Clausius-Duhem inequality and the bulk material flow rule are presented in order to obtain consistent frameworks.

Chapter 5 introduces a GB flow condition approach. The GB energy is introduced as a function of the geometric dislocation tensor in order to account for the misorientation of adjacent slip systems and dislocation transmission across GBs. An analytical solution for the distribution of plastic slip and the displacement field of a periodic laminate is derived. For simplicity small strains and single slip is considered. The GB flow condition approach is compared with a commonly used approach for a varying grain misorientation angle. Consistency checks are made for the limiting case of vanishing grain misorientation. In addition, the influence of the grain size is investigated.

In Chapter 6 a finite strain gradient crystal plasticity theory is presented, which includes a FE application based on a micromorphic approach. In order to reduce the computational cost the model is restricted to

one gradient-stress associated with the gradient of the accumulated plastic slip. The Clausius-Duhem inequality and flow rules for the bulk material and GBs are derived. Details on the FE implementation of a discontinuous plastic slip field are presented. The influence of grain misorientation, grain size and material parameters are discussed for a periodic laminate microstructure.

Chapter 7 introduces a finite strain gradient crystal plasticity framework that accounts for a semi-phenomenological dislocation transport mechanism. Besides the accumulated plastic slip an accumulated density of dislocations is introduced as an additional degree of freedom. Flow rules for the bulk material and the GBs are derived. Three-dimensional FE simulations of a periodic laminate microstructure and a fiber-matrix composite material are performed.

A summary in Chapter 8, featuring an outlook based on remaining open questions from the work at hand, concludes the thesis.

1.3 Frequently used acronyms, symbols, and operators

Acronyms

BCC	Body-centered cubic
DOF	Degree of freedom
FCC	Face-centered cubic
FE	Finite element
GB	Grain boundary

GND	Geometrically necessary dislocations
SSD	Statisticall stored dislocations

Latin letters

$a, b, A, B, \mathcal{D}, \ldots$	Scalar quantities
$\boldsymbol{u}, \boldsymbol{v}, \boldsymbol{w}, \ldots$	First-order tensors
$\boldsymbol{A}, \boldsymbol{B}, \boldsymbol{C}, \ldots$	Second-order tensors
$\mathbb{A}, \mathbb{B}, \mathbb{C}, \ldots$	Fourth-order tensors
A_γ	Micro-inertia force
b	Absolute value of the Burgers vector
b_γ	Micro-body force
$\boldsymbol{b}$	Body force
B	Finite element shape function derivative
C^{++}, C^{--}	Intra-grain interaction moduli
C^{+-}	Inter-grain interaction moduli
$\mathbb{C}$	Fourth-order elastic stiffness tensor
$\boldsymbol{d}_\alpha$	Slip direction of slip system α
$\mathcal{D}$	Dissipation
$\mathcal{D}_{\mathrm{red}}$	Reduced dissipation
e	Specific internal energy
$\boldsymbol{e}_1, \boldsymbol{e}_2, \boldsymbol{e}_3$	Unit vector in x-,y- and z-direction of a Cartesian coordinate system
$\boldsymbol{E}_{\mathrm{e}}$	Green strain tensor

$\boldsymbol{F}$	Deformation gradient
$\boldsymbol{F}_\mathrm{e}, \boldsymbol{F}_\mathrm{p}$	Elastic and plastic part of $\boldsymbol{F}$
$\boldsymbol{G}$	Geometric dislocation tensor
H_χ	Penalty modulus
$\boldsymbol{H}$	Displacement gradient
$\boldsymbol{H}_\mathrm{e}, \boldsymbol{H}_\mathrm{p}$	Elastic and plastic part of $\boldsymbol{H}$
$\boldsymbol{I}$	Second-order identity tensor
$\mathbb{I}$	Fourth-order identity tensor
k	Mean curvature
K_0	Isotropic energy parameter
K_c	Correlation energy parameter
K_g	Defect energy parameter
K_j	Grain boundary energy parameter associated with the jump of plastic slip
K_m	Grain boundary energy parameter associated with the mean value of plastic slip
K_s	Dislocation self energy parameter
$\boldsymbol{L}$	Velocity gradient
$\boldsymbol{L}_\mathrm{p}$	Distortion rate tensor
$\boldsymbol{M}_\alpha$	Schmid tensor of slip system α
$\boldsymbol{M}^\mathrm{s}_\alpha$	Symmetric Schmid tensor of slip system α
$\boldsymbol{n}$	Normal vector
$\boldsymbol{n}_\alpha$	Slip plane normal vector of slip system α
N	Finite element shape function
p	Slip rate sensitivity parameter

$\breve{p}$	Generalized relative stress
$\boldsymbol{P}_\alpha$	Projector of slip system α
$\boldsymbol{P}_\mathcal{S}$	Projector of interface $\mathcal{S}$
$\mathcal{P}_\mathrm{ext}$	External power
$\mathcal{P}_\mathrm{int}$	Internal power
$\boldsymbol{q}$	Heat flux vector
$\boldsymbol{Q}_\vartheta$	Orthogonal rotation matrix with angle ϑ
$\boldsymbol{Q}^{+-}$	Inter-grain rotation matrix
r	Residuals
$\boldsymbol{R}$	Rigid body rotation tensor
$\boldsymbol{S}$	Piola-Kirchhoff stress
$\boldsymbol{s}$	Dislocation direction line
$\boldsymbol{S}_\mathrm{e}$	Second Piola-Kirchhoff stress
t	Time
$\boldsymbol{t}$	Stress vector
$\bar{\boldsymbol{t}}$	Surface traction
$\boldsymbol{u}$	Displacement field
$\boldsymbol{U}$	Rigid stretch tensor
$\boldsymbol{v}$	Velocity field
$\boldsymbol{x}$	Position vector of a material point in the current configuration
$\boldsymbol{X}$	Position vector of a material point in the reference configuration

Greek letters

α	Slip system index
β_α	Derivative of hardening energy by plastic slip of slip system α
β_ρ	Derivative of hardening energy by dislocation density
γ_α	Plastic slip of slip system α
$\gamma_{\mathrm{ac}\alpha}$	Accumulated plastic slip of slip system α
γ_{ac}	Accumulated plastic slip
$\breve{\gamma}_{\mathrm{ac}}$	Micromorphic accumulated plastic slip
$\boldsymbol{\varepsilon}$	Infinitesimal strain tensor
$\boldsymbol{\varepsilon}_{\mathrm{e}}, \boldsymbol{\varepsilon}_{\mathrm{p}}$	Elastic and plastic part of $\boldsymbol{\varepsilon}$
ζ_α	Continuous plastic slip of slip system α
η	Specific entropy
θ	Temperature
Θ_0	Initial hardening modulus
Θ_{inf}	Saturation hardening modulus
ϑ	Orientation angle of single slip system
κ	Grain boundary strength
λ_α	Plastic slip parameter of slip system α
$\dot{\lambda}_0$	Reference shear rate
λ_Θ	Thermal conductivity
μ	Shear modulus
$\boldsymbol{\nu}$	Dislocation velocity

$\bar{\boldsymbol{\nu}}$	Coarse grained dislocation velocity
ξ_0	Grain boundary misorientation parameter
$\boldsymbol{\xi}$	Vector-valued microstress
Ξ	Microscopic surface traction
$\Xi_\mathrm{j}, \Xi_\mathrm{m}$	Microscopic surface traction work conjugated to the jump and mean value of plastic slip
π	Scalar-valued microstress
Π	Microtraction
ρ	Density of dislocations
$\bar{\rho}$	Coarse grained density of dislocations
ρ^G	Density of geometrically necessary dislocations
ρ_ac	Accumulated density of dislocations
ρ_ini	Initial density of dislocations
ϱ	Mass density
$\boldsymbol{\sigma}$	Cauchy stress tensor
τ	Resolved shear stress
τ_0	Initial critical resolved shear stress
τ_inf	Saturation stress
τ_D	Drag stress
φ	Yield function
ψ	Specific free energy
ψ_c	Specific correlation energy
ψ_e	Specific elastic energy
ψ_g	Specific defect energy

ψ_{h}	Specific hardening energy
ψ_{s}	Specific dislocation self energy
ψ_{χ}	Specific numerical penalty energy
ω	Heat supply density

Operators

$\lvert\cdot\rvert$	Absolute value of a scalar quantity
$\lVert\cdot\rVert$	Norm of a vector or tensor
$(\cdot)_0$	Lagrangian description of a quantity
$\langle\cdot\rangle_{\mathrm{c}}$	Coarse graining of a quantity
$(\cdot)_{\mathcal{S}}$	Quantity with respect to the interface $\mathcal{S}$
$\llbracket\cdot\rrbracket$	Jump of a quantity across an interface
$\langle\!\langle\cdot\rangle\!\rangle$	Mean value of a quantity across an interface
$(\cdot)^+$	Left-hand limit of a quantity at an interface
$(\cdot)^-$	Right-hand limit of a quantity at an interface
$\{\cdot\}$	Macaulay bracket: ramp function of a quantity
$\tilde{(\cdot)}$	Quantity in local coordinate system
$\dot{(\cdot)}$	Material time derivative of a quantity
$\boldsymbol{A}\cdot\boldsymbol{B}$	Dot product of two tensors $\boldsymbol{A},\boldsymbol{B}$
$\boldsymbol{A}\otimes\boldsymbol{B}$	Dyadic product of two tensors $\boldsymbol{A},\boldsymbol{B}$
$\mathbb{C}=\boldsymbol{A}\square\boldsymbol{B}$	Box product of two tensors $\boldsymbol{A},\boldsymbol{B}$ with $(\boldsymbol{A}\square\boldsymbol{B})[\boldsymbol{C}]=\boldsymbol{ACB}$
$\boldsymbol{AB}$	Linear mapping of a second-order tensor

$\boldsymbol{A} = \mathbb{C}\,[\boldsymbol{B}]$	Linear mapping of a second-order tensor by a fourth-order tensor
$\boldsymbol{A}^{-1}$	Inverse of a tensor $\boldsymbol{A}$
$\boldsymbol{A}^{\mathsf{T}}$	Transpose of a tensor $\boldsymbol{A}$
$\cos(\cdot)$	Cosine of a scalar quantity
$\det(\cdot)$	Determinant of a tensor
$\delta(\cdot)$	Variation of a quantity
$\partial(\cdot)/\partial x$	Partial derivative of a quantity w.r.t., e.g., x
$\mathrm{d}(\cdot)/\,\mathrm{d}x$	Total derivative of a quantity w.r.t., e.g., x
$\mathrm{div}\,(\cdot)$	Eulerean divergence of a vector or tensor
$\mathrm{div}_{\mathcal{S}}\,(\cdot)$	Surface divergence of a vector or tensor
$\mathrm{Div}\,(\cdot)$	Lagrangian divergence of a vector or tensor
$\ln(\cdot)$	Logarithm of a scalar quantity
$\mathrm{grad}\,(\cdot)$	Eulerean gradient of a quantity
$\mathrm{grad}_{\mathcal{S}}\,(\cdot)$	Surface gradient of a quantity
$\mathrm{Grad}\,(\cdot)$	Lagrangian gradient of a quantity
$\mathrm{Grad}^{\mathrm{p}}\,(\cdot)$	Lagrangian in-plane gradient of a quantity
$\mathrm{sgn}\,(\cdot)$	Sign of a scalar quantity
$\sin(\cdot)$	Sine of a scalar quantity
$\mathrm{sym}\,(\cdot)$	Symmetric part of a tensor
$\mathrm{tr}(\cdot)$	Trace of a tensor

Chapter 2

Introduction to dislocations

2.1 Dislocation-based plasticity

This chapter serves as an introduction to dislocations and dislocation-based plasticity. It gives a short overview of well-established theories and does not contain new findings. For a more detailed introduction to dislocations it is referred to Hull and Bacon (2011).

An important characteristic of a dislocation is the Burgers vector. A Burgers vector can be constructed by creating a closed atom-to-atom loop around a dislocation. After reconstructing the same loop in a dislocation free crystal structure, the circuit shows a gap. The vector which results by completing the circuit, called Burgers vector $\boldsymbol{b}$, determines the magnitude and orientation of the dislocation. With the Burgers vector and the dislocation direction line $\boldsymbol{s}$ it is possible to distinguish between an edge dislocation ($\boldsymbol{s} \perp \boldsymbol{b}$) and a screw dislocation ($\boldsymbol{s} \parallel \boldsymbol{b}$). A graphical illustration of an edge dislocation in a crystal structure, marked by the symbol "$\perp$" is shown in Fig. 2.1.

The discovery of dislocations by Orowan (1934), Polanyi (1934) and Taylor (1934) provides an explanation for the process of plastic deformation in crystals. Experimental investigations of Schmid and Boas (1935) show that due to dislocation motion the critical resolved shear stress of single crystals is found to be considerably smaller than the theoretical strength. The motion of dislocations can be classified into

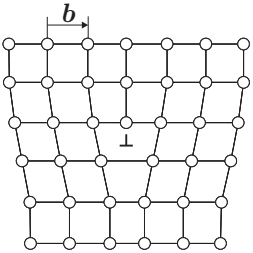

Figure 2.1: Graphical illustration of an edge dislocation with Burgers vector $\boldsymbol{b}$.

conservative dislocation glide and non-conservative dislocation climb. Gliding of dislocations describes the motion on specific planes, which depend on the crystal structure of the material. Climb, in contrary, describes the motion out of these planes. In this work the focus is on dislocation glide. Glide of many dislocations results in slip, which is the most common manifestation of plastic deformation in crystalline solids, cf. Hull and Bacon (2011). The slip planes in FCC metals, in contrary to body-centered cubic (BCC) metals, are well defined as planes with the highest density of atoms. The direction of slip is the direction in which the atoms are most closely spaced. FCC crystals have four slip planes with three slip directions in each plane, and therefore twelve slip systems. Each slip system is characterized by the corresponding Schmid tensor $\boldsymbol{M}_\alpha = \boldsymbol{d}_\alpha \otimes \boldsymbol{n}_\alpha$, with the slip plane normal vector $\boldsymbol{n}_\alpha$ and the slip direction $\boldsymbol{d}_\alpha$, where $\alpha \in \{1, \dots, N\}$ denotes the slip system index and N is the number of slip systems. The two unit vectors are orthogonal to each other, i.e., $\boldsymbol{d}_\alpha \cdot \boldsymbol{n}_\alpha = 0$. In Appendix A.1 the slip system convention for FCC, which is used in this work, is given. The projection of the Cauchy stress tensor $\boldsymbol{\sigma}$ to the slip system α is introduced as the resolved shear stress

$$\tau_\alpha \coloneqq \boldsymbol{\sigma} \cdot \boldsymbol{M}_\alpha \,. \tag{2.1}$$

As soon as the resultant shear stress reaches a critical value τ_c plastic slip occurs. The Orowan equation for plastic slip

$$\dot{\gamma}_\alpha = \rho_\alpha b \nu_\alpha \tag{2.2}$$

gives a relation between the rate of plastic slip $\dot{\gamma}_\alpha$ and the average glide velocity of dislocations ν_α in the slip system α. Hereby, b denotes the absolute value of the burgers vector, i.e., $b = \|\boldsymbol{b}\|$ and ρ_α denotes the density of dislocations in the slip system α.

2.2 Dislocation strengthening mechanisms

Polycrystals consist of many grains with differently oriented slip systems. Hence plastic flow first occurs in the grain with the slip system which can resolve the most shear stress. This leads to an inhomogeneous plastic material behavior. Because the cohesion of the material still has to be guaranteed, the formation of GND, as illustrated in Fig. 2.2, occurs. Ensuing from the deformation of a polycrystal (a) where each grain behaves independently, gaps and overlaps would emerge (b). Due to dislocations these defects are compensated by shear (c) (top) or deformations normal to the GB (c) (bottom). By combining these processes the counteract of all possible failures is enabled (d). The interfaces between regions of different crystal orientations impede the motion of dislocations. The resistance of a GB against the transmission of dislocations is strongly influenced by the mismatch of adjacent slip systems. For an overview of basic dislocation mechanisms near GBs and transmission of dislocations across GBs it is referred Chapter 5 as well as to the review article of Bayerschen et al. (2016). Due to the pile-up of dislocations at GBs the grain size influences the mechanical

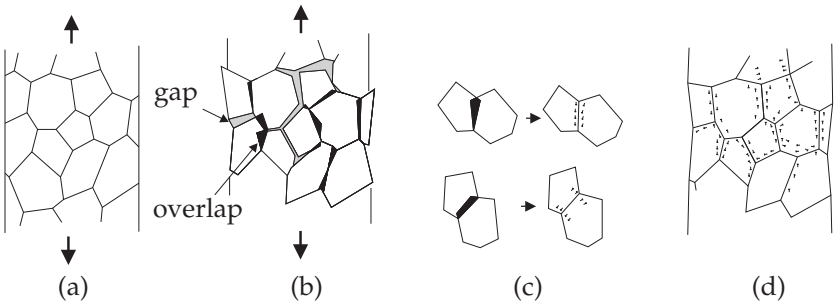

Figure 2.2: Illustration of the origin of GND, cf. Ashby (1970).

response of polycrystalline materials. The Hall-Patch relation

$$\tau_c - \tau_0 \propto \frac{1}{\sqrt{d}}, \tag{2.3}$$

cf. Hall (1951), relates the difference between the yield stress τ_c and the yield stress of an undeformed single crystal τ_0 to the grain size d. This relation, however, is only a manifestation of the general size effect and can not be explained by a variety of theories found in literature, as discussed by Li et al. (2016).

On the contrary to GND, statistically stored dislocations (SSD) are not required for a cohesion of the crystal and originate at various locations inside each grain. Essential origination processes are an unideal crystal growth and the Frank-Read-Mechanism illustrated in Fig. 2.3. A dislocation line lies in a slip plane, is pinned at both ends by two fixing points A and B, e.g., by crystal defects (a) and bows out due to an applied resolved shear stress τ. The radius of curvature R decreases as τ increases until the minimum value of R is reached (b). As the line continues to expand, the dislocation becomes unstable and R increases (c). Consequently, this behavior leads to an annihilation of the opposing segments (d, e). The result is a large outer dislocation loop,

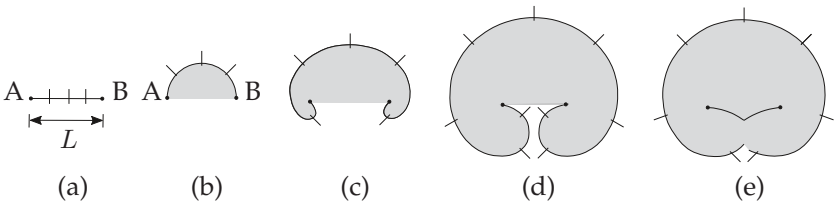

Figure 2.3: Illustration of the Frank-Read mechanism, cf. Hull and Bacon (2011).

which continues to expand, and a regenerated inner dislocation line, which repeats the process. The necessary stress for this Frank-Read mechanism is given with shear modulus G by

$$\tau_{\mathrm{c}} = \frac{aGb}{L}\,, \tag{2.4}$$

cf. Hull and Bacon (2011), where L denotes the spacing between the fixing points A and B and $a \approx 0.5$ denotes a material constant. A special case of the treatment above is the phenomenon of work hardening. Here, the pinning points are forest dislocations and the relevant size parameter is given by their average spacing $L = 1/\sqrt{\rho}$, cf. Arzt (1998). The classical Taylor equation for work hardening is obtained

$$\tau_{\mathrm{c}} = aGb\sqrt{\rho}\,. \tag{2.5}$$

Both types of dislocations, GND and SSD, influence the material behavior of polycrystals. At first an overview of classical continuum mechanics theory for the local continuum representation of dislocation-based plasticity is given.

Chapter 3

Classical continuum mechanics theory

3.1 Introduction and motivation

The critical resolved shear stress evolves during the plastic deformation process of the crystal lattice due to work-hardening. The work-hardening of single-crystals describes the strengthening of the material due to the production and annihilation of dislocations and is often formulated by a constitutive relation between the critical resolved shear stress and scalar-valued hardening quantities, cf. , e.g., Bishop and Hill (1951); Hill (1966). With the formulation of constitutive laws for the evolution of the plastic slips, plastic deformation of polycrystalline structures can be modeled. This classical crystal plasticity approach is presented in the following. Hereby, mechanical and thermodynamical balance relations are introduced in order to describe the motion of a material body in time and the evolution of the associated mechanical fields.

3.2 Kinematics and basic assumptions

The motion of a material body $\mathcal{V} \in \mathbb{R}^3$ is considered. As seen in Fig. 3.1, the position of a material point can be characterized by the vector $\boldsymbol{X}$

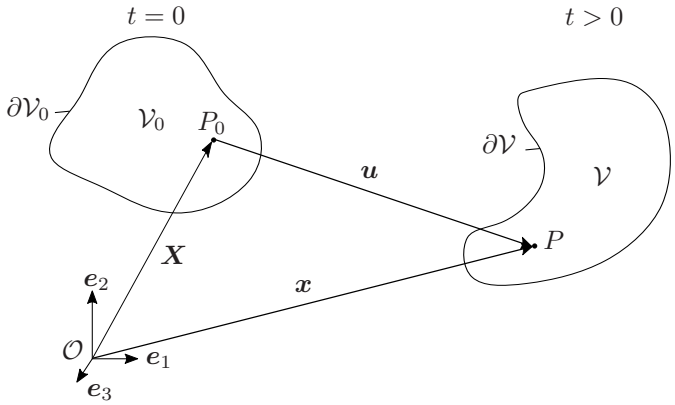

Figure 3.1: Material body in the reference and the current placement.

in reference description (time: $t = 0$), or by the vector $\boldsymbol{x}$ in spatial description (time: $t > 0$). With the introduction of the deformation $\boldsymbol{\chi}$ the current position of a material point can be described as a function of its reference position upon neglecting phenomena like, e.g., cracks

$$\boldsymbol{x} = \boldsymbol{\chi}(\boldsymbol{X}, t)\,. \tag{3.1}$$

It is assumed that the function $\boldsymbol{\chi}$ is invertible and twice continuously differentiable. The material time derivative of the motion represents the velocity $\boldsymbol{v}(\boldsymbol{X}, t) = \boldsymbol{\chi}(\dot{\boldsymbol{X}}, t)$. For a general field quantity $\psi(\boldsymbol{x}, t)$ the material time derivative is given as

$$\dot{\psi}(\boldsymbol{x}, t) = \frac{\partial \psi(\boldsymbol{x}, t)}{\partial t} + \frac{\partial \psi(\boldsymbol{x}, t)}{\partial \boldsymbol{x}} \cdot \boldsymbol{v}(\boldsymbol{x}, t)\,. \tag{3.2}$$

The displacement of a material point results as the difference of its current position and reference position

$$\boldsymbol{u}(\boldsymbol{X}, t) = \boldsymbol{\chi}(\boldsymbol{X}, t) - \boldsymbol{X}\,. \tag{3.3}$$

The displacement gradient reads

$$\boldsymbol{H} = \mathrm{Grad}\,(\boldsymbol{u}(\boldsymbol{X},t)) = \frac{\partial \boldsymbol{u}(\boldsymbol{X},t)}{\partial \boldsymbol{X}}\,. \tag{3.4}$$

In the following, dependencies of quantities are dropped due to better readability.

Small deformation setting

In the context of Chapter 4 and 5 only small deformations are considered. Frameworks extended to finite deformations are presented in Chapter 6 and 7. For a geometrically linear theory the norm of the displacement gradient has to fulfil the condition

$$\|\boldsymbol{H}\| \ll 1\,, \tag{3.5}$$

and occurring rotations have to be sufficiently small. Since only small deformations are considered in the following, there is no distinction between the reference configuration and the current configuration. The displacement gradient $\boldsymbol{H} = \mathrm{Grad}\,(\boldsymbol{u}) \approx \mathrm{grad}\,(\boldsymbol{u})$ is assumed to be additively decomposable into an elastic part $\boldsymbol{H}_\mathrm{e}$ and a plastic part $\boldsymbol{H}_\mathrm{p}$. As a result, the additive decomposition also applies to the infinitesimal strain tensor

$$\boldsymbol{\varepsilon} = \mathrm{sym}(\boldsymbol{H}) = \mathrm{sym}(\boldsymbol{H}_\mathrm{e}) + \mathrm{sym}(\boldsymbol{H}_\mathrm{p}) = \boldsymbol{\varepsilon}_\mathrm{e} + \boldsymbol{\varepsilon}_\mathrm{p}\,. \tag{3.6}$$

Constitutive equations are required which describe the material-specific response of the body, e.g., to an external force. For material modeling it is crucial to describe the relation between stresses and strains so that the deformation of this material can be calculated. The general linear elastic anisotropic Hooke's law

$$\boldsymbol{\sigma} = \mathbb{C}[\boldsymbol{\varepsilon}_\mathrm{e}] \tag{3.7}$$

connects the stresses and strains by a linear relationship. The stiffness matrix $\mathbb{C} = C_{ijkl}\boldsymbol{e}_i \otimes \boldsymbol{e}_j \otimes \boldsymbol{e}_k \otimes \boldsymbol{e}_l$ is a fourth-order tensor with 81 components. Under consideration of hyperelasticity, the following symmetries hold true. Due to the inherent symmetries of $\boldsymbol{\sigma}$ and $\boldsymbol{\varepsilon}$ the stiffness matrix has two sub-symmetries $C_{ijkl} = C_{jikl}$ and $C_{ijkl} = C_{ijlk}$. Regarding the anisotropic elastic case, the symmetry $C_{ijkl} = C_{klij}$ and one of the sub-symmetries imply that only 21 elastic coefficients of the stiffness matrix are independent. This number of independent coefficients can be further reduced by material symmetries.

Crystal plasticity frameworks are based on the assumption that plastic flow takes place by evolution of plastic slip on different slip systems. With the kinematical constitutive assumption

$$\boldsymbol{H}_{\mathrm{p}} = \sum_{\alpha=1}^{N} \gamma_\alpha \boldsymbol{M}_\alpha \,, \tag{3.8}$$

the evolution equation of the plastic strain $\boldsymbol{\varepsilon}_{\mathrm{p}}$ results in

$$\dot{\boldsymbol{\varepsilon}}_{\mathrm{p}} = \sum_{\alpha=1}^{N} \dot{\gamma}_\alpha \boldsymbol{M}^{\mathrm{s}}_\alpha \,, \tag{3.9}$$

where the symmetric part of the Schmid tensor $\boldsymbol{M}^{\mathrm{s}}_\alpha := \mathrm{sym}\,(\boldsymbol{M}_\alpha)$ is introduced. Based on the slip rate, the accumulated plastic slip on a slip system α is introduced as internal hardening variables by

$$\gamma_{\mathrm{ac}\alpha} = \int_0^t |\dot{\gamma}_\alpha| \, \mathrm{d}\tilde{t} \,. \tag{3.10}$$

Finite deformation setting

Based on the assumption of the existence of the plastic deformation $\boldsymbol{F}_{\mathrm{p}}^{-1} = \boldsymbol{P}$ as the material isomorphism between two elastic materials (cf. Bertram (2008)) the deformation gradient $\boldsymbol{F}$ is multiplicative decom-

posed into the elastic deformation gradient $\boldsymbol{F}_\mathrm{e}$ and the plastic deformation gradient $\boldsymbol{F}_\mathrm{p}$

$$\boldsymbol{F} = \mathrm{Grad}\,(\boldsymbol{\chi}) = \boldsymbol{F}_\mathrm{e}\boldsymbol{F}_\mathrm{p}\,. \tag{3.11}$$

The elastic deformation gradient $\boldsymbol{F}_\mathrm{e} = \boldsymbol{R}_\mathrm{e}\boldsymbol{U}_\mathrm{e}$ consists of the lattice stretch $\boldsymbol{U}_\mathrm{e} \in Psym$ and the mean lattice rotation $\boldsymbol{R}_\mathrm{e} \in Orth^+$ of the crystal lattice. The plastic deformation gradient $\boldsymbol{F}_\mathrm{p} \in Unim^+$ represents the distortion of the crystal lattice due to the formation and movement of dislocations. With the deformation gradient a material line element $\mathrm{d}\boldsymbol{x} = \boldsymbol{F}\,\mathrm{d}\boldsymbol{X}$, an area element $\mathrm{d}\boldsymbol{a} = \det(\boldsymbol{F})\boldsymbol{F}^{-\mathsf{T}}\,\mathrm{d}\boldsymbol{A}$ and a volume element $\mathrm{d}v = \det(\boldsymbol{F})\,\mathrm{d}V$ can be transformed from the reference placement (upper case letters) to the current placement (lower case letters), respectively.

Under the assumption of small elastic strains the St. Venant's law

$$\boldsymbol{S}_\mathrm{e} = \tilde{\mathbb{C}}[\boldsymbol{E}_\mathrm{e}] \tag{3.12}$$

is introduced for the second Piola-Kirchhoff stress $\boldsymbol{S}_\mathrm{e}$. Here, $\tilde{\mathbb{C}}$ denotes the elastic stiffness tensor in the intermediate configuration and

$$\boldsymbol{E}_\mathrm{e} = \frac{1}{2}\left(\boldsymbol{F}_\mathrm{e}^{\mathsf{T}}\boldsymbol{F}_\mathrm{e} - \boldsymbol{I}\right) \tag{3.13}$$

denotes the Green strain tensor. The relation of the second Piola-Kirchhoff stress in Eq. (3.12) and the Cauchy stress in Eq. (3.7) is given by $\boldsymbol{\sigma} = \det(\boldsymbol{F}_\mathrm{e}^{-1})\boldsymbol{F}_\mathrm{e}\boldsymbol{S}_\mathrm{e}\boldsymbol{F}_\mathrm{e}^{\mathsf{T}}$. The multiplicative decomposition of the deformation gradient results in the velocity gradient

$$\boldsymbol{L} = \mathrm{grad}\,(\boldsymbol{v}) = \dot{\boldsymbol{F}}_\mathrm{e}\boldsymbol{F}_\mathrm{e}^{-1} + \boldsymbol{F}_\mathrm{e}\dot{\boldsymbol{F}}_\mathrm{p}\boldsymbol{F}_\mathrm{p}^{-1}\boldsymbol{F}_\mathrm{e}^{-1}\,, \tag{3.14}$$

where the distortion rate tensor

$$\tilde{\boldsymbol{L}}_\mathrm{p} = \dot{\boldsymbol{F}}_\mathrm{p}\boldsymbol{F}_\mathrm{p}^{-1} = \sum_{\alpha=1}^{N} \dot{\gamma}_\alpha \tilde{\boldsymbol{M}}_\alpha \tag{3.15}$$

consists of slip rates $\dot{\gamma}_\alpha$ on individual slip systems. In Eq. (3.15) the Schmid tensor for the slip system α

$$\tilde{\boldsymbol{M}}_\alpha = \tilde{\boldsymbol{d}}_\alpha \otimes \tilde{\boldsymbol{n}}_\alpha \tag{3.16}$$

was introduced in the lattice space. From this, a push forward to the Eulerian form can be performed

$$\boldsymbol{M}_\alpha = \boldsymbol{F}_\mathrm{e} \tilde{\boldsymbol{d}}_\alpha \otimes \boldsymbol{F}_\mathrm{e}^{-\mathsf{T}} \tilde{\boldsymbol{n}}_\alpha \,. \tag{3.17}$$

3.3 Mechanical and thermodynamical balance relations

3.3.1 Motivation and mathematical preliminaries

In the following it is assumed, as illustrated in Fig. 3.2, that a material volume $\mathcal{V}$ is divided by a material singular surface $\mathcal{S}$ into two sub-volumes $\mathcal{V}^+$ and $\mathcal{V}^-$, i.e., $\mathcal{V} = \mathcal{V}^+ \cup \mathcal{V}^-$. The outer normal vector of the surfaces $\partial\mathcal{V}^+$ and $\partial\mathcal{V}^-$ is denoted by $\boldsymbol{n}$, while $\partial\mathcal{V} = \partial\mathcal{V}^+ \cup \partial\mathcal{V}^-$ holds true. The normal vector of the singular surface is denoted by $\boldsymbol{n}_\mathcal{S}$ and points from $\mathcal{V}^-$ towards $\mathcal{V}^+$. The line of intersection of $\mathcal{S}$ and $\partial\mathcal{V}$ is denoted by $\partial\mathcal{S}$ with outer normal vector $\boldsymbol{m}$. The jump of an arbitrary quantity a at a singular surface is defined as $\left[\!\left[a\right]\!\right] = a^+ - a^-$, where a^+ and a^- denotes the right-hand limit and the left-hand limit of a, respectively.

Divergence theorem

The divergence theorem can be used to transform a surface integral into a volume integral. For a material volume divided by a material singular

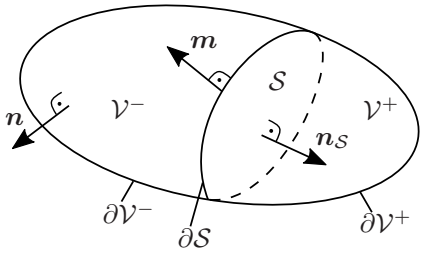

Figure 3.2: Material volume $\mathcal{V}$, separated by a material singular surface $\mathcal{S}$.

suface it reads

$$\int_{\partial\mathcal{V}} \boldsymbol{a}\cdot\boldsymbol{n}\,\mathrm{d}a = \int_{\mathcal{V}} \mathrm{div}\,(\boldsymbol{a})\;\mathrm{d}v + \int_{\mathcal{S}} \llbracket \boldsymbol{a} \rrbracket\cdot\boldsymbol{n}_{\mathcal{S}}\,\mathrm{d}a\,. \tag{3.18}$$

Transport theorems

The transport theorem specifies the time derivative of a volume integral of a bulk density $\Psi_{\mathcal{V}}$ in a time-dependent volume $\mathcal{V}=\mathcal{V}(t)$. In the presence of a material singular surface it reads

$$\frac{\mathrm{d}}{\mathrm{d}t}\int_{\mathcal{V}}\Psi_{\mathcal{V}}\,\mathrm{d}v = \int_{\mathcal{V}}\frac{\partial\Psi_{\mathcal{V}}}{\partial t}\,\mathrm{d}v + \int_{\partial\mathcal{V}}\Psi_{\mathcal{V}}\boldsymbol{v}\cdot\boldsymbol{n}\,\mathrm{d}a - \int_{\mathcal{S}}\llbracket\Psi_{\mathcal{V}}\rrbracket v_{\mathcal{S}}^{\perp}\,\mathrm{d}a\,, \tag{3.19}$$

where $v_{\mathcal{S}}^{\perp}=\boldsymbol{v}_{\mathcal{S}}\cdot\boldsymbol{n}_{\mathcal{S}}$ denotes the normal component of the velocity of the singular surface.

The transport theorem for a surface density $\Psi_{\mathcal{S}}$ in a time dependent material singular surface $\mathcal{S}=\mathcal{S}(t)$ is given in Slattery (1990) as

$$\frac{\mathrm{d}}{\mathrm{d}t}\int_{\mathcal{S}}\Psi_{\mathcal{S}}\,\mathrm{d}v = \int_{\mathcal{S}}\left(\dot{\Psi}_{\mathcal{S}} + \Psi_{\mathcal{S}}\mathrm{div}_{\mathcal{S}}\,(\boldsymbol{v})\right)\,\mathrm{d}a\,, \tag{3.20}$$

where $\mathrm{div}_{\mathcal{S}}\,(\cdot)$ denotes the surface divergence on $\mathcal{S}$. For a detailed discussion on the surface divergence operator it is referred to Cermelli

et al. (2005), where the equivalence of

$$\mathrm{div}_{\mathcal{S}}\left(\boldsymbol{v}\right) = \mathrm{div}_{\mathcal{S}}\left(\boldsymbol{v}^{\parallel}\right) - k_{\mathcal{S}} v^{\perp} \tag{3.21}$$

is shown. Here, $\boldsymbol{v}^{\parallel}$ denotes the tangential component of the velocity $\boldsymbol{v}$ and $k_{\mathcal{S}} = -\mathrm{div}_{\mathcal{S}}\left(\boldsymbol{n}\right)$ denotes the total mean curvature of the singular surface. Additionally, the surface gradient operator

$$\mathrm{grad}_{\mathcal{S}}\left(\boldsymbol{v}\right) = \boldsymbol{P}_{\mathcal{S}}\mathrm{grad}\left(\boldsymbol{v}\right) , \qquad \boldsymbol{P}_{\mathcal{S}} \coloneqq \left(\boldsymbol{I} - \boldsymbol{n}_{\mathcal{S}} \otimes \boldsymbol{n}_{\mathcal{S}}\right) \tag{3.22}$$

according to Cermelli et al. (2005) is introduced for a material surface.

Equation of balance for volume and surface distributions

The additive quantity Ψ, which accounts for the bulk density $\Psi_{\mathcal{V}}$ and the surface density $\Psi_{\mathcal{S}}$, is introduced

$$\Psi = \int_{\mathcal{V}} \Psi_{\mathcal{V}} \,\mathrm{d}v + \int_{\mathcal{S}} \Psi_{\mathcal{S}} \,\mathrm{d}v \,. \tag{3.23}$$

The rate of change of Ψ may occur due to three different causes: Flux, production and supply. The flux per element of area penetrated through $\partial\mathcal{V}$ and the flux per element of line penetrated through $\partial\mathcal{S}$ are denoted by $\boldsymbol{\Phi}_{\mathcal{V}}$ and $\boldsymbol{\Phi}_{\mathcal{S}}$, respectively. Additionally, the production densities $p_{\mathcal{V}}$ and $p_{\mathcal{S}}$ as well as the supply densities $s_{\mathcal{V}}$ and $s_{\mathcal{S}}$, regarding the volume and the singular surface, are introduced. The general form of the equation of balance of a volume divided by a material singular surface reads

$$\begin{aligned} \frac{\mathrm{d}}{\mathrm{d}t}\int_{\mathcal{V}} \Psi_{\mathcal{V}} \,\mathrm{d}v + \frac{\mathrm{d}}{\mathrm{d}t}\int_{\mathcal{S}} \Psi_{\mathcal{S}} \,\mathrm{d}a = \int_{\partial\mathcal{V}} \boldsymbol{\Phi}_{\mathcal{V}} \cdot \boldsymbol{n} \,\mathrm{d}a + \int_{\partial\mathcal{S}} \boldsymbol{\Phi}_{\mathcal{S}} \cdot \boldsymbol{m} \,\mathrm{d}l \\ + \int_{\mathcal{V}} \left(p_{\mathcal{V}} + s_{\mathcal{V}}\right) \,\mathrm{d}v + \int_{\mathcal{S}} \left(p_{\mathcal{S}} + s_{\mathcal{S}}\right) \,\mathrm{d}a \,, \end{aligned} \tag{3.24}$$

cf. Müller (1985). With the divergence theorem according to Eq. (3.18) and transport theorem according to Eq. (3.19) the local equation of balance in regular points is obtained

$$\dot{\Psi}_{\mathcal{V}} + \Psi_{\mathcal{V}} \mathrm{div}\,(\boldsymbol{v}) = p_{\mathcal{V}} + s_{\mathcal{V}} + \mathrm{div}\,(\boldsymbol{\Phi}_{\mathcal{V}}) \; . \tag{3.25}$$

Additionally, with the transport theorem for material singular surfaces according to Eq. (3.20) the local equation of balance in singular points results in

$$\begin{aligned} \dot{\Psi}_{\mathcal{S}} + \Psi_{\mathcal{S}} \mathrm{div}_{\mathcal{S}}\,(\boldsymbol{v}) - \left[\!\left[\Psi_{\mathcal{V}}\,(\boldsymbol{v} - \boldsymbol{v}_{\mathcal{S}})\right]\!\right] \cdot \boldsymbol{n}_{\mathcal{S}} \\ = p_{\mathcal{S}} + s_{\mathcal{S}} + \mathrm{div}_{\mathcal{S}}\,(\boldsymbol{\Phi}_{\mathcal{S}}) + \left[\!\left[\boldsymbol{\Phi}_{\mathcal{V}}\right]\!\right] \cdot \boldsymbol{n}_{\mathcal{S}} \, . \end{aligned} \tag{3.26}$$

For a material singular surface it follows that the velocity field of the singular surface is equal to the spatial velocity field of the body, i.e., $\boldsymbol{v} = \boldsymbol{v}_{\mathcal{S}}$ and $\left[\!\left[\boldsymbol{v}\right]\!\right] = \boldsymbol{0}$.

3.3.2 Balance equations

Balance of mass

It is assumed that the mass densities are conservative quantities, i.e., mass productions do not occur. Furthermore, it is assumed that mass fluxes across the exterior surfaces or lines are zero, and that mass can not be created inside the material by external actions, i.e., mass supplies are zero. The overview of all quantities of the balance of mass is given in Table 3.1, where ϱ denotes the mass density of the bulk material and $\varrho_{\mathcal{S}}$ denotes the mass density of the singular surface. Consequently, the mass balance of a material body is given by

$$\frac{\mathrm{d}}{\mathrm{d}t} \int_{\mathcal{V}} \varrho \, \mathrm{d}v + \frac{\mathrm{d}}{\mathrm{d}t} \int_{\mathcal{S}} \varrho_{\mathcal{S}} \, \mathrm{d}a = 0 \, . \tag{3.27}$$

Table 3.1: Overview of all quantities contained in the balance of mass. Balanced quantity Ψ, production p, supply s and flux $\boldsymbol{\Phi}$ for bulk material and singular surface, respectively.

	Ψ	p	s	$\boldsymbol{\Phi}$
$\boldsymbol{x} \in \mathcal{V}$	ϱ	0	0	$\mathbf{0}$
$\boldsymbol{x} \in \mathcal{S}$	$\varrho_{\mathcal{S}}$	0	0	$\mathbf{0}$

With Eqs. (3.25) and (3.26) the local equations of balance of mass in regular points and singular points result to

$$\dot{\varrho} + \varrho \mathrm{div}\,(\boldsymbol{v}) = 0\,, \tag{3.28}$$

$$\dot{\varrho}_{\mathcal{S}} + \varrho_{\mathcal{S}} \mathrm{div}_{\mathcal{S}}\,(\boldsymbol{v}) = 0\,. \tag{3.29}$$

Müller (1985) explains Eq. (3.29) by an illustration of curved impermeable surfaces whose particles move perpendicular to the surface. In this study, however, the surface mass density $\varrho_{\mathcal{S}}$ is assumed to be a constant on the dividing surface. Consequently, Eq. (3.29) simplifies to

$$\mathrm{div}_{\mathcal{S}}\,(\boldsymbol{v}) = 0\,, \tag{3.30}$$

i.e., there is no local dilation of the surfaces, cf. Slattery (1990).

Balance of linear momentum

The balance of linear momentum is equivalent to Newton's second law of motion, which states that the rate of change of momentum of a body is equal to the forces acting on it. The applied forces are separated into body forces and contact forces. The body forces are denoted by $\boldsymbol{b}$ and $\boldsymbol{b}_{\mathcal{S}}$ for the body force per unit mass on the bulk material and surfaces, respectively. The contact forces are given with the Cauchy stress tensor $\boldsymbol{\sigma}$ and the surface stress tensor $\boldsymbol{\sigma}_{\mathcal{S}}$ by the bulk material stress vector $\boldsymbol{t} = \boldsymbol{\sigma}\boldsymbol{n}$ and the surface stress vector $\boldsymbol{t}_{\mathcal{S}} = \boldsymbol{\sigma}_{\mathcal{S}}\boldsymbol{m}$. The overview of all

Table 3.2: Overview of all quantities contained in the balance of linear momentum. Balanced quantity Ψ, production p, supply s and flux $\mathbf{\Phi}$ for bulk material and singular surface, respectively.

	Ψ	p	s	$\mathbf{\Phi}$
$\boldsymbol{x} \in \mathcal{V}$	$\varrho \boldsymbol{v}$	$\mathbf{0}$	$\varrho \boldsymbol{b}$	$\boldsymbol{\sigma}$
$\boldsymbol{x} \in \mathcal{S}$	$\varrho_{\mathcal{S}} \boldsymbol{v}$	$\mathbf{0}$	$\varrho_{\mathcal{S}} \boldsymbol{b}_{\mathcal{S}}$	$\boldsymbol{\sigma}_{\mathcal{S}}$

quantities of the balance of linear momentum is given in Table 3.2. Consequently, the balance of linear momentum is given by

$$\begin{aligned} &\frac{\mathrm{d}}{\mathrm{d}t} \int_{\mathcal{V}} \varrho \boldsymbol{v} \, \mathrm{d}v + \frac{\mathrm{d}}{\mathrm{d}t} \int_{\mathcal{S}} \varrho_{\mathcal{S}} \boldsymbol{v} \, \mathrm{d}a \\ = &\int_{\mathcal{V}} \varrho \boldsymbol{b} \, \mathrm{d}v + \int_{\mathcal{S}} \varrho_{\mathcal{S}} \boldsymbol{b}_{\mathcal{S}} \, \mathrm{d}a + \int_{\partial \mathcal{V}} \boldsymbol{t} \, \mathrm{d}a \int_{\partial \mathcal{S}} \boldsymbol{t}_{\mathcal{S}} \, \mathrm{d}l \, . \end{aligned} \tag{3.31}$$

By use of the balance of mass the local equations of balance of linear momentum in regular points and singular points result to

$$\varrho \dot{\boldsymbol{v}} = \varrho \boldsymbol{b} + \operatorname{div}(\boldsymbol{\sigma}) \, , \tag{3.32}$$

$$\varrho_{\mathcal{S}} \dot{\boldsymbol{v}} = \varrho_{\mathcal{S}} \boldsymbol{b}_{\mathcal{S}} + \operatorname{div}_{\mathcal{S}}(\boldsymbol{\sigma}_{\mathcal{S}}) + \left[\boldsymbol{\sigma}\right] \boldsymbol{n}_{\mathcal{S}} \, . \tag{3.33}$$

Balance of angular momentum

The balance of angular momentum states that when no external torques act on the material volume, no change of angular momentum will occur, i.e., the sum of all torques with respect to position $\boldsymbol{x}_0$ acting on a body must be zero. The overview of all quantities of the balance of angular momentum is given Table 3.3.

Table 3.3: Overview of all quantities contained in the balance of angular momentum. Balanced quantity Ψ, production p, supply s and flux $\boldsymbol{\Phi}$ for bulk material and singular surface, respectively.

	Ψ	p	s	$\boldsymbol{\Phi}$
$\boldsymbol{x} \in \mathcal{V}$	$(\boldsymbol{x}-\boldsymbol{x}_0)\times\varrho\boldsymbol{v}$	$\boldsymbol{0}$	$(\boldsymbol{x}-\boldsymbol{x}_0)\times\varrho\boldsymbol{b}$	$(\boldsymbol{x}-\boldsymbol{x}_0)\times\boldsymbol{\sigma}$
$\boldsymbol{x} \in \mathcal{S}$	$(\boldsymbol{x}-\boldsymbol{x}_0)\times\varrho_{\mathcal{S}}\boldsymbol{v}$	$\boldsymbol{0}$	$(\boldsymbol{x}-\boldsymbol{x}_0)\times\varrho_{\mathcal{S}}\boldsymbol{b}_{\mathcal{S}}$	$(\boldsymbol{x}-\boldsymbol{x}_0)\times\boldsymbol{\sigma}_{\mathcal{S}}$

The balance of angular momentum reads

$$\begin{aligned}\frac{\mathrm{d}}{\mathrm{d}t}\int_{\mathcal{V}}(\boldsymbol{x}-\boldsymbol{x}_0)\times\varrho\boldsymbol{v}\,\mathrm{d}v+\frac{\mathrm{d}}{\mathrm{d}t}\int_{\mathcal{S}}(\boldsymbol{x}-\boldsymbol{x}_0)\times\varrho_{\mathcal{S}}\boldsymbol{v}\,\mathrm{d}a\\ =\int_{\mathcal{V}}(\boldsymbol{x}-\boldsymbol{x}_0)\times\varrho\boldsymbol{b}\,\mathrm{d}v+\int_{\mathcal{S}}(\boldsymbol{x}-\boldsymbol{x}_0)\times\varrho_{\mathcal{S}}\boldsymbol{b}_{\mathcal{S}}\,\mathrm{d}a\\ +\int_{\partial\mathcal{V}}(\boldsymbol{x}-\boldsymbol{x}_0)\times\boldsymbol{t}\,\mathrm{d}a\int_{\partial\mathcal{S}}(\boldsymbol{x}-\boldsymbol{x}_0)\times\boldsymbol{t}_{\mathcal{S}}\,\mathrm{d}l\,.\end{aligned}\tag{3.34}$$

With the assumption that all work on the body is the result of forces, not torques, it is shown in Slattery (1990) that the balance of angular momentum results in

$$\boldsymbol{\sigma}=\boldsymbol{\sigma}^{\mathsf{T}}\,,\qquad \boldsymbol{\sigma}_{\mathcal{S}}=\boldsymbol{\sigma}_{\mathcal{S}}^{\mathsf{T}}\,.\tag{3.35}$$

Balance of kinetic energy

The balance of kinetic energy is a corollary of the balance of linear momentum. The scalar multiplication of Eqs. (3.32) and (3.33) with the local velocity $\boldsymbol{v}$ results in the local equations

$$\frac{1}{2}\varrho(\boldsymbol{v}\cdot\boldsymbol{v})^{\cdot}=\varrho\boldsymbol{b}\cdot\boldsymbol{v}-\boldsymbol{\sigma}\cdot\operatorname{grad}(\boldsymbol{v})+\operatorname{div}\left(\boldsymbol{\sigma}^{\mathsf{T}}\boldsymbol{v}\right)\,,\tag{3.36}$$

$$\frac{1}{2}\varrho_{\mathcal{S}}(\boldsymbol{v}\cdot\boldsymbol{v})^{\cdot}=\varrho_{\mathcal{S}}\boldsymbol{b}_{\mathcal{S}}\cdot\boldsymbol{v}-\boldsymbol{\sigma}_{\mathcal{S}}\cdot\operatorname{grad}_{\mathcal{S}}(\boldsymbol{v})+\operatorname{div}_{\mathcal{S}}\left(\boldsymbol{\sigma}_{\mathcal{S}}^{\mathsf{T}}\boldsymbol{v}\right)+\left[\!\left[\boldsymbol{\sigma}^{\mathsf{T}}\boldsymbol{v}\right]\!\right]\cdot\boldsymbol{n}_{\mathcal{S}}\,.\tag{3.37}$$

Table 3.4: Overview of all quantities contained in the balance of energy. Balanced quantity Ψ, production p, supply s and flux $\boldsymbol{\Phi}$ for bulk material and singular surface, respectively.

	Ψ	p	s	$\boldsymbol{\Phi}$
$\boldsymbol{x} \in \mathcal{V}$	$\varrho e + \varrho(\boldsymbol{v}\cdot\boldsymbol{v})/2$	0	$\varrho\omega + \varrho\boldsymbol{b}\cdot\boldsymbol{v}$	$-\boldsymbol{q} + \boldsymbol{\sigma}^{\mathsf{T}}\boldsymbol{v}$
$\boldsymbol{x} \in \mathcal{S}$	$\varrho_{\mathcal{S}} e_{\mathcal{S}} + \varrho_{\mathcal{S}}(\boldsymbol{v}\cdot\boldsymbol{v})/2$	0	$\varrho_{\mathcal{S}}\omega_{\mathcal{S}} + \varrho_{\mathcal{S}}\boldsymbol{b}_{\mathcal{S}}\cdot\boldsymbol{v}$	$-\boldsymbol{q}_{\mathcal{S}} + \boldsymbol{\sigma}_{\mathcal{S}}^{\mathsf{T}}\boldsymbol{v}$

From a comparison with the general forms of balance equations presented in Eqs. (3.25) and (3.26) it follows that the kinetic energy is not a conservative quantity, since the production densities $p_{\mathcal{V}} = -\boldsymbol{\sigma}\cdot\operatorname{grad}(\boldsymbol{v})$ and $p_{\mathcal{S}} = -\boldsymbol{\sigma}_{\mathcal{S}}\cdot\operatorname{grad}_{\mathcal{S}}(\boldsymbol{v})$ are present. With the symmetry of stresses according to Eq. (3.35) and the definition of the infinitesimal strain tensor according to Eq. (3.6) it follows $p_{\mathcal{V}} = -\boldsymbol{\sigma}\cdot\dot{\boldsymbol{\varepsilon}}$ and $p_{\mathcal{S}} = -\boldsymbol{\sigma}_{\mathcal{S}}\cdot(\boldsymbol{P}_{\mathcal{S}}\dot{\boldsymbol{\varepsilon}})$.

Balance of energy

The energy of a system is given as the sum of internal energy and kinetic energy. The internal energy is denoted by e and $e_{\mathcal{S}}$ for the bulk material and singular surfaces, respectively. Being a conservative quantity, there is no production of energy. The supply of energy is given by heat supply densities $\varrho\omega$ and $\varrho_{\mathcal{S}}\omega_{\mathcal{S}}$ and supply densities of kinetic energy $\varrho\boldsymbol{b}\cdot\boldsymbol{v}$ and $\varrho_{\mathcal{S}}\boldsymbol{b}_{\mathcal{S}}\cdot\boldsymbol{v}$. The flux of energy is composed of non-convective heat transfer by the heat flux vectors $-\boldsymbol{q}$ and $-\boldsymbol{q}_{\mathcal{S}}$ and the contact energy transmissions $\boldsymbol{\sigma}^{\mathsf{T}}\boldsymbol{v}$ and $\boldsymbol{\sigma}_{\mathcal{S}}^{\mathsf{T}}\boldsymbol{v}$ of the bulk material and the singular surfaces, respectively. The overview of all quantities of the balance of energy is given in Table 3.4. The balance of energy reads

$$\begin{aligned}\frac{\mathrm{d}}{\mathrm{d}t}\int_{\mathcal{V}}\varrho\left(e+\frac{1}{2}\boldsymbol{v}\cdot\boldsymbol{v}\right)\,\mathrm{d}v + \frac{\mathrm{d}}{\mathrm{d}t}\int_{\mathcal{S}}\varrho_{\mathcal{S}}\left(e_{\mathcal{S}}+\frac{1}{2}\boldsymbol{v}\cdot\boldsymbol{v}\right)\,\mathrm{d}a \\ = \int_{\mathcal{V}}\varrho\left(\omega+\boldsymbol{b}\cdot\boldsymbol{v}\right)\,\mathrm{d}v + \int_{\mathcal{S}}\varrho_{\mathcal{S}}\left(\omega_{\mathcal{S}}+\boldsymbol{b}_{\mathcal{S}}\cdot\boldsymbol{v}\right)\,\mathrm{d}a \\ + \int_{\partial\mathcal{V}}\left(\boldsymbol{v}\cdot\boldsymbol{t}-\boldsymbol{q}\cdot\boldsymbol{n}\right)\,\mathrm{d}a + \int_{\partial\mathcal{S}}\left(\boldsymbol{v}\cdot\boldsymbol{t}_{\mathcal{S}}-\boldsymbol{q}_{\mathcal{S}}\cdot\boldsymbol{m}\right)\,\mathrm{d}l\,.\end{aligned} \tag{3.38}$$

By use of the balance of mass the local equations of balance of energy in regular points and singular points result to

$$\varrho\left(\dot{e}+\frac{1}{2}\dot{\boldsymbol{v}}\cdot\boldsymbol{v}\right)=\varrho\left(\omega+\boldsymbol{b}\cdot\boldsymbol{v}\right)+\operatorname{div}\left(\boldsymbol{\sigma}^{\mathsf{T}}\boldsymbol{v}\right)-\operatorname{div}\left(\boldsymbol{q}\right)\,, \tag{3.39}$$

$$\begin{aligned}\varrho_{\mathcal{S}}\left(\dot{e}_{\mathcal{S}}+\frac{1}{2}\dot{\boldsymbol{v}}\cdot\boldsymbol{v}\right)&=\varrho_{\mathcal{S}}\left(\omega_{\mathcal{S}}+\boldsymbol{b}_{\mathcal{S}}\cdot\boldsymbol{v}\right)+\operatorname{div}_{\mathcal{S}}\left(\boldsymbol{\sigma}_{\mathcal{S}}^{\mathsf{T}}\boldsymbol{v}\right)-\operatorname{div}_{\mathcal{S}}\left(\boldsymbol{q}_{\mathcal{S}}\right)\\&\quad+\left[\!\left[\boldsymbol{\sigma}^{\mathsf{T}}\boldsymbol{v}\right]\!\right]\cdot\boldsymbol{n}_{\mathcal{S}}-\left[\!\left[\boldsymbol{q}\right]\!\right]\cdot\boldsymbol{n}_{\mathcal{S}}\,.\end{aligned} \tag{3.40}$$

Balance of internal energy

The local equations of balance of internal energy result by a subtraction of the local equations of balance of kinetic energy from the local equations of balance of energy. Subtracting Eqs. (3.36) and (3.37) from Eqs. (3.39) and (3.40) results in

$$\varrho\dot{e}=\varrho\omega+\boldsymbol{\sigma}\cdot\dot{\boldsymbol{\varepsilon}}-\operatorname{div}\left(\boldsymbol{q}\right)\,, \tag{3.41}$$

$$\varrho_{\mathcal{S}}\dot{e}_{\mathcal{S}}=\varrho_{\mathcal{S}}\omega_{\mathcal{S}}+\boldsymbol{\sigma}_{\mathcal{S}}\cdot\left(\boldsymbol{P}_{\mathcal{S}}\dot{\boldsymbol{\varepsilon}}\right)-\operatorname{div}_{\mathcal{S}}\left(\boldsymbol{q}_{\mathcal{S}}\right)-\left[\!\left[\boldsymbol{q}\right]\!\right]\cdot\boldsymbol{n}_{\mathcal{S}}\,. \tag{3.42}$$

Balance of entropy

The entropy is not a conservative quantity, therefore, the entropy production densities ϱp^{η} and $\varrho_{\mathcal{S}}p_{\mathcal{S}}^{\eta}$ are introduced for the bulk material and singular surfaces, respectively. For the entropy supply and the entropy flux the classical approach is chosen, cf., e.g., Coleman and Noll (1963), where the contribution to the balance of entropy results from the heat contribution divided by the absolute temperature θ. The absolute temperature is assumed to be continuous across singular surfaces, i.e., $\left[\!\left[\theta\right]\!\right]=0$. Consequently, the entropy density supplies and entropy flux vectors are given as listed in Table 3.5, where η and $\eta_{\mathcal{S}}$ denotes the mass specific entropy of the bulk material and singular surfaces, respectively.

Table 3.5: Overview of all quantities contained in the balance of entropy. Balanced quantity Ψ, production p, supply s and flux $\boldsymbol{\Phi}$ for bulk material and singular surface, respectively.

	Ψ	p	s	$\boldsymbol{\Phi}$
$\boldsymbol{x} \in \mathcal{V}$	$\varrho\eta$	ϱp^η	$\varrho\omega/\theta$	$-\boldsymbol{q}/\theta$
$\boldsymbol{x} \in \mathcal{S}$	$\varrho_\mathcal{S}\eta_\mathcal{S}$	$\varrho_\mathcal{S} p^\eta_\mathcal{S}$	$\varrho_\mathcal{S}\omega_\mathcal{S}/\theta$	$-\boldsymbol{q}_\mathcal{S}/\theta$

The balance of entropy reads

$$\begin{aligned} &\frac{\mathrm{d}}{\mathrm{d}t}\int_\mathcal{V} \varrho\eta \,\mathrm{d}v + \frac{\mathrm{d}}{\mathrm{d}t}\int_\mathcal{S} \varrho_\mathcal{S}\eta_\mathcal{S}\,\mathrm{d}a \\ &= \int_\mathcal{V} \varrho\left(\frac{\omega}{\theta} + p^\eta\right)\mathrm{d}v + \int_\mathcal{S} \varrho_\mathcal{S}\left(\frac{\omega_\mathcal{S}}{\theta} + p^\eta_\mathcal{S}\right)\mathrm{d}a \\ &\quad - \int_{\partial\mathcal{V}} \frac{\boldsymbol{q}}{\theta}\cdot\boldsymbol{n}\,\mathrm{d}a - \int_{\partial\mathcal{S}} \frac{\boldsymbol{q}_\mathcal{S}}{\theta}\cdot\boldsymbol{m}\,\mathrm{d}l\,. \end{aligned} \tag{3.43}$$

By use of the balance of mass the local equations of balance of entropy in regular points and singular points result to

$$\varrho\dot\eta = \varrho\frac{\omega}{\theta} + \varrho p^\eta - \operatorname{div}\left(\frac{\boldsymbol{q}}{\theta}\right), \tag{3.44}$$

$$\varrho_\mathcal{S}\dot\eta_\mathcal{S} = \varrho_\mathcal{S}\frac{\omega_\mathcal{S}}{\theta} + \varrho_\mathcal{S} p^\eta_\mathcal{S} - \operatorname{div}_\mathcal{S}\left(\frac{\boldsymbol{q}_\mathcal{S}}{\theta}\right) - \frac{1}{\theta}[\![\boldsymbol{q}]\!]\cdot\boldsymbol{n}_\mathcal{S}\,. \tag{3.45}$$

3.3.3 Clausius-Duhem inequality

The second law of thermodynamics states that, in a closed system, the minimum time rate change of entropy is equal to the rate of entropy transmission. Consequently, the total production of entropy is non-negative. In Coleman and Noll (1963) it is stated that it is necessary and sufficient that the specific entropy production is non-negative at all material points and at all times, i.e., $\varrho p^\eta \geq 0$ and $\varrho_\mathcal{S} p^\eta_\mathcal{S} \geq 0$. With $\mathcal{D} := \varrho p^\eta\theta$

the dissipation of bulk material is defined, whereas $\mathcal{D}_\mathcal{S} \coloneqq \varrho_\mathcal{S} p_\mathcal{S}^\eta \theta$ defines dissipation of singular surfaces. From a Legendre transformation it follows

$$\psi = e - \eta\theta\,, \tag{3.46}$$

$$\psi_\mathcal{S} = e_\mathcal{S} - \eta_\mathcal{S}\theta\,, \tag{3.47}$$

cf., e.g., Levine (2009), where the specific Helmholtz free energy of the bulk material ψ and the specific Helmholtz free energy of singular surfaces $\psi_\mathcal{S}$ are introduced. With Eqs. (3.41), (3.42), (3.44) and (3.45) the resulting inequalities, called Clausius-Duhem inequalities for regular points and singular points, read

$$\mathcal{D} = -\varrho\dot{\psi} - \varrho\eta\dot{\theta} + \boldsymbol{\sigma}\cdot\dot{\boldsymbol{\varepsilon}} - \frac{1}{\theta}\boldsymbol{q}\cdot\operatorname{grad}(\theta) \geq 0\,, \tag{3.48}$$

$$\mathcal{D}_\mathcal{S} = -\varrho_\mathcal{S}\dot{\psi}_\mathcal{S} - \varrho_\mathcal{S}\eta_\mathcal{S}\dot{\theta} + \boldsymbol{\sigma}_\mathcal{S}\cdot(\boldsymbol{P}_\mathcal{S}\dot{\boldsymbol{\varepsilon}}) - \frac{1}{\theta}\boldsymbol{q}_\mathcal{S}\cdot\operatorname{grad}_\mathcal{S}(\theta) \geq 0\,. \tag{3.49}$$

The mass density of the bulk material, the mass density of the singular surfaces, as well as the temperature, are per definition non-negative, i.e., $\varrho \geq 0, \varrho_\mathcal{S} \geq 0$ and $\theta \geq 0$.

3.4 Summary and conclusion

The deformation of a body is influenced by both external loads and and internal loads. Balance relations are introduced which provide statements about the connection between the rate of change of a mechanical or thermomechanical quantity based on production, supply and flux contributions. In continuum mechanics the mechanical balance relations of mass, linear momentum, angular momentum and kinetic energy are considered. With the balance of energy, internal energy and entropy the Clausius-Duhem inequalities are obtained by means of the second law of thermodynamics. Hereby, regular points and singular

surfaces are considered in order to model the mechanical behavior of the bulk material as well as the mechanical behavior of GBs in polycrystalline materials. This provides the basis to derive thermodynamically consistent flow rules for the plastic deformation inside the bulk material and at the GBs. In order to account for the nonlocal mechanical behavior of polycrystalline materials, which results from interactions between dislocations and GBs, however, additional DOF have to be introduced in the framework. In the following chapter a gradient crystal plasticity theory is established in the context of small deformations by considering the plastic slips as additional DOF.

Chapter 4

Gradient crystal plasticity theory

4.1 Introduction and motivation

For polycrystalline structures classical continuum theories fail to reproduce the experimentally observed influence of grain size on the yield stress, cf., e.g., Armstrong et al. (1962); Conrad et al. (1967). In order to account for work-hardening in polycrystals, Estrin et al. (1998) divides the cell structure into cell walls and cell interiors and formulates the resolved shear stress as a function of two dislocation densities, respectively. At the core of this and most phenomenological plasticity models are the evolution equations for the dislocation densities. A commonly used evolution law for FCC crystals accounts for dislocation storage and dislocation annihilation via the Kocks-Mecking relation, cf. Mecking and Lücke (1970); Kocks and Mecking (2003). While theories dependent on randomly distributed SSD are able to predict the overall mechanical behavior of homogeneous materials, plastically inhomogeneous deformations on the microscale require special consideration. To consider the work-hardening induced by interactions between dislocations and GBs, Ashby (1970) introduces the density of GND which is assumed to scale proportionally with the amount of plastic slip on each slip system. Based on this approach various strain gradient plasticity theories have been developed. In the early work of Aifantis (1987) the macroscopic back stress is formulated with regard to the Laplacian of

the plastic slip. More recent works include experimental investigations (e.g., by Fleck et al. (1994)), applications to polycrystals (e.g., by Ohno et al. (2008)), finite deformations (e.g., by Gurtin (2008)) and dissipative solids (e.g., by Miehe (2011)).

By introducing generalized stresses power conjugate to the in-plane gradients of plastic slip, Gurtin (2002) develops a thermodynamically consistent framework based on the principle of virtual power. Following the same approach, a thermomechanically coupled gradient theory is derived in Anand et al. (2015). While Gurtin (2002) uses an extension of the principle of virtual power to derive the governing equations for the gradient-enhanced plasticity model, Svendsen (2002) formulates the constitutive models by using an invariance consideration of the extended balance of total energy. In Prahs and Böhlke (2020b) the invariance of an extended energy balance is considered with respect to a change of observer. A contribution of kinetic energy associated with the scalar-valued slip is taken into account. This chapter gives an overview of the required assumptions in order to get a consistency of the model approaches by Gurtin (2002) and Prahs and Böhlke (2020b).

4.2 Model approach based on extended balance equations

4.2.1 Extended balance equations

Extended energy balance

For each slip system α the plastic slip γ_α is introduced as an additional DOF. Each additional scalar-valued DOF extends the balance of energy, given in Eq. (3.38), by an additional kinetic energy density, an additional volume specific mechanical power and an additional surface specific mechanical power. The spatial velocity of the additional DOF is

Table 4.1: Overview of all quantities contained in the extended balance of energy. Balanced quantity Ψ, production p, supply s and flux $\boldsymbol{\Phi}$ for bulk material and GBs, respectively.

	Ψ	p	s	$\boldsymbol{\Phi}$
$\boldsymbol{x} \in \mathcal{V}$	$\varrho e + \varrho(\boldsymbol{v}\cdot\boldsymbol{v})/2$ $+\sum_\alpha \varrho A_{\gamma\alpha}\dot{\gamma}_\alpha^2/2$	0	$\varrho\omega + \varrho\boldsymbol{b}\cdot\boldsymbol{v}$ $+\varrho\sum_\alpha b_{\gamma\alpha}\dot{\gamma}_\alpha$	$-\boldsymbol{q} + \boldsymbol{\sigma}^{\mathsf{T}}\boldsymbol{v}$ $+\sum_\alpha \boldsymbol{\xi}_\alpha\dot{\gamma}_\alpha$
$\boldsymbol{x} \in \mathcal{S}$	$\varrho_\mathcal{S} e_\mathcal{S} + \varrho_\mathcal{S}(\boldsymbol{v}\cdot\boldsymbol{v})/2$ $+\sum_\alpha \varrho_\mathcal{S} A_{\mathcal{S}\gamma\alpha}\dot{\gamma}_{\mathcal{S}\alpha}^2/2$	0	$\varrho_\mathcal{S}\omega_\mathcal{S} + \varrho_\mathcal{S}\boldsymbol{b}_\mathcal{S}\cdot\boldsymbol{v}$ $+\varrho_\mathcal{S}\sum_\alpha b_{\mathcal{S}\gamma\alpha}\dot{\gamma}_{\mathcal{S}\alpha}$	$-\boldsymbol{q}_\mathcal{S} + \boldsymbol{\sigma}_\mathcal{S}^{\mathsf{T}}\boldsymbol{v}$ $+\sum_\alpha \boldsymbol{\xi}_{\mathcal{S}\alpha}\dot{\gamma}_{\mathcal{S}\alpha}$

given as the time derivative of plastic slip, i.e., $\dot{\gamma}_\alpha$. For each slip system α the micro-inertia force $A_{\gamma\alpha}$, the generalized micro-body force $b_{\gamma\alpha}$ and the generalized micro-stress $\boldsymbol{\xi}_\alpha$ are introduced, cf. Prahs and Böhlke (2020b). Additional contributions regarding the GBs are denoted by $A_{\mathcal{S}\gamma\alpha}$, $b_{\mathcal{S}\gamma\alpha}$ and $\boldsymbol{\xi}_{\mathcal{S}\alpha}$, respectively. An overview of all contributions to the balance of energy extended by plastic slips is given in Table 4.1. With Eq. (3.24) the extended balance of energy is given by

$$
\begin{aligned}
&\frac{\mathrm{d}}{\mathrm{d}t}\int_\mathcal{V} \varrho\left(e + \frac{1}{2}\boldsymbol{v}\cdot\boldsymbol{v}\right)\,\mathrm{d}v + \frac{\mathrm{d}}{\mathrm{d}t}\int_\mathcal{S} \varrho_\mathcal{S}\left(e_\mathcal{S} + \frac{1}{2}\boldsymbol{v}\cdot\boldsymbol{v}\right)\,\mathrm{d}a \\
&+\frac{\mathrm{d}}{\mathrm{d}t}\int_\mathcal{V} \frac{1}{2}\sum_{\alpha=1}^{N} \varrho A_{\gamma\alpha}\dot{\gamma}_\alpha^2\,\mathrm{d}v + \frac{\mathrm{d}}{\mathrm{d}t}\int_\mathcal{S} \frac{1}{2}\sum_{\alpha=1}^{N} \varrho_\mathcal{S} A_{\mathcal{S}\gamma\alpha}\dot{\gamma}_{\mathcal{S}\alpha}^2\,\mathrm{d}a \\
&\qquad = \int_\mathcal{V} \varrho\,(\omega + \boldsymbol{b}\cdot\boldsymbol{v})\,\mathrm{d}v + \int_\mathcal{S} \varrho_\mathcal{S}\,(\omega_\mathcal{S} + \boldsymbol{b}_\mathcal{S}\cdot\boldsymbol{v})\,\mathrm{d}a \\
&\qquad\quad + \int_\mathcal{V} \varrho\sum_{\alpha=1}^{N} b_{\gamma\alpha}\dot{\gamma}_\alpha\,\mathrm{d}v + \int_\mathcal{S} \varrho_\mathcal{S}\sum_{\alpha=1}^{N} b_{\mathcal{S}\gamma\alpha}\dot{\gamma}_{\mathcal{S}\alpha}\,\mathrm{d}a \\
&\quad + \int_{\partial\mathcal{V}} (\boldsymbol{v}\cdot\boldsymbol{t} - \boldsymbol{q}\cdot\boldsymbol{n})\,\mathrm{d}a + \int_{\partial\mathcal{S}} (\boldsymbol{v}\cdot\boldsymbol{t}_\mathcal{S} - \boldsymbol{q}_\mathcal{S}\cdot\boldsymbol{m})\,\mathrm{d}l \\
&+ \int_{\partial\mathcal{V}} \sum_{\alpha=1}^{N} (\boldsymbol{\xi}_\alpha\cdot\boldsymbol{n})\,\dot{\gamma}_\alpha\,\mathrm{d}a + \int_{\partial\mathcal{S}} \sum_{\alpha=1}^{N} (\boldsymbol{\xi}_{\mathcal{S}\alpha}\cdot\boldsymbol{m})\,\dot{\gamma}_{\mathcal{S}\alpha}\,\mathrm{d}l\,.
\end{aligned}
\tag{4.1}
$$

In Prahs and Böhlke (2020b) the local form of the balance of mass and the local form of the balance of linear momentum are obtained for regular points under the assumption of invariance of the extended energy balance with respect to a change of observer. The extension to a material including singular surfaces is given in Prahs and Böhlke (2020a). From the invariance considerations it follows that neither the local balance of mass nor the local balance of linear momentum is affected by the extension of the balance of energy by additional scalar-valued DOF. By use of the balance of mass, given in Eq. (3.28), the local equation of the extended balance of energy in regular points results to

$$\begin{aligned}\varrho\left(\dot{e}+\frac{1}{2}\dot{\boldsymbol{v}}\cdot\boldsymbol{v}+\frac{1}{2}\sum_{\alpha=1}^{N}A_{\gamma\alpha}\ddot{\gamma}_\alpha\dot{\gamma}_\alpha+\frac{1}{2}\sum_{\alpha=1}^{N}\dot{A}_{\gamma\alpha}\dot{\gamma}_\alpha^2\right)\\ =\varrho\left(\omega+\boldsymbol{b}\cdot\boldsymbol{v}+\sum_{\alpha=1}^{N}b_{\gamma\alpha}\dot{\gamma}_\alpha\right)\\ +\operatorname{div}\left(\boldsymbol{\sigma}^{\mathsf{T}}\boldsymbol{v}\right)-\operatorname{div}\left(\boldsymbol{q}\right)+\sum_{\alpha=1}^{N}\operatorname{div}\left(\boldsymbol{\xi}_\alpha\dot{\gamma}_\alpha\right).\end{aligned}\tag{4.2}$$

Analogously, with Eq. (3.29), the local equation of the extended balance of energy in singular points follows

$$\begin{aligned}\varrho_{\mathcal{S}}\left(\dot{e}_{\mathcal{S}}+\frac{1}{2}\dot{\boldsymbol{v}}\cdot\boldsymbol{v}+\frac{1}{2}\sum_{\alpha=1}^{N}A_{\mathcal{S}\gamma\alpha}\ddot{\gamma}_{\mathcal{S}\alpha}\dot{\gamma}_{\mathcal{S}\alpha}+\frac{1}{2}\sum_{\alpha=1}^{N}\dot{A}_{\mathcal{S}\alpha}\dot{\gamma}_{\mathcal{S}\alpha}^2\right)\\ =\varrho_{\mathcal{S}}\left(\omega_{\mathcal{S}}+\boldsymbol{b}_{\mathcal{S}}\cdot\boldsymbol{v}+\sum_{\alpha=1}^{N}b_{\mathcal{S}\gamma\alpha}\dot{\gamma}_{\mathcal{S}\alpha}\right)\\ +\operatorname{div}_{\mathcal{S}}\left(\boldsymbol{\sigma}_{\mathcal{S}}^{\mathsf{T}}\boldsymbol{v}\right)-\operatorname{div}_{\mathcal{S}}\left(\boldsymbol{q}_{\mathcal{S}}\right)+\sum_{\alpha=1}^{N}\operatorname{div}_{\mathcal{S}}\left(\boldsymbol{\xi}_{\mathcal{S}\alpha}\dot{\gamma}_{\mathcal{S}\alpha}\right)\\ +\left[\boldsymbol{\sigma}^{\mathsf{T}}\boldsymbol{v}\right]\cdot\boldsymbol{n}_{\mathcal{S}}-\left[\boldsymbol{q}\right]\cdot\boldsymbol{n}_{\mathcal{S}}++\sum_{\alpha=1}^{N}\left[\boldsymbol{\xi}_\alpha\dot{\gamma}_\alpha\right]\cdot\boldsymbol{n}_{\mathcal{S}}.\end{aligned}\tag{4.3}$$

Extended internal energy balance

By subtracting the local form of the kinetic energy, given in Eq. (3.36), from the extended balance of energy, given in Eq. (4.2), the local form of the extended internal energy in regular points is obtained

$$\begin{aligned}\varrho\dot{e} = \varrho\left(\omega + \sum_{\alpha=1}^{N}\left(b_{\gamma\alpha} - \frac{1}{2}\left(A_{\gamma\alpha}\ddot{\gamma}_\alpha + \dot{A}_\alpha\dot{\gamma}_\alpha\right)\right)\dot{\gamma}_\alpha\right) \\ + \boldsymbol{\sigma}\cdot\dot{\boldsymbol{\varepsilon}} + \sum_{\alpha=1}^{N}\operatorname{div}\left(\boldsymbol{\xi}_\alpha\dot{\gamma}_\alpha\right) - \operatorname{div}\left(\boldsymbol{q}\right)\,.\end{aligned} \tag{4.4}$$

Analogously, the local form of the extended internal energy in singular points is obtained by subtracting Eq. (3.37) from Eq. (4.3)

$$\begin{aligned}\varrho_{\mathcal{S}}\dot{e}_{\mathcal{S}} = \varrho_{\mathcal{S}}\left(\omega_{\mathcal{S}} + \sum_{\alpha=1}^{N}\left(b_{\mathcal{S}\gamma\alpha} - \frac{1}{2}\left(A_{\mathcal{S}\gamma\alpha}\ddot{\gamma}_{\mathcal{S}\alpha} + \dot{A}_{\mathcal{S}\alpha}\dot{\gamma}_{\mathcal{S}\alpha}\right)\right)\dot{\gamma}_{\mathcal{S}\alpha}\right) \\ + \boldsymbol{\sigma}_{\mathcal{S}}\cdot\left(\boldsymbol{P}_{\mathcal{S}}\dot{\boldsymbol{\varepsilon}}\right) + \sum_{\alpha=1}^{N}\operatorname{div}_{\mathcal{S}}\left(\boldsymbol{\xi}_{\mathcal{S}\alpha}\dot{\gamma}_{\mathcal{S}\alpha}\right) - \operatorname{div}_{\mathcal{S}}\left(\boldsymbol{q}_{\mathcal{S}}\right) \\ + \sum_{\alpha=1}^{N}\left[\!\left[\boldsymbol{\xi}_\alpha\dot{\gamma}_\alpha\right]\!\right]\cdot\boldsymbol{n}_{\mathcal{S}} - \left[\!\left[\boldsymbol{q}\right]\!\right]\cdot\boldsymbol{n}_{\mathcal{S}}\,.\end{aligned} \tag{4.5}$$

Simplifying assumptions

Following the work of Prahs and Böhlke (2020a;b), effects associated with micro-body forces $b_{\gamma\alpha}$ and $b_{\mathcal{S}\gamma\alpha}$ and micro-inertia $A_{\gamma\alpha}$ and $A_{\mathcal{S}\gamma\alpha}$ are neglected. Consequently, it is assumed that there are no body forces or kinetic contributions associated with the plastic slips. Additionally, the surface stress vector of the GBs $\boldsymbol{t}_{\mathcal{S}}$, i.e., the contact force per unit length at the curve $\mathcal{S}$, as well as the additional contribution associated with the plastic slip $\boldsymbol{\xi}_{\mathcal{S}\alpha}\cdot\boldsymbol{m}$, are neglected as well. This simplification is motivated by the neglection of GB sliding within this work.

4.2.2 Clausius-Duhem inequality

Under consideration of these assumptions the Clausius-Duhem inequality for regular points and singular points result to

$$\mathcal{D} = -\varrho\dot{\psi} - \varrho\eta\dot{\theta} + \boldsymbol{\sigma}\cdot\dot{\boldsymbol{\varepsilon}} + \sum_{\alpha=1}^{N} \operatorname{div}\left(\boldsymbol{\xi}_\alpha\dot{\gamma}_\alpha\right) - \frac{1}{\theta}\boldsymbol{q}\cdot\operatorname{grad}\left(\theta\right) \geq 0\,, \quad (4.6)$$

$$\mathcal{D}_\mathcal{S} = -\varrho_\mathcal{S}\dot{\psi}_\mathcal{S} - \varrho_\mathcal{S}\eta_\mathcal{S}\dot{\theta} + \sum_{\alpha=1}^{N} \left[\boldsymbol{\xi}_\alpha\dot{\gamma}_\alpha\right]\cdot\boldsymbol{n}_\mathcal{S} - \frac{1}{\theta}\boldsymbol{q}_\mathcal{S}\cdot\operatorname{grad}_\mathcal{S}\left(\theta\right) \geq 0\,. \quad (4.7)$$

In order to derive the reduced dissipation inequalities constitutive assumptions are required for the free energy of the bulk material and the free energy of the GBs.

Bulk material

The Helmholtz free energy of the bulk material is assumed in the form

$$\psi = \psi(\boldsymbol{\varepsilon}_\mathrm{e}, \gamma_{\mathrm{ac}\alpha}, \operatorname{grad}\left(\gamma_\alpha\right), \theta)\,. \quad (4.8)$$

With this, the derivation of the Helmholtz free energy is given by

$$\begin{aligned}\dot{\psi} = \frac{\partial\psi}{\partial\boldsymbol{\varepsilon}}\cdot\dot{\boldsymbol{\varepsilon}} + \frac{\partial\psi}{\partial\boldsymbol{\varepsilon}_\mathrm{p}}\cdot\dot{\boldsymbol{\varepsilon}}_\mathrm{p} \\ + \sum_{\alpha=1}^{N}\left(\frac{\partial\psi}{\partial\gamma_{\mathrm{ac}\alpha}}\dot{\gamma}_{\mathrm{ac}\alpha} + \frac{\partial\psi}{\partial\operatorname{grad}\left(\gamma_\alpha\right)}\cdot\operatorname{grad}\left(\dot{\gamma}_\alpha\right)\right) + \frac{\partial\psi}{\partial\theta}\dot{\theta}\,.\end{aligned} \quad (4.9)$$

Hereby, slip fields are varied independently since they represent additional fields of DOF. The derivation with respect to the accumulated plastic strain can be further specified by

$$\frac{\partial\psi}{\partial\gamma_{\mathrm{ac}\alpha}}\dot{\gamma}_{\mathrm{ac}\alpha} = \frac{\partial\psi}{\partial\gamma_{\mathrm{ac}\alpha}}\left|\dot{\gamma}_\alpha\right| = \frac{\partial\psi}{\partial\gamma_{\mathrm{ac}\alpha}}\operatorname{sgn}\left(\dot{\gamma}_\alpha\right)\dot{\gamma}_\alpha\,. \quad (4.10)$$

Inserting Eq. (4.9) in the Clausius-Duhem inequality of the bulk material, given in Eq. (4.6), results in

$$\begin{aligned}\mathcal{D} = &\left(\boldsymbol{\sigma} - \frac{\partial \varrho\psi}{\partial \boldsymbol{\varepsilon}}\right) \cdot \dot{\boldsymbol{\varepsilon}} + \sum_{\alpha=1}^{N} \left(\boldsymbol{\xi}_\alpha - \frac{\partial \varrho\psi}{\partial \mathrm{grad}\,(\gamma_\alpha)}\right) \cdot \mathrm{grad}\,(\dot{\gamma}_\alpha) \\ &+ \sum_{\alpha=1}^{N} \left(\mathrm{div}\,(\boldsymbol{\xi}_\alpha) - \frac{\partial \varrho\psi}{\partial \gamma_{\mathrm{ac}\alpha}} \mathrm{sgn}\,(\dot{\gamma}_\alpha) - \frac{\partial \varrho\psi}{\partial \boldsymbol{\varepsilon}_\mathrm{p}} \cdot \boldsymbol{M}^\mathrm{s}_\alpha\right) \dot{\gamma}_\alpha \\ &- \left(\varrho\eta + \frac{\partial \varrho\psi}{\partial \theta}\right) \dot{\theta} - \frac{1}{\theta} \boldsymbol{q} \cdot \mathrm{grad}\,(\theta) \geq 0\,, \\ &\forall\, \boldsymbol{\varepsilon}, \dot{\boldsymbol{\varepsilon}}, \theta, \dot{\theta}, \gamma_\alpha, \dot{\gamma}_\alpha, \mathrm{grad}\,(\gamma_\alpha)\,, \mathrm{grad}\,(\dot{\gamma}_\alpha)\ ,\end{aligned} \tag{4.11}$$

where the evolution equations of the plastic strains, Eq. (3.9), is taken into account. Assuming that the Cauchy stress $\boldsymbol{\sigma}$ as well as the gradient stresses $\boldsymbol{\xi}_\alpha$ are purely energetic, the potential relations are obtained

$$\boldsymbol{\sigma} = \frac{\partial \varrho\psi}{\partial \boldsymbol{\varepsilon}}\,, \tag{4.12}$$

$$\boldsymbol{\xi}_\alpha = \frac{\partial \varrho\psi}{\partial \mathrm{grad}\,(\gamma_\alpha)}\,, \quad \forall \alpha \in \{1, \ldots, N\}\,, \tag{4.13}$$

$$\varrho\eta = -\frac{\partial \varrho\psi}{\partial \theta}\,. \tag{4.14}$$

This leads to the reduced dissipation equation of the bulk material

$$\underbrace{\sum_{\alpha=1}^{N} \left(\mathrm{div}\,(\boldsymbol{\xi}_\alpha) - \frac{\partial \varrho\psi}{\partial \gamma_{\mathrm{ac}\alpha}} \mathrm{sgn}\,(\dot{\gamma}_\alpha) - \frac{\partial \varrho\psi}{\partial \boldsymbol{\varepsilon}_\mathrm{p}} \cdot \boldsymbol{M}^\mathrm{s}_\alpha\right) \dot{\gamma}_\alpha}_{\text{mechanical contribution}} \underbrace{- \frac{1}{\theta} \boldsymbol{q} \cdot \mathrm{grad}\,(\theta)}_{\text{thermal contribution}} \geq 0\,, \tag{4.15}$$

which can be decomposed in a mechanical contribution and a thermal contribution. Here, both contributions of the dissipation are considered to be uncoupled. With Fourier's law for isotropy

$$\boldsymbol{q} = -\lambda_\Theta \mathrm{grad}\,(\theta)\ , \tag{4.16}$$

cf., e.g., Bergman et al. (2017), where λ_Θ denotes the thermal conductivity, the positivity of the thermal contribution to the dissipation is ensured. Consequently, the reduced dissipation equation of the bulk material is given as

$$\mathcal{D}_{\text{red}} = \sum_{\alpha=1}^{N} \left(\operatorname{div}(\boldsymbol{\xi}_\alpha) - \frac{\partial \varrho\psi}{\partial \gamma_{\text{ac}\alpha}} \operatorname{sgn}(\dot{\gamma}_\alpha) - \frac{\partial \varrho\psi}{\partial \boldsymbol{\varepsilon}_{\text{p}}} \cdot \boldsymbol{M}^{\text{s}}_\alpha \right) \dot{\gamma}_\alpha \geq 0 \,. \tag{4.17}$$

Grain boundaries

The Helmholtz free energy of the GBs is assumed to depend on the temperature as well as on the right-hand limit and the left-hand limit of the plastic slips, i.e.,

$$\psi_{\mathcal{S}} = \psi_{\mathcal{S}}(\gamma_\alpha^+, \gamma_\alpha^-, \theta) \,. \tag{4.18}$$

Slip fields are varied independently which results in

$$\dot{\psi}_{\mathcal{S}} = \sum_{\alpha=1}^{N} \left(\frac{\partial \psi_{\mathcal{S}}}{\partial \gamma_\alpha^+} \dot{\gamma}_\alpha^+ + \frac{\partial \psi_{\mathcal{S}}}{\partial \gamma_\alpha^-} \dot{\gamma}_\alpha^- \right) + \frac{\partial \psi_{\mathcal{S}}}{\partial \theta} \dot{\theta} \,. \tag{4.19}$$

With Eq. (4.7) this results in the dissipation of the GBs

$$\begin{aligned} \mathcal{D}_{\mathcal{S}} = \sum_{\alpha=1}^{N} \left(\boldsymbol{\xi}_\alpha^+ \cdot \boldsymbol{n}_{\mathcal{S}} - \frac{\partial \varrho_{\mathcal{S}} \psi_{\mathcal{S}}}{\partial \gamma_\alpha^+} \right) \dot{\gamma}_\alpha^+ + \sum_{\alpha=1}^{N} \left(-\boldsymbol{\xi}_\alpha^- \cdot \boldsymbol{n}_{\mathcal{S}} - \frac{\partial \varrho_{\mathcal{S}} \psi_{\mathcal{S}}}{\partial \gamma_\alpha^-} \right) \dot{\gamma}_\alpha^- \\ - \left(\varrho_{\mathcal{S}} \eta_{\mathcal{S}} + \frac{\partial \varrho_{\mathcal{S}} \psi_{\mathcal{S}}}{\partial \theta} \right) \dot{\theta} - \frac{1}{\theta} \boldsymbol{q}_{\mathcal{S}} \cdot \operatorname{grad}_{\mathcal{S}}(\theta) \geq 0 \,, \\ \forall\, \theta, \dot{\theta}, \gamma_\alpha^+, \dot{\gamma}_\alpha^+, \gamma_\alpha^-, \dot{\gamma}_\alpha^- \,. \end{aligned} \tag{4.20}$$

From this the potential relation

$$\varrho_{\mathcal{S}} \eta_{\mathcal{S}} = -\frac{\partial \varrho_{\mathcal{S}} \psi_{\mathcal{S}}}{\partial \theta} \tag{4.21}$$

is obtained. In analogy to Eq. (4.16) the Fourier's law for GBs

$$\boldsymbol{q}_{\mathcal{S}} = -\lambda_{\Theta\mathcal{S}} \mathrm{grad}_{\mathcal{S}}\left(\theta\right) , \tag{4.22}$$

with the thermal conductivity of GBs $\lambda_{\Theta\mathcal{S}}$, ensures the positivity of the thermal contribution of the dissipation. Consequently, the reduced dissipation equation of the GBs is given as

$$\begin{aligned} \mathcal{D}_{\mathcal{S}\mathrm{red}} = &\sum_{\alpha=1}^{N} \left(\boldsymbol{\xi}_{\alpha}^{+} \cdot \boldsymbol{n}_{\mathcal{S}} - \frac{\partial \varrho_{\mathcal{S}} \psi_{\mathcal{S}}}{\partial \gamma_{\alpha}^{+}} \right) \dot{\gamma}_{\alpha}^{+} \\ &+ \sum_{\alpha=1}^{N} \left(-\boldsymbol{\xi}_{\alpha}^{-} \cdot \boldsymbol{n}_{\mathcal{S}} - \frac{\partial \varrho_{\mathcal{S}} \psi_{\mathcal{S}}}{\partial \gamma_{\alpha}^{-}} \right) \dot{\gamma}_{\alpha}^{-} \geq 0 . \end{aligned} \tag{4.23}$$

4.3 Model approach based on principle of virtual power

4.3.1 Principle of virtual power

In the following, based on the principle of virtual power, so called microforce balance equations are obtained for each slip system. It is shown that the microforce balance equations are equivalent to nonlocal yield conditions for the individual slip systems.

For the evolution of the polycrystalline body, composed of bulk material and GBs, a microscopic and a macroscopic force system is considered. The microscopic system in Cermelli and Gurtin (2002) is defined by contributions of both, bulk material and GBs. The bulk material contributions are a lattice stress $\boldsymbol{\sigma}$ that expends power over the lattice strain-rate $\boldsymbol{\varepsilon}$ and, for each slip system α, a scalar-valued microstress π_{α} that expends power over the slip-rate $\dot{\gamma}_{\alpha}$ and a vector-valued microstress $\boldsymbol{\xi}_{\alpha}$ that expends power over the slip-rate gradient $\mathrm{grad}\left(\gamma_{\alpha}\right)$.

Regarding the GBs, microtractions Π_α^+ and Π_α^- expend power over the right-hand limit and left-hand limit of the slip rate γ_α^+ and γ_α^-, respectively. In Cermelli and Gurtin (2002) an additional GB contribution is given by a macroscopic internal force $\boldsymbol{\tau}$ conjugate to the rate of displacement discontinuity $\dot{[\![\boldsymbol{u}]\!]}$. Cavitation at the GB is excluded, i.e., $[\![\boldsymbol{u}]\!] \cdot \boldsymbol{n}_\mathcal{S} = \boldsymbol{0}$, however, the jump $[\![\boldsymbol{u}]\!]$, which is tangential to $\mathcal{S}$, introduces GB slip. This effect is neglected in this work. Based on the individual contributions the internal power is given as

$$\begin{aligned}\mathcal{P}_{\text{int}} = \int_\mathcal{V} \left(\boldsymbol{\sigma} \cdot \dot{\boldsymbol{\varepsilon}} + \sum_{\alpha=1}^{N} \left(\pi_\alpha \dot{\gamma}_\alpha + \boldsymbol{\xi}_\alpha \cdot \operatorname{grad}\left(\dot{\gamma}_\alpha\right) \right) \right) \mathrm{d}v \\ + \int_\mathcal{S} \sum_{\alpha=1}^{N} \left(\Pi_\alpha^+ \dot{\gamma}_\alpha^+ + \Pi_\alpha^- \dot{\gamma}_\alpha^- \right) \mathrm{d}a \,.\end{aligned} \tag{4.24}$$

The power of external forces is constructed based on the work of Gurtin (2002). The macroscopic system is defined by a body force density $\varrho \boldsymbol{b}$ and a macroscopic surface traction $\bar{\boldsymbol{t}}$, both associated with $\dot{\boldsymbol{u}}$, and further, for each slip system α, by a microscopic surface traction $\bar{\Xi}_\alpha$ associated with the plastic slip rate $\dot{\gamma}_\alpha$. Consequently, the power of external forces is given as

$$\mathcal{P}_{\text{ext}} = \int_\mathcal{V} \varrho \boldsymbol{b} \cdot \dot{\boldsymbol{u}} \, \mathrm{d}v + \int_{\partial \mathcal{V}_t} \bar{\boldsymbol{t}} \cdot \dot{\boldsymbol{u}} \, \mathrm{d}a + \int_{\partial \mathcal{V}_\Xi} \sum_{\alpha=1}^{N} \bar{\Xi}_\alpha \dot{\gamma}_\alpha \, \mathrm{d}a \,, \tag{4.25}$$

where $\partial \mathcal{V}_t$ denotes the Neumann boundary corresponding to $\boldsymbol{t}$ and $\partial \mathcal{V}_\Xi$ denotes the Neumann boundary corresponding to Ξ. The principle of virtual power states that given any generalized virtual velocity δv and any subregion the corresponding internal and external virtual powers are balanced. For Eqs. (4.24) and (4.25) the generalized virtual velocity is introduced as the list $\delta v = \{\delta \dot{\boldsymbol{u}}, \delta \dot{\boldsymbol{\varepsilon}}, \delta \dot{\gamma}_\alpha\}$, where $\delta \dot{\boldsymbol{u}}$, $\delta \dot{\boldsymbol{\varepsilon}}$ and $\delta \dot{\gamma}_\alpha$ denote

the virtual counterparts of $\dot{\boldsymbol{u}}$, $\dot{\boldsymbol{\varepsilon}}$ and $\dot{\gamma}_\alpha$. The power balance reads

$$\begin{aligned}\int_{\mathcal{V}} \left(\boldsymbol{\sigma} \cdot \delta\dot{\boldsymbol{\varepsilon}} + \sum_{\alpha=1}^{N} \left(\pi_\alpha \delta\dot{\gamma}_\alpha + \boldsymbol{\xi}_\alpha \cdot \operatorname{grad}\left(\delta\dot{\gamma}_\alpha\right) \right) \right) \mathrm{d}v \\ + \int_{\mathcal{S}} \sum_{\alpha=1}^{N} \left(\Pi_\alpha^+ \delta\dot{\gamma}_\alpha^+ + \Pi_\alpha^- \delta\dot{\gamma}_\alpha^- \right) \mathrm{d}a \\ - \int_{\mathcal{V}} \varrho \boldsymbol{b} \cdot \delta\dot{\boldsymbol{u}} \,\mathrm{d}v - \int_{\partial\mathcal{V}_t} \bar{\boldsymbol{t}} \cdot \delta\dot{\boldsymbol{u}} \,\mathrm{d}a - \int_{\partial\mathcal{V}_\Xi} \sum_{\alpha=1}^{N} \bar{\Xi}_\alpha \delta\dot{\gamma}_\alpha \,\mathrm{d}a = 0 \,.\end{aligned} \tag{4.26}$$

With the balance of angular momentum, i.e., $\boldsymbol{\sigma} = \boldsymbol{\sigma}^{\mathsf{T}}$, the application of the divergence theorem, given in Eq. (3.18), results in

$$\begin{aligned}\int_{\mathcal{V}} \sum_{\alpha=1}^{N} \left(\pi_\alpha - \operatorname{div}\left(\boldsymbol{\xi}_\alpha\right) \right) \delta\dot{\gamma}_\alpha \,\mathrm{d}v - \int_{\mathcal{V}} \left(\varrho \boldsymbol{b} + \operatorname{div}\left(\boldsymbol{\sigma}\right) \right) \cdot \delta\dot{\boldsymbol{u}} \,\mathrm{d}v \\ + \int_{\mathcal{S}} \sum_{\alpha=1}^{N} \left(\Pi_\alpha^+ \delta\dot{\gamma}_\alpha^+ + \Pi_\alpha^- \delta\dot{\gamma}_\alpha^- - \left[\boldsymbol{\xi}_\alpha \delta\dot{\gamma}_\alpha\right] \cdot \boldsymbol{n}_{\mathcal{S}} \right) \mathrm{d}a \\ + \int_{\partial\mathcal{V}_\Xi} \sum_{\alpha=1}^{N} \left(\boldsymbol{\xi}_\alpha \cdot \boldsymbol{n} - \bar{\Xi}_\alpha \right) \delta\dot{\gamma}_\alpha \,\mathrm{d}a + \int_{\partial\mathcal{V}_t} \left(\boldsymbol{\sigma}\boldsymbol{n} - \bar{\boldsymbol{t}} \right) \delta\dot{\boldsymbol{u}} \,\mathrm{d}a = 0 \,.\end{aligned} \tag{4.27}$$

Eq. (4.27) has to be satisfied for all $\{\delta\dot{\boldsymbol{u}}, \delta\dot{\gamma}\}$ and all subbodies, i.e., for bulk material as well as for GBs, separately. This results in the following local field equations, boundary conditions and GB conditions

$$\pi_\alpha - \operatorname{div}\left(\boldsymbol{\xi}_\alpha\right) = 0 \,, \qquad \forall \alpha \in \{1, \ldots, N\}, \quad \forall \boldsymbol{x} \in \mathcal{V} \,, \tag{4.28}$$

$$\varrho \boldsymbol{b} + \operatorname{div}\left(\boldsymbol{\sigma}\right) = \boldsymbol{0} \,, \qquad \forall \boldsymbol{x} \in \mathcal{V} \,, \tag{4.29}$$

$$\Xi_\alpha^+ - \boldsymbol{\xi}_\alpha^+ \cdot \boldsymbol{n}_{\mathcal{S}} = 0 \,, \qquad \forall \alpha \in \{1, \ldots, N\}, \quad \forall \boldsymbol{x} \in \mathcal{S} \,, \tag{4.30}$$

$$\Xi_\alpha^- + \boldsymbol{\xi}_\alpha^- \cdot \boldsymbol{n}_{\mathcal{S}} = 0 \,, \qquad \forall \alpha \in \{1, \ldots, N\}, \quad \forall \boldsymbol{x} \in \mathcal{S} \,, \tag{4.31}$$

$$\boldsymbol{\xi}_\alpha \cdot \boldsymbol{n} - \bar{\Xi}_\alpha = 0 \,, \qquad \forall \alpha \in \{1, \ldots, N\}, \quad \forall \boldsymbol{x} \in \partial\mathcal{V}_\Xi \,, \tag{4.32}$$

$$\boldsymbol{\sigma}\boldsymbol{n} - \bar{\boldsymbol{t}} = \boldsymbol{0} \,, \qquad \forall \boldsymbol{x} \in \partial\mathcal{V}_t \,. \tag{4.33}$$

With the pill-box theorem of Müller (1985) $\boldsymbol{n}_{\mathcal{S}} = \boldsymbol{n}_{\mathcal{V}}^{+} = -\boldsymbol{n}_{\mathcal{V}}^{-}$ holds true for the singular surface normal vectors of the right-hand subregion $\mathcal{V}^{+}$ and the left-hand subregion $\mathcal{V}^{-}$. Consequently, Eqs. (4.30) and (4.31) can be written as

$$\Xi_{\alpha}^{\pm} - \boldsymbol{\xi}_{\alpha}^{\pm} \cdot \boldsymbol{n}_{\mathcal{V}}^{\pm} = 0\,, \qquad \forall \alpha \in \{1, \ldots, N\}\,, \quad \forall \boldsymbol{x} \in \mathcal{S}\,. \tag{4.34}$$

4.3.2 Clausius-Duhem inequality

In the following, the Clausius-Duhem inequality is derived based on the work of Gurtin (2008), where a purely mechanical framework is considered. Subsequently, a comparison to the thermomechanical framework based on extended balance equations is made. The derivation of the dissipation inequality is based on a second law in which, for any subregion of the body, the temporal increase in free energy is less than or equal to the power expended on it. Thus, for the bulk material and the GBs it follows

$$\int_{\mathcal{V}} \varrho \dot{\psi} \, \mathrm{d}v \leq \mathcal{P}_{\text{ext}}(\mathcal{V})\,, \qquad \int_{\Gamma} \varrho_{\mathcal{S}} \dot{\psi}_{\mathcal{S}} \, \mathrm{d}a \leq \mathcal{P}_{\text{ext}}(\mathcal{S})\,, \tag{4.35}$$

where $\mathcal{P}_{\text{ext}}(\mathcal{V})$ denotes the power expended on the bulk material and $\mathcal{P}_{\text{ext}}(\mathcal{S})$ denotes the power expended on the GBs. With the power balance and Eq. (4.24) the dissipation of the bulk material $\mathcal{D}$ and the dissipation of the GBs $\mathcal{D}_{\mathcal{S}}$ are obtained by localization

$$\mathcal{D} = -\varrho \dot{\psi} + \boldsymbol{\sigma} \cdot \dot{\boldsymbol{\varepsilon}} + \sum_{\alpha=1}^{N} \left(\pi_{\alpha} \dot{\gamma}_{\alpha} + \boldsymbol{\xi}_{\alpha} \cdot \operatorname{grad}\left(\dot{\gamma}_{\alpha}\right) \right) \geq 0\,, \tag{4.36}$$

$$\mathcal{D}_{\mathcal{S}} = -\varrho_{\mathcal{S}} \dot{\psi}_{\mathcal{S}} + \sum_{\alpha=1}^{N} \left(\Pi_{\alpha}^{+} \dot{\gamma}_{\alpha}^{+} + \Pi_{\alpha}^{-} \dot{\gamma}_{\alpha}^{-} \right) \geq 0\,. \tag{4.37}$$

In order to derive the reduced dissipation inequalities constitutive assumptions are required for the free energy of the bulk material and the free energy of the GBs.

Bulk material

In the following, the Helmholtz free energy of the bulk material is assumed in the form

$$\psi = \psi(\boldsymbol{\varepsilon}_\mathrm{e}, \gamma_{\mathrm{ac}\alpha}, \mathrm{grad}\,(\gamma_\alpha))\,. \tag{4.38}$$

Inserting in the Clausius-Duhem inequality results in the bulk material dissipation inequality

$$\begin{aligned}\mathcal{D} = &\left(\boldsymbol{\sigma} - \frac{\partial \varrho\psi}{\partial \boldsymbol{\varepsilon}}\right) \cdot \dot{\boldsymbol{\varepsilon}} + \sum_{\alpha=1}^{N} \left(\boldsymbol{\xi}_\alpha - \frac{\partial \varrho\psi}{\partial \mathrm{grad}\,(\gamma_\alpha)}\right) \cdot \mathrm{grad}\,(\dot{\gamma}_\alpha) \\ &+ \sum_{\alpha=1}^{N} \left(\pi_\alpha - \frac{\partial \varrho\psi}{\partial \gamma_{\mathrm{ac}\alpha}} \mathrm{sgn}\,(\dot{\gamma}_\alpha) - \frac{\partial \varrho\psi}{\partial \boldsymbol{\varepsilon}_\mathrm{p}} \cdot \boldsymbol{M}^\mathrm{s}_\alpha\right) \dot{\gamma}_\alpha \geq 0\,, \\ &\qquad \forall\, \boldsymbol{\varepsilon}, \dot{\boldsymbol{\varepsilon}}, \gamma_\alpha, \dot{\gamma}_\alpha, \mathrm{grad}\,(\gamma_\alpha)\,, \mathrm{grad}\,(\dot{\gamma}_\alpha)\,.\end{aligned} \tag{4.39}$$

Assuming that the Cauchy stress $\boldsymbol{\sigma}$ as well as the gradient stresses $\boldsymbol{\xi}_\alpha$ are purely energetic, the following potential relations are obtained

$$\boldsymbol{\sigma} = \frac{\partial \varrho\psi}{\partial \boldsymbol{\varepsilon}}\,, \tag{4.40}$$

$$\boldsymbol{\xi}_\alpha = \frac{\partial \varrho\psi}{\partial \mathrm{grad}\,(\gamma_\alpha)}\,, \quad \forall \alpha \in \{1, \ldots, N\}\,. \tag{4.41}$$

This leads to the reduced dissipation equation of the bulk material

$$\mathcal{D}_\mathrm{red} = \sum_{\alpha=1}^{N} \left(\pi_\alpha - \frac{\partial \varrho\psi}{\partial \gamma_{\mathrm{ac}\alpha}} \mathrm{sgn}\,(\dot{\gamma}_\alpha) - \frac{\partial \varrho\psi}{\partial \boldsymbol{\varepsilon}_\mathrm{p}} \cdot \boldsymbol{M}^\mathrm{s}_\alpha\right) \dot{\gamma}_\alpha \geq 0\,. \tag{4.42}$$

Grain boundaries

The Helmholtz free energy of the GBs is assumed to depend on the right-hand limit and the left-hand limit of the plastic slips, i.e.,

$$\psi_{\mathcal{S}} = \psi_{\mathcal{S}}(\gamma_\alpha^+, \gamma_\alpha^-)\,. \tag{4.43}$$

Slip fields are varied independently which results in the dissipation of the GBs

$$\mathcal{D}_{\mathcal{S}\text{red}} = \sum_{\alpha=1}^{N} \left(\Xi_\alpha^+ - \frac{\partial \varrho_{\mathcal{S}} \psi_{\mathcal{S}}}{\partial \gamma_\alpha^+} \right) \dot{\gamma}_\alpha^+ + \sum_{\alpha=1}^{N} \left(\Xi_\alpha^- - \frac{\partial \varrho_{\mathcal{S}} \psi_{\mathcal{S}}}{\partial \gamma_\alpha^-} \right) \dot{\gamma}_\alpha^- \geq 0\,. \tag{4.44}$$

4.4 Comparison and simplifications

To compare the model approaches the following assumptions are made

- Helmholtz free energy temperature independent

$$\psi \neq \psi(\theta)\,, \qquad \psi_{\mathcal{S}} \neq \psi_{\mathcal{S}}(\theta) \tag{4.45}$$

- Isothermal processes

$$\dot{\theta} = 0 \tag{4.46}$$

- Homogeneous distribution of temperature

$$\operatorname{grad}(\theta) = \mathbf{0}\,, \qquad \operatorname{div}(\boldsymbol{q}) = \mathbf{0} \tag{4.47}$$

- No heat sources

$$\omega = 0\,, \qquad \omega_{\mathcal{S}} = 0 \tag{4.48}$$

With Eq. (4.45) and the potential relations of Eqs. (4.14) and (4.21), the Legendre transformations of Eqs. (3.46) and (3.47) result in $\psi = e$ and $\psi_{\mathcal{S}} = e_{\mathcal{S}}$ for the bulk material and GBs, respectively. Consequently,

with the made assumptions, the balance of internal energy, given in Eqs. (4.4) and (4.5), results in

$$\varrho\dot{e} = \boldsymbol{\sigma} \cdot \dot{\boldsymbol{\varepsilon}} + \sum_{\alpha=1}^{N} \operatorname{div}\left(\boldsymbol{\xi}_\alpha \dot{\gamma}_\alpha\right) , \tag{4.49}$$

$$\varrho_{\mathcal{S}}\dot{e}_{\mathcal{S}} = \sum_{\alpha=1}^{N} \left[\!\left[\boldsymbol{\xi}_\alpha \dot{\gamma}_\alpha\right]\!\right] \cdot \boldsymbol{n}_{\mathcal{S}} \, . \tag{4.50}$$

With Eqs. (4.6) and (4.7) it directly follows that both, the bulk material and GBs, are dissipation free, i.e.,

$$\mathcal{D} = -\varrho\dot{\psi} + \boldsymbol{\sigma} \cdot \dot{\boldsymbol{\varepsilon}} + \sum_{\alpha=1}^{N} \operatorname{div}\left(\boldsymbol{\xi}_\alpha \dot{\gamma}_\alpha\right) = 0 \, , \tag{4.51}$$

$$\mathcal{D}_{\mathcal{S}} = -\varrho_{\mathcal{S}}\dot{\psi}_{\mathcal{S}} + \sum_{\alpha=1}^{N} \left[\!\left[\boldsymbol{\xi}_\alpha \dot{\gamma}_\alpha\right]\!\right] \cdot \boldsymbol{n}_{\mathcal{S}} = 0 \, . \tag{4.52}$$

An in-depth discussion of the vanishing dissipation of a purely mechanical theory within the framework of continuum thermodynamics is given in Prahs and Böhlke (2022) for extended continua with additional non-thermal DOFs. Whereas in Prahs and Böhlke (2022) singular surfaces are not considered, it is shown by Eq. (4.52), that with the assumptions of Eqs. (4.45)–(4.48) the dissipation on the singular surfaces vanishes. The vanishing dissipation on singular points is also obtained in Prahs and Böhlke (2020a).

The comparison of the reduced dissipation inequalities obtained by extended balance equations, given in Eqs. (4.17) and (4.23), with the reduced dissipation inequalities obtained by the principle of virtual power, given in Eqs. (4.42) and (4.44), results in $\pi_\alpha = \operatorname{div}\left(\boldsymbol{\xi}_\alpha\right)$ and $\Xi_\alpha^{\pm} = \boldsymbol{\xi}_\alpha^{\pm} \cdot \boldsymbol{n}_{\mathcal{V}}^{\pm}$. These are the local field equations obtained from the principle of virtual power, i.e., Eqs. (4.28) and (4.13), which are contained implicitly in the model approach of extended balance equations.

4.5 Bulk material flow rule

In the following, a bulk material flow rule is constructed which fulfills the reduced dissipation inequality of the bulk material, given in Eq. (4.6). With the additive decomposition of strain into an elastic and plastic part, cf. Eq. (3.6), and the general linear elastic anisotropic Hooke's law, cf. Eq. (3.7), the potential relation

$$\frac{\partial \varrho\psi}{\partial \boldsymbol{\varepsilon}_{\mathrm{p}}} = -\boldsymbol{\sigma} \tag{4.53}$$

is obtained from Eq. (4.12). Furthermore, the following notation is introduced for the derivation of the free energy density by the accumulated plastic slip of slip system α

$$\beta_\alpha := \frac{\partial \varrho\psi}{\partial \gamma_{\mathrm{ac}\alpha}} \,. \tag{4.54}$$

With the result, that the bulk material is dissipation free, cf. Eq. (4.51), the reduced dissipation inequality of the bulk material, given in Eq. (4.6), results in

$$\left(\left(\tau_\alpha + \operatorname{div}\left(\boldsymbol{\xi}_\alpha\right)\right) \operatorname{sgn}\left(\dot{\gamma}_\alpha\right) - \beta_\alpha\right) \dot{\gamma}_{\mathrm{ac}\alpha} = 0 \,, \quad \forall \alpha \in \{1, \ldots, N\} \,. \tag{4.55}$$

Here, Eq. (3.10) is taken into account stating that $\dot{\gamma}_{\mathrm{ac}\alpha} = |\dot{\gamma}_\alpha|$. Assuming $\operatorname{sgn}\left(\dot{\gamma}_\alpha\right) = \operatorname{sgn}\left(\tau_\alpha + \operatorname{div}\left(\boldsymbol{\xi}_\alpha\right)\right)$ leads to

$$\left(\left|\tau_\alpha + \operatorname{div}\left(\boldsymbol{\xi}_\alpha\right)\right| - \beta_\alpha\right) \dot{\gamma}_{\mathrm{ac}\alpha} = 0 \,, \quad \forall \alpha \in \{1, \ldots, N\} \,. \tag{4.56}$$

To characterize plastic flow a yield criterion function $\varphi_\alpha \leq 0$ is defined for each slip system. For details on yield criterion functions it is referred to Simo and Hughes (1998). In this work, the rate-independent yield

criterion of slip system α is specified by

$$\varphi_\alpha := |\tau_\alpha + \operatorname{div}(\boldsymbol{\xi}_\alpha)| - \beta_\alpha \,. \tag{4.57}$$

Here, β_α characterizes the isotropic hardening of the yield surface and $\operatorname{div}(\boldsymbol{\xi}_\alpha)$ the kinematic hardening defining the center of the yield surface. Eq. (4.56) then reads

$$\varphi_\alpha \dot{\gamma}_{\mathrm{ac}\alpha} = 0 \,, \quad \forall \alpha \in \{1, \dots, N\} \,. \tag{4.58}$$

From this the loading and unloading conditions can be formulated for each slip system α in the Kuhn-Tucker form with

$$\varphi_\alpha \dot{\gamma}_{\mathrm{ac}\alpha} = 0 \,, \qquad \varphi_\alpha \leq 0 \,, \qquad \dot{\gamma}_{\mathrm{ac}\alpha} \geq 0 \,. \tag{4.59}$$

In contrast to viscoplasticity in the multi-slip case an active set search algorithm has to be used in the rate-independent case. The set of active slip systems is generally non-unique. For a comparison of algorithmic approaches it is referred to Miehe and Schröder (2001).

4.6 Summary and conclusion

In this work, the modeling of plastic slip under consideration of dislocation pile-up at GBs is realized by an extended energy balance according to Prahs and Böhlke (2020a;b). The framework is compared to the model approach based on an extended principle of virtual power according to Gurtin (2002). The two model approaches are equivalent if isothermal processes, a homogeneous distribution of temperature and a temperature-independent free energy for the bulk material and the GBs are assumed. It is shown, that under these assumptions the bulk material and the GBs are dissipation free. The following chapter is dedicated to the investigation of the GB flow rule.

Chapter 5

Comparison of grain boundary models

5.1 Introduction and motivation

In the early works of gradient plasticity theories, GBs act as insurmountable obstacles for plastic slip, cf., e.g., Gurtin (2002). Gurtin and Needleman (2005) discuss microhard and microfree boundary conditions within a gradient crystal plasticity framework. A microhard GB state corresponds to the situations when GBs act as barriers to dislocation motion, hence the plastic strain within the GBs vanishes. The microfree GB condition implies that the GBs allow free dislocation transmission so that the microtractions are prescribed to be zero, i.e., $\boldsymbol{\xi}_\alpha \cdot \boldsymbol{n}_\mathcal{S} = 0 \ \forall \alpha$. In order to model a GB behavior in between those limits, slip transmission criteria have to be introduced. The plastically active state of the GBs is referred to as microcontrolled in the following in order to highlight the controlled evolution of the GB slip by additional field equations.

A lot of experimental work has been done in order to detect GB resistance to slip transfer, e.g., by the use of nanoindentation. In Soer et al. (2005) a displacement jump is observed during the loading part of the indentation. It is shown in Wang and Ngan (2004) that this so called pop-in effect has a close relationship with the misorientation across the GB. The observed trend that the slip transmission ability of a GB is

mainly governed by the misorientation between slip planes and slip directions across the GB is supported by Wo and Ngan (2004). The direct observation of the interaction of individual dislocations with GBs of Kondo et al. (2016), however, shows that beside the geometric effects of misaligned slip systems, local structural stabilization effects cause the dislocation impediment at GBs.

It is stated in Wo and Ngan (2004) that nanoindentation are not an effective method to probe the slip transfer properties of GBs. Especially in FCC materials, where there is little dislocation locking and little resistance to slip transfer across GBs, a GB pop-in is not observed, cf. Britton et al. (2009). The efficient mechanical characterization of GBs using nanoindentation is therefore mainly restricted to BCC metals. For the characterization of GBs within BCC metals the mechanical response to nanoindentation is recorded as a function of the distance to the GB, cf., e.g., Soer and De Hosson (2005); Ohmura and Tsuzaki (2007). The characterization is strongly limited by the instrumented indentation and the recorded resolution. More recent work, e.g., Kalidindi and Vachhani (2014), therefore address these problems and obtain advances by automation of measurement and data analysis. Besides nanoindentation, in-situ electron microscope measurements and diffraction-contrast electron tomography can be used to investigate dislocation work hardening effects, cf., e.g., Lagow et al. (2001), or dislocation-GB interactions, cf., Kacher and Robertson (2014). Interactions of dislocations at GBs, however, are complex with multiple dislocation systems emitted simultaneously. Therefore, models and simulations of slip transmission across GBs are essential in order to understand the slip system activation within polycrystalline materials.

Various realizations of slip transmission criteria in simulations of metal materials exist. In Hamid et al. (2017) a GB model within a continuum dislocation dynamics framework is constructed. For each slip system pair a slip transmissivity number is computed based on the angle be-

tween the slip planes and the angle between the slip directions. This geometrical condition was introduced in Werner and Prantl (1990). The GB strength is assumed as a linear function of the slip transmissivity number. Alipour et al. (2020) construct a GB model based on the same geometrical condition of Werner and Prantl (1990) within a gradient-extended framework. Hereby, an overall measure of all slip system combinations is constructed. In contrast to Hamid et al. (2017) the assumed form of the GB yield strength is able to predict the limiting case of a microhard GB. Other simulation approaches for slip transmission phenomena are dislocation-density based crystalline plasticity formulations, cf., e.g., Shi and Zikry (2011), the modification of a classical crystal plasticity model where slip transfer is permitted only for low-angle boundaries, cf., Haouala et al. (2020), or atomistic simulations, cf. Spearot and Sangid (2014). The geometrical slip transmission criteria have in common that transmission prevails at low-angle GBs. It is shown in Liu et al. (2020) that in contrast to this, at high-angle GBs dislocation source activation occurs. This effect, however, is not considered in this work. For a detailed overview on slip transmission criteria in metals it is referred to the review article of Bayerschen et al. (2016).

In the following, the GB interface energy of Gurtin (2008), dependent on Nye's dislocation density tensor, is investigated. The surface energy incorporates both the orientation of the GBs relative to the crystal lattice of the adjacent grains and the misorientation of slip systems between adjacent grains. Intra-grain interactions and inter-grain interactions of dislocations on different slip systems provide a physically meaningful framework for polycrystalline structures. The numerical simulation of Özdemir and Yalçinkaya (2014) for the two dimensional case, or Gottschalk et al. (2016) and McBride et al. (2015) in three dimensions provide valuable insight into the GB model of Gurtin (2008). The plastic slip gradient at the GB is only dependent on the respective energy of the GB. The plastic slip rates at the GB are further assumed to be inde-

pendent. As shown in this work, for the limiting case of a vanishing grain misorientation, this only results in a single-crystal response for equally sized grains. In order to overcome this shortcoming, a second approach to derive the GB condition is introduced. Peng et al. (2019) couple the plastic slips for the incoming slip systems with the outgoing slip systems by kinematic relations. Hereby, however, a continuous distribution of plastic slip across GBs is assumed. In this work the general case of discontinuous plastic slip distributions is considered. An additional GB flow rule motivated by Wulfinghoff et al. (2013) and Erdle and Böhlke (2017) is introduced based on the gradient of plastic slip. Instead of the coupling of slip gradients of adjacent grains with a constant material parameter the coupling is formulated based on a misorientation function.

For the analytical investigation of the GB modeling approaches the framework is applied to the shearing of a three-phase periodic laminate structure for the special case of single slip. A similar problem, i.e., shearing of a two-phase structure consisting of an elasto-plastic phase and an elastic phase, has been investigated by Sedláček and Forest (2000) for a dislocation-based model of plasticity. Forest and Sedláček (2003) consider the identical boundary value problem in order to compare dislocation-based, Cosserat and strain-gradient models of crystal plasticity. In Forest (2008) the extension to a cyclic deformation is made in order to investigate kinematic hardening within the models. Additional applications to the two-phase laminate have been made in Cordero et al. (2010); Aslan et al. (2011) for the investigation of size-effects and in Forest and Guéninchault (2013); Wulfinghoff et al. (2015) for the investigation of free energy potentials in gradient crystal plasticity. Erdle and Böhlke (2017) consider a two-phase laminate consisting of two elasto-plastic phases in order to investigate GB effects within a gradient crystal plasticity framework. Prahs and Böhlke (2020a) reintroduce a purely elastic third phase for the investigation

of the influence of energy parameters with energetic GBs according to Gurtin (2008). Hereby, the special case of coherent slip systems, orthogonal to the GBs is considered. In this work the analytical solution of the three-phase laminate structure is constructed for a variable misorientation between the two adjacent elasto-plastic grains. The effect of the misorientation is investigated with special interest of a single crystal consistency check for coinciding slip systems.

5.2 Grain boundary flow rule

5.2.1 Grain boundary energy

In order to derive the GB conditions that fulfill Eq. (4.23) an expression of the specific free energy of the GB $\psi_{\mathcal{S}}$ is required. In this work a GB energy is chosen based on a measurement of GND. An experimental investigation of GND distribution in an aluminum bicrystal is performed in Sun et al. (1998; 2000). Here, it is shown that at first GND concentrate near the interface and redistribute with higher strain levels. This motivates a GB flow rule based on the amount of GND concentration at the GB and the activation of GB slip at higher strain levels. In order to characterize GND, Cermelli and Gurtin (2001) introduce the geometric dislocation tensor $\boldsymbol{G} = \boldsymbol{F}_{\mathrm{p}}\mathrm{curl}\left(\boldsymbol{F}_{\mathrm{p}}\right)/\det(\boldsymbol{F}_{\mathrm{p}})$. $\boldsymbol{G}$ measures the local Burgers vector, which represents the closure deficit of circuits deformed from a perfect lattice, per unit area in the microstructural configuration within a finite deformation setting. A gradient theory with a bulk material defect energy dependent on $\boldsymbol{G}$ is presented in Gurtin (2002). Here, $\boldsymbol{G} = \sum_{\alpha} \varrho_{\alpha}^{\odot} \boldsymbol{d}_{\alpha} \otimes \boldsymbol{d}_{\alpha} + \varrho_{\alpha}^{\perp}(\boldsymbol{n}_{\alpha} \times \boldsymbol{d}_{\alpha}) \otimes \boldsymbol{d}_{\alpha}$ is expressed in terms of pure screw dislocations $\varrho_{\alpha}^{\odot}$ and pure screw dislocations $\varrho_{\alpha}^{\perp}$. Additionally, for a small deformation theory, $\boldsymbol{G} = \mathrm{curl}\left(\boldsymbol{H}_{\mathrm{p}}\right)$ is given. A small deformation theory based on this is presented in Cermelli and Gurtin (2002) where the specific defect energy $\psi_{\mathrm{g}} = c \parallel \boldsymbol{G} \parallel^2 /2$ is chosen in a quadratic

isotropic form with material constant c. Based on this defect energy approach Gurtin and Needleman (2005) construct a possible GB condition. The Burgers vector density of the GB, measured per unit length, is characterized by the GB Burgers tensor $\boldsymbol{G}_{\mathcal{S}} = \llbracket \boldsymbol{H}_{\mathrm{p}} \rrbracket (\boldsymbol{n}_{\mathcal{S}} \times)$, which reads in index notation $(\boldsymbol{G}_{\mathcal{S}})_{il} = \llbracket (\boldsymbol{H}_{\mathrm{p}})_{ij} \rrbracket \epsilon_{jkl} (\boldsymbol{n}_{\mathcal{S}})_k$. Consequently, a GB is referred to as defect-free if $\llbracket \boldsymbol{H}_{\mathrm{p}} \rrbracket (\boldsymbol{n}_{\mathcal{S}} \times) = \boldsymbol{0}$ and the Burgers vector production within the GB is given as $\dot{G}_{\mathcal{S}} = \left\| \llbracket \dot{\boldsymbol{H}}_{\mathrm{p}} \rrbracket (\boldsymbol{n}_{\mathcal{S}} \times) \right\|$. Gurtin (2008) specifies the GB energy in a quadratic form

$$\varrho_{\mathcal{S}} \psi_{\mathcal{S}} = \frac{1}{2} \kappa \left\| \boldsymbol{G}_{\mathcal{S}} \right\|^2 , \tag{5.1}$$

based on the GB Burgers tensor. Here, the GB strength κ is introduced as a material parameter. With Eq. (3.8) the magnitude of the GB Burgers tensor can be formulated in terms of slip-interaction moduli of each slip system pair α, β as

$$\left\| \boldsymbol{G}_{\mathcal{S}} \right\|^2 = \sum_{\alpha=1}^{N} \sum_{\beta=1}^{N} C_{\alpha\beta}^{++} \gamma_{\alpha}^{+} \gamma_{\beta}^{+} + C_{\alpha\beta}^{--} \gamma_{\alpha}^{-} \gamma_{\beta}^{-} - 2 C_{\alpha\beta}^{+-} \gamma_{\alpha}^{+} \gamma_{\beta}^{-} , \tag{5.2}$$

cf. Gurtin (2008). The slip-interaction moduli

$$C_{\alpha\beta}^{++} = \left(\boldsymbol{d}_{\alpha}^{+} \cdot \boldsymbol{d}_{\beta}^{+} \right) \left(\boldsymbol{n}_{\alpha}^{+} \times \boldsymbol{n}_{\mathcal{S}} \right) \cdot \left(\boldsymbol{n}_{\beta}^{+} \times \boldsymbol{n}_{\mathcal{S}} \right) , \tag{5.3}$$

$$C_{\alpha\beta}^{--} = \left(\boldsymbol{d}_{\alpha}^{-} \cdot \boldsymbol{d}_{\beta}^{-} \right) \left(\boldsymbol{n}_{\alpha}^{-} \times \boldsymbol{n}_{\mathcal{S}} \right) \cdot \left(\boldsymbol{n}_{\beta}^{-} \times \boldsymbol{n}_{\mathcal{S}} \right) , \tag{5.4}$$

$$C_{\alpha\beta}^{+-} = \left(\boldsymbol{d}_{\alpha}^{+} \cdot \boldsymbol{d}_{\beta}^{-} \right) \left(\boldsymbol{n}_{\alpha}^{+} \times \boldsymbol{n}_{\mathcal{S}} \right) \cdot \left(\boldsymbol{n}_{\beta}^{-} \times \boldsymbol{n}_{\mathcal{S}} \right) \tag{5.5}$$

depend on the Schmid tensors $\boldsymbol{M}_{\alpha} = \boldsymbol{d}_{\alpha} \otimes \boldsymbol{n}_{\alpha}$ of the two grains and the GB normal vector $\boldsymbol{n}_{\mathcal{S}}$. $C_{\alpha\beta}^{++}$ and $C_{\alpha\beta}^{--}$ can be interpreted as intra-grain interaction moduli for the respective grain which represent interactions between slip systems within the respective grain. $C_{\alpha\beta}^{+-}$ is interpreted as an inter-grain interaction modulus which represents interactions between the two grains.

In the following dissipation free GBs are considered, cf. Eq. (4.52). With a discontinuous slip distribution across GBs the reduced dissipation inequality of the GBs, given in Eq. (4.23), results in N equations for the $2N$ GB slip values. Two approaches are presented in order to solve this underdetermined system of equations.

5.2.2 Approach I: Independent plastic slips

One approach, here called approach I, is to assume independent slip rates at the GB. With this assumption Eq. (4.52) can directly be solved to the $2N$ unknown GB slip values. With the assumption of independent slip rates at the GB it follows **Approach I (independent plastic slips)**

$$\boldsymbol{\xi}_\alpha^+ \cdot \boldsymbol{n}_\mathcal{S} = \varrho_\mathcal{S} \frac{\partial \psi_\mathcal{S}}{\partial \gamma_\alpha^+} = \sum_{\beta=1}^{N} \kappa \left(C_{\alpha\beta}^{++} \gamma_\beta^+ - C_{\alpha\beta}^{+-} \gamma_\beta^- \right) , \tag{5.6}$$

$$-\boldsymbol{\xi}_\alpha^- \cdot \boldsymbol{n}_\mathcal{S} = \varrho_\mathcal{S} \frac{\partial \psi_\mathcal{S}}{\partial \gamma_\alpha^-} = \sum_{\beta=1}^{N} \kappa \left(C_{\alpha\beta}^{--} \gamma_\beta^- - C_{\alpha\beta}^{+-} \gamma_\beta^+ \right) . \tag{5.7}$$

5.2.3 Approach II: Coupled plastic slips

In contrast to approach I, in the following the plastic slip rates at the GB are not considered to be independent. An additional flow condition based on a misorientation function $f(\boldsymbol{Q}_{\alpha\beta}^{+-}, \boldsymbol{n}_\mathcal{S})$ is introduced. $\boldsymbol{Q}_{\alpha\beta}^{+-}$ describes the misorientation between the slip systems α and β of the adjacent grains, e.g., by three Euler angles. In this work it is proposed that the misorientation function correlates to the amount of dislocations that piled-up at the GB, i.e., to the discontinuity of the plastic slip gradient at the GB. If two slip systems α and β hold no misorientation, $\boldsymbol{Q}_{\alpha\beta}^{+-} = \boldsymbol{I}$ holds true and no dislocations pile-up at the GB, which results in a continuous gradient of slip, i.e. $\left(\boldsymbol{\xi}_\beta^+ - \boldsymbol{\xi}_\alpha^- \right) \cdot \boldsymbol{n}_\mathcal{S} = 0$.

This results in **Approach II (coupled slips)**

$$\sum_{\alpha=1}^{N}\left(\boldsymbol{\xi}_{\alpha}^{+}\cdot\boldsymbol{n}_{\mathcal{S}}-\varrho_{\mathcal{S}}\frac{\partial\psi_{\mathcal{S}}}{\partial\gamma_{\alpha}^{+}}\right)\dot{\gamma}_{\alpha}^{+}-\sum_{\alpha=1}^{N}\left(\boldsymbol{\xi}_{\alpha}^{-}\cdot\boldsymbol{n}_{\mathcal{S}}+\varrho_{\mathcal{S}}\frac{\partial\psi_{\mathcal{S}}}{\partial\gamma_{\alpha}^{-}}\right)\dot{\gamma}_{\alpha}^{-}=0\,, \tag{5.8}$$

$$\left(\left(\boldsymbol{\xi}_{\beta}^{+}-\boldsymbol{\xi}_{\alpha}^{-}\right)\cdot\boldsymbol{n}_{\mathcal{S}}-\xi_{0}\left(1-f(\boldsymbol{Q}_{\alpha\beta}^{+-},\boldsymbol{n}_{\mathcal{S}})\right)\right)=0\,,\quad\forall\alpha,\beta\in\{1,\ldots,N\}\,, \tag{5.9}$$

with GB misorientation parameter ξ_0. Examples for the misorientation function can be found in Bayerschen et al. (2016). In this work, the misorientation function is adopted from the free energy of the GBs according to Gurtin (2008), given in Eq. (5.1), as

$$f(\boldsymbol{Q}_{\alpha\beta}^{+-},\boldsymbol{n}_{\mathcal{S}})=C_{\alpha\beta}^{+-}=\left(\boldsymbol{d}_{\alpha}^{-}\cdot\boldsymbol{d}_{\beta}^{+}\right)\left(\boldsymbol{n}_{\alpha}^{-}\times\boldsymbol{n}_{\mathcal{S}}\right)\cdot\left(\boldsymbol{n}_{\beta}^{+}\times\boldsymbol{n}_{\mathcal{S}}\right)\,. \tag{5.10}$$

5.3 Simulation setup: Shearing of a periodic laminate

The gradient crystal plasticity framework, introduced in Chapter 4, is applied to an elasto-plastic laminate microstructure in order to discuss the differences between the two GB flow rules. For sake of simplicity, the exact solution of the model problem is discussed under the assumption of single-slip and monotonic loading. For the cyclic deformation of a two-phase laminate structure and the in-depth discussion of the resulting generalized kinematic hardening modulus, cf. Forest (2008); Forest and Guéninchault (2013); Wulfinghoff et al. (2015). The laminate is exposed to plane strain, while, per definition, the plastic shear strain in the elastic phase is set to zero $\gamma=0$. As shown in the schematic illustration of Fig. 5.1 the laminate consists of three periodic layers, two elasto-plastic layers A and B colored in light gray and an elastic layer E

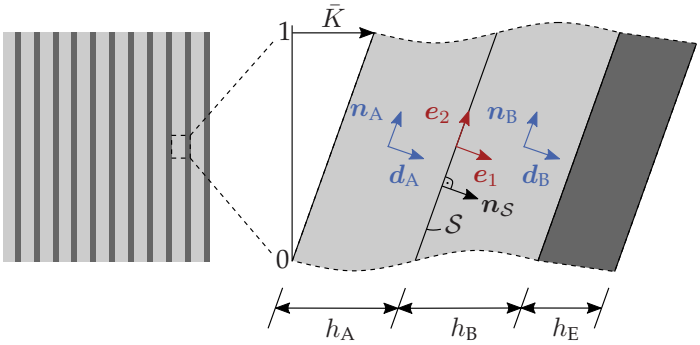

Figure 5.1: Undeformed periodic laminate material and deformed unit cell.

colored in dark gray. The GB between grain A and B is labeled $\mathcal{S}$ with the GB plane normal $\boldsymbol{n}_{\mathcal{S}}$. The origin of the coordinate system is located at the GB between the two adjacent elasto-plastic layers. The widths of the layers A, B and E are denoted by $h_{\mathrm{A}}, h_{\mathrm{B}}$ and h_{E}, respectively. Each grain contains a single slip system, with the orientations of the slip direction vectors denoted by $\boldsymbol{d}_{\mathrm{A}}$ and $\boldsymbol{d}_{\mathrm{B}}$ and the orientations of the slip plane normal vectors denoted by $\boldsymbol{n}_{\mathrm{A}}$ and $\boldsymbol{n}_{\mathrm{B}}$. The origin of the global coordinate system $\{\boldsymbol{e}_1, \boldsymbol{e}_2\}$ is located at the GB of the adjacent elasto-plastic grains A and B.

In order to account for a misorientation between the two grains, a local coordinate system $\{\tilde{\boldsymbol{e}}_1, \tilde{\boldsymbol{e}}_2\}$ is introduced in each grain, as illustrated in Figure 5.2. The orientation of the local coordinate systems is characterized by the rotation angles $\alpha_{\mathrm{A}}, \alpha_{\mathrm{B}}$ for each grain, respectively. Quantities given in the local coordinate system are denoted by a tilde, e.g., $\tilde{\boldsymbol{x}}$. The angle between the local coordinate system and slip system is denoted by Φ. In this work, the single slip system is not rotated towards the local coordinate system so that $\Phi = 0$. Consequently, the slip system corresponds with the local system yielding $\boldsymbol{d}_{\mathrm{A}} = \boldsymbol{d}_{\mathrm{B}} = \tilde{\boldsymbol{e}}_1$ and $\boldsymbol{n}_{\mathrm{A}} = \boldsymbol{n}_{\mathrm{B}} = \tilde{\boldsymbol{e}}_2$. For the transformation from the global coordinate system $\{\boldsymbol{e}_1, \boldsymbol{e}_2, \boldsymbol{e}_3\}$ into the local coordinate system $\{\tilde{\boldsymbol{e}}_1, \tilde{\boldsymbol{e}}_2, \tilde{\boldsymbol{e}}_3\}$ a trans-

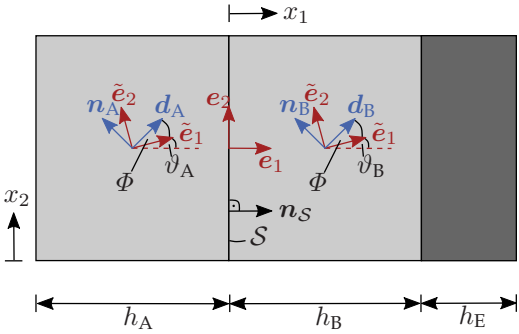

Figure 5.2: Notation for the orientation of the single slip systems.

formation matrix $\boldsymbol{Q}_\vartheta$ is defined by $\tilde{\boldsymbol{x}} = \boldsymbol{Q}_\vartheta \boldsymbol{x}$. The transformation is performed by a rotation about the $\boldsymbol{e}_3$-axis by the angles ϑ_A and ϑ_B for grains A and B, respectively. Consequently, the transformation reads

$$\begin{pmatrix} \tilde{x}_1 \\ \tilde{x}_2 \\ \tilde{x}_3 \end{pmatrix} = \begin{pmatrix} \cos(\vartheta) & -\sin(\vartheta) & 0 \\ \sin(\vartheta) & \cos(\vartheta) & 0 \\ 0 & 0 & 1 \end{pmatrix} \begin{pmatrix} x_1 \\ x_2 \\ x_3 \end{pmatrix}, \qquad \forall \vartheta = \{\vartheta_\mathrm{A}, \vartheta_\mathrm{B}\}. \tag{5.11}$$

5.4 Analytical solution

5.4.1 Constitutive assumptions

The free energy in the bulk material within the small deformation framework is assumed to be additively decomposed into three terms

$$\psi(\boldsymbol{\varepsilon}_\mathrm{e}, \gamma_\mathrm{ac}, \mathrm{grad}(\gamma)) = \psi_\mathrm{e}(\boldsymbol{\varepsilon}_\mathrm{e}) + \psi_\mathrm{g}(\mathrm{grad}(\gamma)) + \psi_\mathrm{h}(\gamma_\mathrm{ac}), \tag{5.12}$$

where γ_{ac} denotes the accumulated plastic slip. For the exact solution a monotonous evolution of the plastic slip is assumed, i.e., $\gamma_{\mathrm{ac}} = \gamma$. The free energy density for the bulk thereby consists of an elastic energy contribution ψ_{e}, a defect energy contribution ψ_{g} and an isotropic hardening energy contribution ψ_{h}, which are introduced in the following. The elastic energy contribution is given by

$$\varrho\psi_{\mathrm{e}} = \frac{1}{2}\boldsymbol{\varepsilon}_{\mathrm{e}} \cdot \mathbb{C}[\boldsymbol{\varepsilon}_{\mathrm{e}}] = \frac{1}{2}(\boldsymbol{\varepsilon} - \boldsymbol{\varepsilon}_{\mathrm{p}}) \cdot \mathbb{C}[\boldsymbol{\varepsilon} - \boldsymbol{\varepsilon}_{\mathrm{p}}]\,. \tag{5.13}$$

For sake of simplicity elastic isotropic material behavior is considered. Consequently, elastic material properties are independent of direction in space. In this case the stiffness matrix consists of only two independent entries

$$\mathbb{C} = \lambda \boldsymbol{I} \otimes \boldsymbol{I} + 2\mu \mathbb{I}^{\mathrm{S}}\,, \tag{5.14}$$

where λ and μ are so called Lamé parameters. With this, the Hooke's law for linear elastic isotropic solid bodies reads

$$\boldsymbol{\sigma} = \lambda \mathrm{tr}(\boldsymbol{\varepsilon}_{\mathrm{e}})\boldsymbol{I} + 2\mu\boldsymbol{\varepsilon}_{\mathrm{e}}\,. \tag{5.15}$$

For the defect energy density the phenomenological, quadratic approach

$$\varrho\psi_{\mathrm{g}} = \frac{1}{2}K_{\mathrm{g}} \| \mathrm{grad}\,(\gamma)\,\|^2 \tag{5.16}$$

is chosen, where K_{g} is a constant defect parameter. Isotropic hardening is characterized by the isotropic hardening energy

$$\varrho\psi_{\mathrm{h}} = \frac{1}{2}K_0\gamma^2 + \tau_0\gamma\,, \tag{5.17}$$

where K_0 and τ_0 are introduced as material parameters. Supplementary to the free energy in the bulk material, an additional energy density per unit area contribution on the GB is introduced. For the special case of

single slip Eq. (5.1) results in

$$\varrho_{\mathcal{S}}\psi_{\mathcal{S}} = \frac{1}{2}\kappa\left(C_{\mathrm{AA}}\gamma_{\mathcal{S}\mathrm{A}}^2 + C_{\mathrm{BB}}\gamma_{\mathcal{S}\mathrm{B}}^2 - 2C_{\mathrm{AB}}\gamma_{\mathcal{S}\mathrm{A}}\gamma_{\mathcal{S}\mathrm{B}}\right) , \tag{5.18}$$

with right-hand limit of plastic slip $\gamma^+ = \gamma_{\mathcal{S}\mathrm{B}}$, left-hand limit of plastic slip $\gamma^- = \gamma_{\mathcal{S}\mathrm{A}}$ and GB strength κ. The slip-interaction moduli are given with Eq. (5.5) as

$$C_{\mathrm{AA}} = (\boldsymbol{n}_{\mathrm{A}} \times \boldsymbol{n}_{\mathcal{S}}) \cdot (\boldsymbol{n}_{\mathrm{A}} \times \boldsymbol{n}_{\mathcal{S}}) , \tag{5.19}$$

$$C_{\mathrm{BB}} = (\boldsymbol{n}_{\mathrm{B}} \times \boldsymbol{n}_{\mathcal{S}}) \cdot (\boldsymbol{n}_{\mathrm{B}} \times \boldsymbol{n}_{\mathcal{S}}) , \tag{5.20}$$

$$C_{\mathrm{AB}} = (\boldsymbol{d}_{\mathrm{A}} \cdot \boldsymbol{d}_{\mathrm{B}})\,(\boldsymbol{n}_{\mathrm{A}} \times \boldsymbol{n}_{\mathcal{S}}) \cdot (\boldsymbol{n}_{\mathrm{B}} \times \boldsymbol{n}_{\mathcal{S}}) . \tag{5.21}$$

5.4.2 Displacement field, strain and stress

The displacement field for simple shear deformation is given as

$$\boldsymbol{u} = u_1(x_1, x_2)\boldsymbol{e}_1 + u_2(x_1, x_2)\boldsymbol{e}_2 \tag{5.22}$$

in the global coordinate system. It is defined for each grain in the following boundaries

$$\boldsymbol{u} = \begin{cases} \boldsymbol{u}_{\mathrm{A}}(x_1, x_2) , & x_1 \in [-h_{\mathrm{A}}, 0] \\ \boldsymbol{u}_{\mathrm{B}}(x_1, x_2) , & x_1 \in [0, h_{\mathrm{B}}] \\ \boldsymbol{u}_{\mathrm{E}}(x_1, x_2) , & x_1 \in [h_{\mathrm{B}}, h_{\mathrm{B}} + h_{\mathrm{E}}] \end{cases} . \tag{5.23}$$

The displacement field in the local coordinate system reads

$$\tilde{\boldsymbol{u}} = \begin{cases} \tilde{\boldsymbol{u}}_{\mathrm{A}}(\tilde{x}_1, \tilde{x}_2) , & \tilde{x}_1 \in [-h_{\mathrm{A}}/\cos(\vartheta_{\mathrm{A}}), 0] \\ \tilde{\boldsymbol{u}}_{\mathrm{B}}(\tilde{x}_1, \tilde{x}_2) , & \tilde{x}_1 \in [0, h_{\mathrm{B}}/\cos(\vartheta_{\mathrm{B}})] \\ \tilde{\boldsymbol{u}}_{\mathrm{E}}(\tilde{x}_1, \tilde{x}_2) , & \tilde{x}_1 \in [h_{\mathrm{B}}/\cos(\vartheta_{\mathrm{B}}), (h_{\mathrm{B}}/\cos(\vartheta_{\mathrm{B}})) + h_{\mathrm{E}}] \end{cases} . \tag{5.24}$$

Considering the local coordinate system, it is further assumed that the displacement in $\tilde{\boldsymbol{e}}_1$-direction only depends on $\tilde{x}_2$ and the displacement in $\tilde{\boldsymbol{e}}_2$-direction only on $\tilde{x}_1$ yielding

$$\tilde{\boldsymbol{u}} = \tilde{u}_1(\tilde{x}_2)\tilde{\boldsymbol{e}}_1 + \tilde{u}_2(\tilde{x}_1)\tilde{\boldsymbol{e}}_2 \,. \tag{5.25}$$

An elastic isotropic and homogeneous material is assumed. The infinitesimal strain tensor in the local coordinate system is defined by

$$\tilde{\boldsymbol{\varepsilon}} = \operatorname{sym}(\operatorname{grad}(\tilde{\boldsymbol{u}})) = \frac{1}{2}\left(\frac{\mathrm{d}\tilde{u}_1}{\mathrm{d}\tilde{x}_2} + \frac{\mathrm{d}\tilde{u}_2}{\mathrm{d}\tilde{x}_1}\right)(\tilde{\boldsymbol{e}}_1 \otimes \tilde{\boldsymbol{e}}_2 + \tilde{\boldsymbol{e}}_2 \otimes \tilde{\boldsymbol{e}}_1) \,. \tag{5.26}$$

Further, with the assumption of a monotonous evolution of the plastic slip, the plastic strain tensor in the local coordinate system is defined with Eq. (3.9) by

$$\tilde{\boldsymbol{\varepsilon}}_{\mathrm{p}} = \tilde{\gamma}\tilde{\boldsymbol{M}}^{\mathrm{s}} = \frac{1}{2}\tilde{\gamma}\,(\tilde{\boldsymbol{e}}_1 \otimes \tilde{\boldsymbol{e}}_2 + \tilde{\boldsymbol{e}}_2 \otimes \tilde{\boldsymbol{e}}_1) \,. \tag{5.27}$$

The local Cauchy stress tensor is given by Hooke's law

$$\tilde{\boldsymbol{\sigma}} = \tilde{\mathbb{C}}[\tilde{\boldsymbol{\varepsilon}} - \tilde{\boldsymbol{\varepsilon}}_{\mathrm{p}}] = G\left(\frac{\mathrm{d}\tilde{u}_1}{\mathrm{d}\tilde{x}_2} + \frac{\mathrm{d}\tilde{u}_2}{\mathrm{d}\tilde{x}_1} - \tilde{\gamma}\right)(\tilde{\boldsymbol{e}}_1 \otimes \tilde{\boldsymbol{e}}_2 + \tilde{\boldsymbol{e}}_2 \otimes \tilde{\boldsymbol{e}}_1) \,. \tag{5.28}$$

The resolved shear stress in the local coordinate system results in

$$\tilde{\tau} = \tilde{\boldsymbol{\sigma}} \cdot \tilde{\boldsymbol{M}}^{\mathrm{s}} = \mu\left(\frac{\mathrm{d}\tilde{u}_1}{\mathrm{d}\tilde{x}_2} + \frac{\mathrm{d}\tilde{u}_2}{\mathrm{d}\tilde{x}_1} - \tilde{\gamma}\right) \,. \tag{5.29}$$

5.4.3 Analytical solution for plastic slip

From Eqs. (4.13) and (4.54) it follows

$$\beta := \frac{\partial \varrho\psi}{\partial \gamma} = K_0\gamma + \tau_0\,, \tag{5.30}$$

$$\boldsymbol{\xi} = \frac{\partial \varrho\psi}{\partial \mathrm{grad}\,(\gamma)} = K_\mathrm{g}\,\mathrm{grad}\,(\gamma)\ . \tag{5.31}$$

Consequently, the bulk material flow rule, given in Eq. (4.57), results in

$$K_\mathrm{g}\mathrm{div}\,(\mathrm{grad}\,(\gamma)) - K_0\gamma + (\tau - \tau_0) = 0\,. \tag{5.32}$$

With Eq. (5.29) the inhomogeneous second-order linear ordinary differential equation in the local coordinate system is given by

$$K_\mathrm{g}\frac{\mathrm{d}^2\tilde{\gamma}}{\mathrm{d}\tilde{x}_1^2} - K_0\tilde{\gamma} = -\mu\left(\frac{\mathrm{d}\tilde{u}_1}{\mathrm{d}\tilde{x}_2} + \frac{\mathrm{d}\tilde{u}_2}{\mathrm{d}\tilde{x}_1} - \tilde{\gamma}\right) + \tau_0\,. \tag{5.33}$$

The balance of linear momentum, given in Eq. (3.32), results in

$$0 = \mu\frac{\mathrm{d}^2\tilde{u}_1}{\mathrm{d}\tilde{x}_2^2}\,, \qquad 0 = \mu\left(\frac{\mathrm{d}^2\tilde{u}_2}{\mathrm{d}\tilde{x}_1^2} - \frac{\mathrm{d}\tilde{\gamma}}{\mathrm{d}\tilde{x}_1}\right)\,. \tag{5.34}$$

From this integration results in the displacement fields

$$\tilde{u}_{1\mathrm{A}} = k_{\mathrm{uA}}\tilde{x}_2 + d_{\mathrm{uA}}\,, \tag{5.35}$$

$$\tilde{u}_{1\mathrm{B}} = k_{\mathrm{uB}}\tilde{x}_2 + d_{\mathrm{uB}}\,, \tag{5.36}$$

$$u_\mathrm{E} = k_{\mathrm{uE}}x_2 + d_{\mathrm{uE}}\,, \tag{5.37}$$

$$\tilde{u}_{2\mathrm{A}} = \int \tilde{\gamma}_\mathrm{A}\,\mathrm{d}\tilde{x}_1 + k_{\mathrm{vA}}\tilde{x}_1 + d_{\mathrm{vA}}\,, \tag{5.38}$$

$$\tilde{u}_{2\mathrm{B}} = \int \tilde{\gamma}_\mathrm{B}\,\mathrm{d}\tilde{x}_1 + k_{\mathrm{vB}}\tilde{x}_1 + d_{\mathrm{vB}}\,, \tag{5.39}$$

$$u_\mathrm{E} = k_{\mathrm{vE}}x_1 + d_{\mathrm{vE}}\,, \tag{5.40}$$

where $k_{\mathrm{uA}}, k_{\mathrm{uB}}, k_{\mathrm{uE}}, d_{\mathrm{uA}}, d_{\mathrm{uB}}, d_{\mathrm{uE}}$ and $k_{\mathrm{vA}}, k_{\mathrm{vB}}, k_{\mathrm{vE}}, d_{\mathrm{vA}}, d_{\mathrm{vB}}, d_{\mathrm{vE}}$ are 12 unknown integration constants. With these relations the plastic slip distribution within grain A

$$\begin{aligned}\tilde{\gamma}_{\mathrm{A}}(\tilde{x}_1) = c_{1\mathrm{A}} \exp\left(\sqrt{\frac{K_0}{K_{\mathrm{g}}}}\tilde{x}_1\right) + c_{2\mathrm{A}} \exp\left(-\sqrt{\frac{K_0}{K_{\mathrm{g}}}}\tilde{x}_1\right) \\ + \frac{G\left(k_{\mathrm{uA}} + k_{\mathrm{vA}}\right) - \tau_0}{K_0}\,,\end{aligned} \tag{5.41}$$

and the plastic slip distribution within grain B

$$\begin{aligned}\tilde{\gamma}_{\mathrm{B}}(\tilde{x}_1) = c_{1\mathrm{B}} \exp\left(\sqrt{\frac{K_0}{K_{\mathrm{g}}}}\tilde{x}_1\right) + c_{2\mathrm{B}} \exp\left(-\sqrt{\frac{K_0}{K_{\mathrm{g}}}}\tilde{x}_1\right) \\ + \frac{G\left(k_{\mathrm{uB}} + k_{\mathrm{vB}}\right) - \tau_0}{K_0}\,,\end{aligned} \tag{5.42}$$

result from Eq. (5.33), with constants $c_{1\mathrm{A}}, c_{2\mathrm{A}}, c_{1\mathrm{B}}, c_{2\mathrm{B}}$. In the following the boundary conditions are introduced to determine the 16 constants.

5.4.4 Boundary conditions

Boundary conditions for plastic slip

The laminate consists of three periodic layers. Grain B, and due to periodicity also grain A, adjoin the elastic grain. At the respective GB between an elasto-plastic grain and the elastic grain the plastic slip must be equal zero. Therefore, the two boundary conditions read

$$\tilde{\gamma}_{\mathrm{A}}\left(\tilde{x}_1 = -\frac{h_{\mathrm{A}}}{\cos\left(\vartheta_{\mathrm{A}}\right)}\right) = 0\,, \tag{5.43}$$

$$\tilde{\gamma}_{\mathrm{B}}\left(\tilde{x}_1 = \frac{h_{\mathrm{B}}}{\cos\left(\vartheta_{\mathrm{B}}\right)}\right) = 0\,. \tag{5.44}$$

At the GB between the two elasto-plastic layers, the plastic slip is discontinuous with a right-hand limit $\gamma_{\mathcal{S}\mathrm{B}}$ and a left-hand limit $\gamma_{\mathcal{S}\mathrm{A}}$, i.e.,

$$\tilde{\gamma}_{\mathrm{A}}\left(\tilde{x}_1 = 0\right) = \gamma_{\mathcal{S}\mathrm{A}}\,, \tag{5.45}$$

$$\tilde{\gamma}_{\mathrm{B}}\left(\tilde{x}_1 = 0\right) = \gamma_{\mathcal{S}\mathrm{B}}\,. \tag{5.46}$$

The four equations are sufficient to determine the four constants $c_{1\mathrm{A}}$, $c_{2\mathrm{A}}$, $c_{1\mathrm{B}}$ and $c_{2\mathrm{B}}$.

Boundary conditions for the displacement field

The laminate is exposed to a simple shear deformation. For this case four loading conditions can be determined. At $x_2 = 0$ no displacement occurs, i.e.,

$$u_{1\mathrm{A}}(x_1, x_2 = 0) = 0\,, \tag{5.47}$$

$$u_{1\mathrm{B}}(x_1, x_2 = 0) = 0\,, \tag{5.48}$$

$$u_{1\mathrm{E}}(x_1, x_2 = 0) = 0\,. \tag{5.49}$$

At $x_2 = 1$ the constant macroscopic shear strain $\bar{K}$ is applied, i.e.,

$$u_{1\mathrm{A}}(x_1, x_2 = 1) = \bar{K}\,, \tag{5.50}$$

$$u_{1\mathrm{B}}(x_1, x_2 = 1) = \bar{K}\,, \tag{5.51}$$

$$u_{1\mathrm{E}}(x_1, x_2 = 1) = \bar{K}\,. \tag{5.52}$$

Additionally to the loading conditions the continuity of the displacement field at the GBs

$$u_{2\mathrm{A}}(x_1 = 0, x_2) = u_{2\mathrm{B}}(x_1 = 0, x_2)\,, \tag{5.53}$$

$$u_{2\mathrm{B}}(x_1 = h_{\mathrm{B}}, x_2) = u_{2\mathrm{E}}(x_1 = h_{\mathrm{B}}, x_2) \tag{5.54}$$

is taken into account. Eq. (3.33) states that the stress vector is continuous at GBs. This requires

$$\left[\left(\boldsymbol{Q}_\vartheta^\mathsf{T}\tilde{\boldsymbol{\sigma}}\boldsymbol{Q}_\vartheta\right)\boldsymbol{n}_\mathcal{S}\right] = \boldsymbol{0}\,, \tag{5.55}$$

with $\boldsymbol{n}_\mathcal{S} = \boldsymbol{e}_1$. Thus, one additional boundary condition is obtained for both the GB between the two elasto-plastic grains A and B and for the GB between the elasto-plastic grain B and the elastic grain E.

Finally, u_2 is assumed to be a periodic fluctuation field. The periodicity requires

$$\int_{-h_\mathrm{A}}^{0} \frac{\partial u_{2\mathrm{A}}}{\partial x_1}\,\mathrm{d}x_1 + \int_{0}^{h_\mathrm{B}} \frac{\partial u_{2\mathrm{B}}}{\partial x_1}\,\mathrm{d}x_1 + \int_{h_\mathrm{B}}^{h_\mathrm{B}+h_\mathrm{E}} \frac{\partial u_{2\mathrm{E}}}{\partial x_1}\,\mathrm{d}x_1 = 0\,, \tag{5.56}$$

if u_2 is continuous at the GB. The definition of u_2 as fluctuation requires

$$\int_{-h_\mathrm{A}}^{0} u_{2\mathrm{A}}\,\mathrm{d}x_1 + \int_{0}^{h_\mathrm{B}} u_{2\mathrm{B}}\,\mathrm{d}x_1 + \int_{h_\mathrm{B}}^{h_\mathrm{B}+h_\mathrm{E}} u_{2\mathrm{E}}\,\mathrm{d}x_1 = 0\,. \tag{5.57}$$

With Eqs. (5.47)–(5.57) 12 boundary conditions are obtained that are sufficient to solve for the 12 integration constants of the displacement fields $\boldsymbol{u}_\mathrm{A}$, $\boldsymbol{u}_\mathrm{B}$ and $\boldsymbol{u}_\mathrm{E}$.

5.5 Comparison of grain boundary flow condition approaches

5.5.1 Material parameters

The material parameters of the aluminium-type bulk material are chosen according to Bayerschen et al. (2015). Isotropic elastic material behavior is homogeneous within the laminate material with $\mu = 27\mathrm{GPa}$. The plastic behavior in both elasto-plastic layers is also chosen to be

homogeneous with $\tau_0 = 10\mathrm{MPa}$, $K_0 = 1075\mathrm{MPa}$ and $K_\mathrm{g} = 84\mu\mathrm{N}$. The GB strength is chosen according to Özdemir and Yalçinkaya (2014) as $\kappa = 2100\mathrm{N/m}$. The remaining material parameter of GB flow condition approach II is chosen as $\xi_0 = 100\mathrm{N/m}$.

5.5.2 Limit case of vanishing misorientation

In order to discuss the differences between the two GB flow condition approaches for the limit case of vanishing misorientation, this section focuses on the influence of the grain width of the elasto-plastic grains on the solution. In the following investigation, the width of the left elasto-plastic grain is chosen to be $h_\mathrm{A} = 0.5\mu\mathrm{m}$, while the width of the right elasto-plastic grain h_B is varied between $h_\mathrm{B} = h_\mathrm{A}$ and $h_\mathrm{B} = h_\mathrm{A}/8$. The width of the elastic layer is set to $h_\mathrm{E} = 0.5\mu\mathrm{m}$, however, with γ being zero, the elastic layer is only shown in the figures showing the displacement field. The misorientation between the adjacent elasto-plastic grains A and B is assumed to vanish. Therefore, the grain structure is a single-crystal problem and the GB between the elasto-plastic grains A and B should not be observable.

For a macroscopic shear of $\bar{K} = 0.01$, Fig. 5.3a shows the exact solution of the plastic slip $\tilde{\gamma}(\tilde{x}_1)$ in shear direction over the laminate for the GB flow condition approach I. In case of identical grain widths $h_\mathrm{A} = h_\mathrm{B}$, the distribution of the plastic slip is continuous across the GB. As soon as the grain widths of the elasto-plastic grains are not equal, i.e., $h_\mathrm{B} < h_\mathrm{A}$, the plastic slip is discontinuous with $\gamma_{\mathcal{S}\mathrm{A}} > \gamma_{\mathcal{S}\mathrm{B}}$. It can be seen that with decreasing grain width h_B, the discontinuity of the plastic slip at the GB increases. The single crystal consistency check is satisfied only for $h_\mathrm{A} = h_\mathrm{B}$, where a continuous distribution of the plastic slip is observed. For the limit case of a vanishing misorientation, the discontinuous distribution of the plastic slip for the case of $h_\mathrm{B} < h_\mathrm{A}$ is unexpected.

According to GB flow condition approach I, given in Eq. (5.7), the gradient of the slip depends only on the GB energy $\psi_\mathcal{S}$. For the limit case

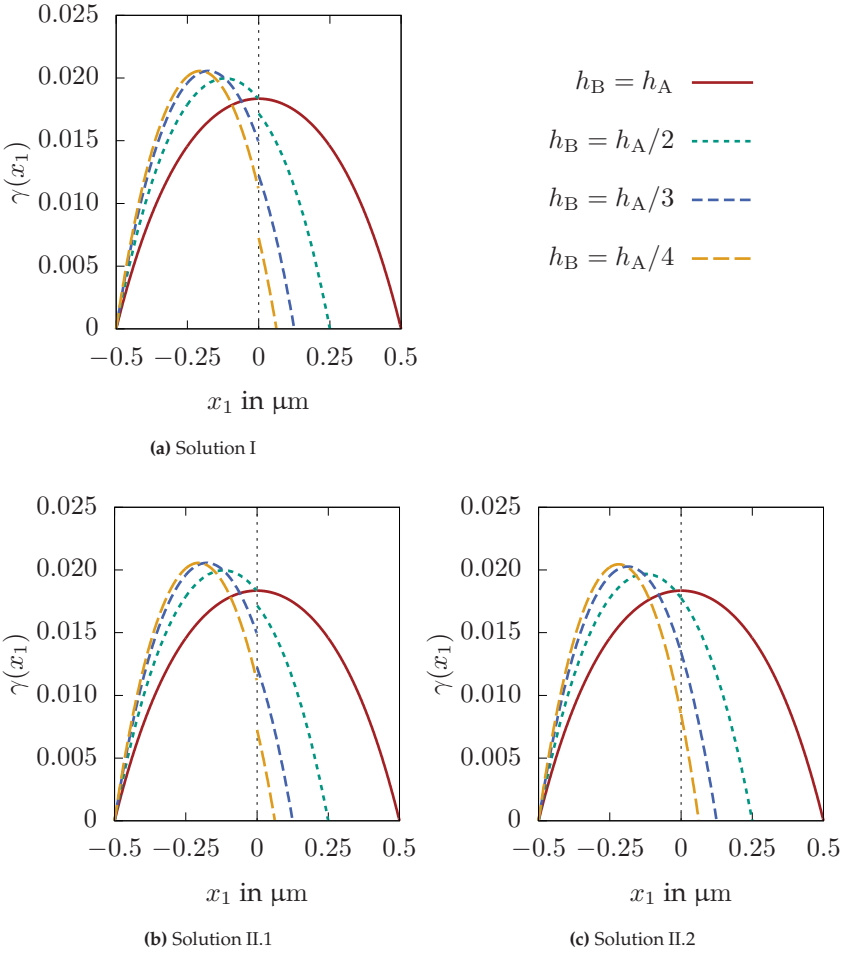

(a) Solution I

(b) Solution II.1

(c) Solution II.2

Figure 5.3: Comparison of GB flow condition approach I (top) and approach II (bottom) for the limit case of vanishing misorientation with a macroscopic shear of $\bar{K} = 0.01$. The exact solutions for the plastic slip $\tilde{\gamma}(\tilde{x}_1)$ are shown for a varying grain width h_B.

of vanishing misorientation the GB flow condition reads

$$\boldsymbol{\xi}_{\mathrm{B}} \cdot \boldsymbol{n}_{\mathcal{S}} + \kappa \left(\gamma_{\mathcal{S}\mathrm{A}} - \gamma_{\mathcal{S}\mathrm{B}} \right) = 0 \,, \tag{5.58}$$

$$\boldsymbol{\xi}_{\mathrm{A}} \cdot \boldsymbol{n}_{\mathcal{S}} + \kappa \left(\gamma_{\mathcal{S}\mathrm{A}} - \gamma_{\mathcal{S}\mathrm{B}} \right) = 0 \,. \tag{5.59}$$

A solution is obtained for $\boldsymbol{\xi}_{\mathrm{A}} \cdot \boldsymbol{n}_{\mathcal{S}} = \boldsymbol{\xi}_{\mathrm{B}} \cdot \boldsymbol{n}_{\mathcal{S}}$, i.e., the slip gradients in normal direction have to coincide at the GB. This can be observed in Fig. 5.3a for all $h_{\mathrm{B}} \leq h_{\mathrm{A}}$.

Now considering approach II to derive the GB flow condition, Fig. 5.3b and Fig. 5.3c show the exact solutions of the plastic slip $\gamma(x_1)$ in shear direction plotted over the laminate. In contrast to approach I, approach II results in two solutions for the distribution of the plastic slip. Solution II.1 in Fig. 5.3b is similar to the solution obtained from approach I in Fig. 5.3a. In contrast to solution II.1, the distribution of the plastic slip in solution II.2 is not only continuous across the GB for the case of $h_{\mathrm{A}} = h_{\mathrm{B}}$, but also for all $h_{\mathrm{B}} \leq h_{\mathrm{A}}$. The single crystal consistency check is therefore satisfied.

Approach II for the GB flow condition reads for the limit case of vanishing misorientation

$$\left(\boldsymbol{\xi}_{\mathrm{B}} \cdot \boldsymbol{n}_{\mathcal{S}} + \kappa \left(\gamma_{\mathcal{S}\mathrm{A}} - \gamma_{\mathcal{S}\mathrm{B}} \right) \right) \dot{\gamma}_{\mathcal{S}\mathrm{B}} - \left(\boldsymbol{\xi}_{\mathrm{A}} \cdot \boldsymbol{n}_{\mathcal{S}} + \kappa \left(\gamma_{\mathcal{S}\mathrm{A}} - \gamma_{\mathcal{S}\mathrm{B}} \right) \right) \dot{\gamma}_{\mathcal{S}\mathrm{A}} = 0 \,, \tag{5.60}$$

$$\boldsymbol{\xi}_{\mathrm{B}} \cdot \boldsymbol{n}_{\mathcal{S}} - \boldsymbol{\xi}_{\mathrm{A}} \cdot \boldsymbol{n}_{\mathcal{S}} = 0 \,. \tag{5.61}$$

Eq. (5.60) is quadratic in the plastic slips of the GB. Hence, solving for the two unknowns $\gamma_{\mathcal{S}\mathrm{A}}$ and $\gamma_{\mathcal{S}\mathrm{B}}$ results in two solutions obtained by approach II. The additionally introduced flow condition, given in Eq. (5.9), reads that the jump of the slip gradient at the GB correlates to a certain misorientation function, which is zero for the limit case of vanishing misorientation. Consequently, the slip gradients in normal direction of both sides of the GB coincide in both solutions II.1 and II.2,

see Eq. (5.61). The discontinuous solution of the plastic slip in Fig. 5.3b, however, fails the single crystal consistency check.

In order to investigate differences in solutions II.1 and II.2 the displacement field $u_2(x_1)$ for both solutions II.1 and II.2 is shown in Figure 5.4. With the boundary conditions Eqs. (5.53) and (5.54) the distribution of $u_2(x_1)$ for solution II.1 as well as for solution II.2 is continuous at the GBs. The derivatives of the fluctuation field, i.e., $\partial u_2/\partial x_1$, are shown in Fig. 5.5. The displacement field obtained by GB flow condition approach I shows a kink at the GB in case of $h_\mathrm{B} < h_\mathrm{A}$. The same kink is observed for solution II.1 of approach II. In solution II.2, however, the distribution of $u_2(x_1)$ is continuously differentiable at the GB. The differentiability of the displacement field is included in the Hadamard compatibility condition, which is investigated in the following.

Hadamard compatibility condition check

The Hadamard compatibility condition is given by

$$\llbracket \boldsymbol{F} \rrbracket \boldsymbol{P}_\mathcal{S} = \boldsymbol{0}\,, \tag{5.62}$$

with GB projector $\boldsymbol{P}_\mathcal{S} = (\boldsymbol{I} - \boldsymbol{n}_\mathcal{S} \otimes \boldsymbol{n}_\mathcal{S})$, cf., e.g., Gurtin et al. (2010). For the simple shear of the laminate material the displacement field is given as $\boldsymbol{u} = \bar{K} x_2 \boldsymbol{e}_1 + u_2(x_1)\boldsymbol{e}_2$. From this the displacement gradient can be specified by

$$\boldsymbol{H} = \bar{K}(\boldsymbol{e}_1 \otimes \boldsymbol{e}_2) + \frac{\mathrm{d}u_2}{\mathrm{d}x_1}(\boldsymbol{e}_2 \otimes \boldsymbol{e}_1)\,. \tag{5.63}$$

Therefore, the jump of the deformation gradient yields with the assumption of small deformations

$$\llbracket \boldsymbol{F} \rrbracket = \left(\frac{\mathrm{d}u_{2\mathrm{B}}}{\mathrm{d}x_1} - \frac{\mathrm{d}u_{2\mathrm{A}}}{\mathrm{d}x_1} \right) (\boldsymbol{e}_2 \otimes \boldsymbol{e}_1)\,. \tag{5.64}$$

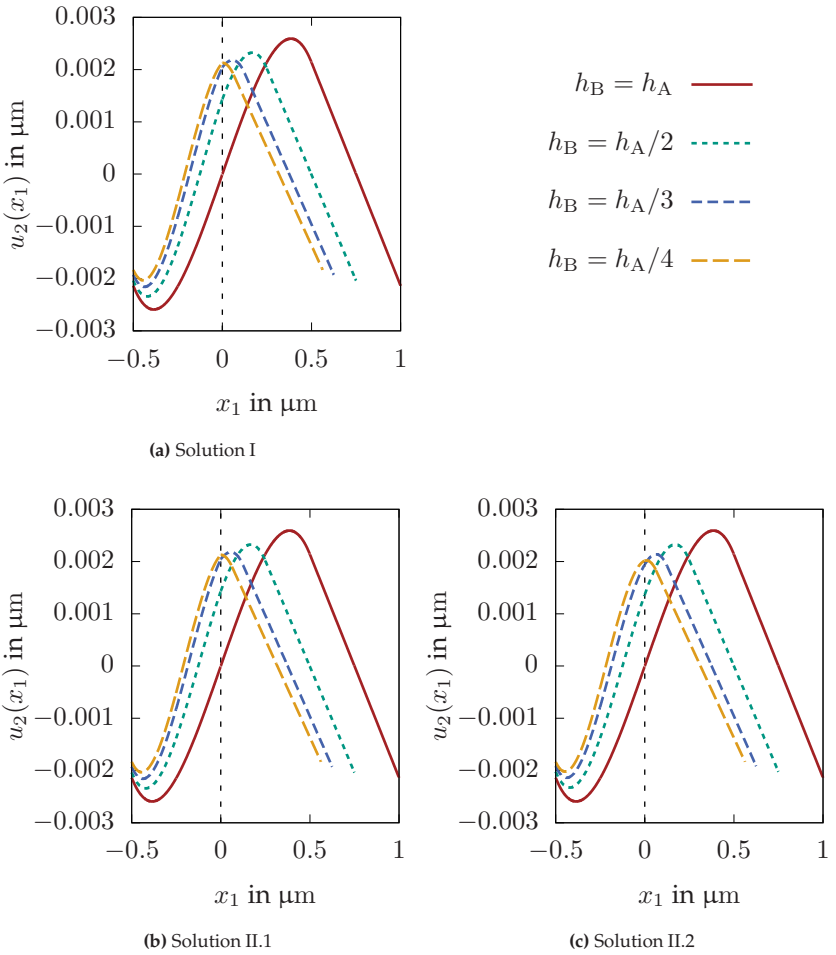

(a) Solution I

(b) Solution II.1

(c) Solution II.2

Figure 5.4: Comparison of GB flow condition approach I (top) and approach II (bottom) for the limit case of vanishing misorientation with a macroscopic shear of $\bar{K} = 0.01$. The exact solutions of the fluctuation fields $u_2(x_1)$ are shown for a varying grain width h_B.

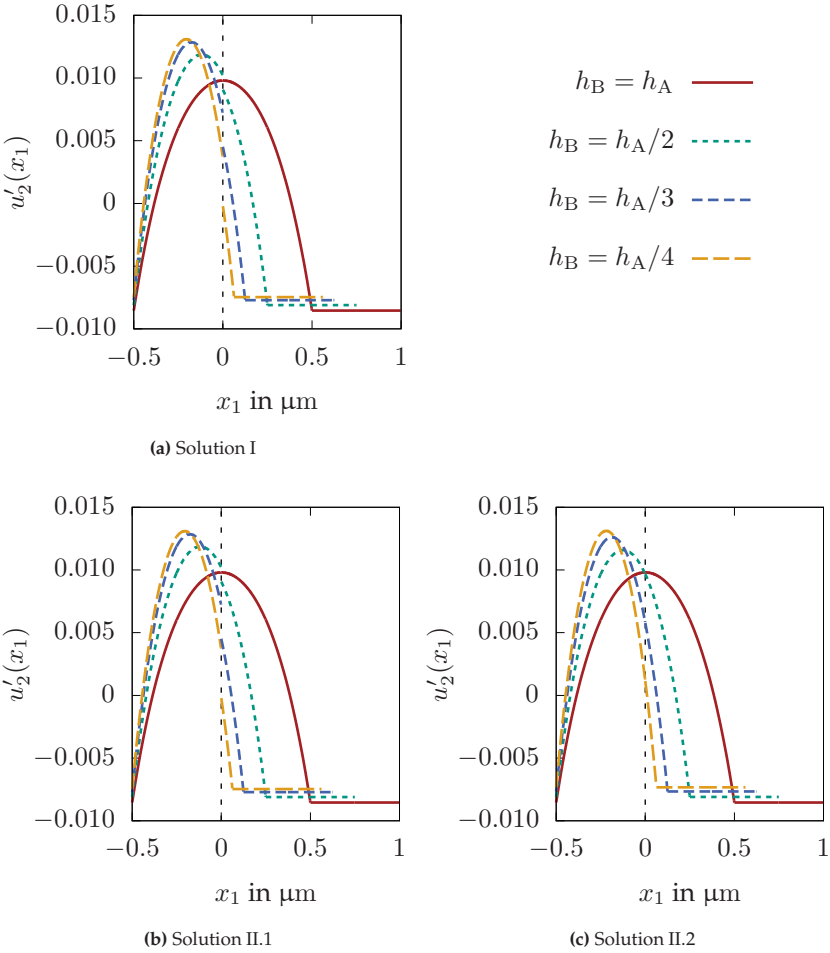

(a) Solution I

(b) Solution II.1

(c) Solution II.2

Figure 5.5: Comparison of GB flow condition approach I (top) and approach II (bottom) for the limit case of vanishing misorientation with a macroscopic shear of $\bar{K} = 0.01$. The exact solutions of the derivatives of the fluctuation fields $\partial u_2/\partial x_1$ are shown for a varying grain width h_B.

For the considered three-phase periodic laminate, the normal vector of the GB is given by $\boldsymbol{n}_{\mathcal{S}} = \boldsymbol{e}_1$. The Hadamard condition reads

$$\begin{aligned}\left[\!\left[\boldsymbol{F}\right]\!\right]\boldsymbol{P}_{\mathcal{S}} &= \left(\frac{\mathrm{d}u_{2\mathrm{B}}}{\mathrm{d}x_1} - \frac{\mathrm{d}u_{2\mathrm{A}}}{\mathrm{d}x_1}\right)(\boldsymbol{e}_2 \otimes \boldsymbol{e}_1)\,(\boldsymbol{e}_2 \otimes \boldsymbol{e}_2 + \boldsymbol{e}_3 \otimes \boldsymbol{e}_3) \\ &= \left(\frac{\mathrm{d}u_{2\mathrm{B}}}{\mathrm{d}x_1} - \frac{\mathrm{d}u_{2\mathrm{A}}}{\mathrm{d}x_1}\right)((\boldsymbol{e}_1 \cdot \boldsymbol{e}_2)\,(\boldsymbol{e}_2 \otimes \boldsymbol{e}_2) + (\boldsymbol{e}_1 \cdot \boldsymbol{e}_3)\,(\boldsymbol{e}_3 \otimes \boldsymbol{e}_3)) \\ &\equiv \boldsymbol{0}\,.\end{aligned} \tag{5.65}$$

Considering the case of no grain misorientation, the Hadamard compatibility condition is therefore trivially fulfilled. Hence, even though the displacement is continuously differentiable at the GB only for solution II.2, the Hadamard compatibility condition is not violated for solution II.1.

5.5.3 Misaligned grains

In the following, the influence of a varying grain misorientation is investigated for GB flow condition approach I and approach II. In order to investigate the influence of the grain misorientation, a variation of the misorientation angle $\vartheta_{\mathrm{A}} = \{0°, 10°, 20°, 30°\}$ is chosen. The three layers of the laminate are equally sized with $h_{\mathrm{A}} = h_{\mathrm{B}} = h_{\mathrm{E}} = 0.5\mu\mathrm{m}$.

Figure 5.6a shows the exact solution of the plastic slip plotted over the laminate structure with the use of GB flow condition approach I. The laminate is exposed to a macroscopic shear strain of $\bar{K} = 0.01$. For the equally sized grains without misorientation the single crystal solution is obtained. For all solutions including a grain misorientation, the distribution of the plastic slip is discontinuous at the GB between the elasto-plastic grains. It can be seen that with increasing grain misorientation angle, the discontinuity of the plastic slip at the GB increases.

With approach II for the GB flow condition, again two solutions for

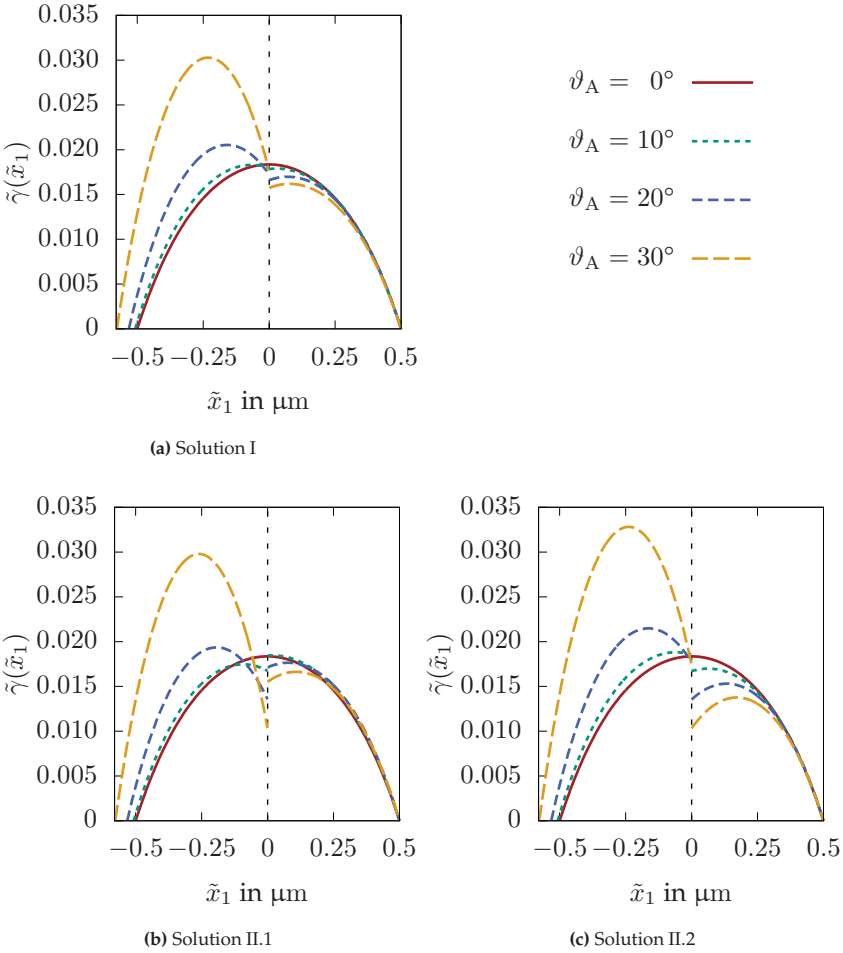

(a) Solution I

(b) Solution II.1

(c) Solution II.2

Figure 5.6: Comparison of GB flow condition approach I (top) and approach II (bottom) for misaligned grains with a macroscopic shear of $\bar{K} = 0.01$. The exact solutions of the plastic slip $\tilde{\gamma}(\tilde{x}_1)$ are shown for a varying misorientation angle ϑ_A.

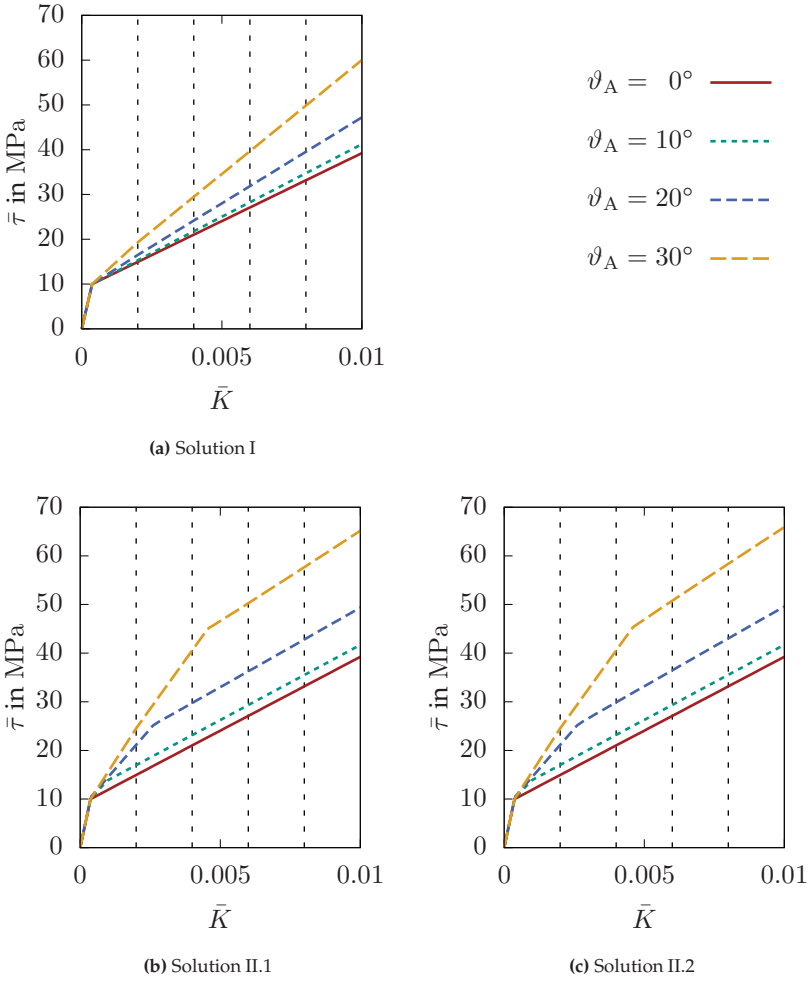

(a) Solution I

(b) Solution II.1

(c) Solution II.2

Figure 5.7: Comparison of GB flow condition approach I (top) and approach II (bottom) for misaligned grains with a macroscopic shear of $\bar{K} = 0.01$. The effective stress-strain curves are shown for a varying misorientation angle ϑ_A.

the plastic slip are obtained. The exact solutions II.1 and II.2 of the plastic slip are shown in Fig. 5.6b and Fig. 5.6c. Both solutions show a discontinuous distribution of the plastic slip for misaligned grains, more distinct than obtained by approach I. In contrast to the investigation of a varying grain size, neither of the two solutions is identical to the solution obtained by GB flow condition approach I. Equivalent to approach I, however, it can be observed that with an increasing misorientation angle, the discontinuity of the plastic slip at the GB increases. Additionally, based on the amount of the grain misorientation, the gradient of plastic slip increases. This can be related to the amount of dislocations, which are piled-up at the GB.

In order to investigate the differences of the solutions obtained by GB flow condition approach I and approach II, the laminate is exposed to an increasing macroscopic shear strain of $\bar{K} \in \{0, \ldots, 0.01\}$. This allows the investigation of the GB states during loading. In Fig. 5.7, the effective stress-strain curves are shown for both GB flow condition approaches. While for approach I, shown in Fig. 5.7a, only two sectors of the stress-strain curve are observable, three GB states can be identified for approach II, which is shown in Figs. 5.7b and 5.7c:

- Elastic: No yield condition is satisfied, therefore, no plastic deformation occurs. The plastic slip is zero.
- Microhard: The yield condition is satisfied only in the bulk material but not in the GB. Dislocations pile-up.
- Microcontrolled: The yield condition is satisfied in the bulk material as well as in the GB. GB plasticity occurs, which is controlled by a GB flow rule.

For GB flow condition approach II the two solutions, II.1 in Fig. 5.7b and II.2 in Fig. 5.7c, show an equivalent stress evolution. The slope of the microhard GB stress evolution is higher for a higher misorientation angle of the adjacent slip system. The most dominant influence of the misorientation angle, however, is the transition point of the microcon-

trolled GB state. The resistance of the GB against dislocation transmission strongly depends on the misorientation function, cf. Eq. (5.9). For $\vartheta_{\mathrm{A}} = 0°$, i.e., limiting case of coinciding slip systems, dislocations can cross the GB without hindrance. Consequently, the GB is microfree after the initial elastic state. The amount of dislocations piled-up at the GB before the critical stress for GB transmission is reached is higher for a higher misorientation angle.

To illustrate the different GB states and the differences between approach I and approach II for the GB flow condition, the distribution of the plastic slip along the x-axis is shown in Fig. 5.8 for the four loading states labeled in Fig. 5.7. Exemplary, the slip distributions are shown for $\vartheta_{\mathrm{A}} = 30°$. For approach I shown in Fig. 5.8a plastic slip evolves at the GB as soon as the initial critical resolved shear stress occurs. Approach II again shows two solutions shown in Fig. 5.8b and Fig. 5.8c. It is important to note that only for the microcontrolled GB state, two solutions are obtained. Both solutions are identical for the microhard GB state, where the GB still acts as an insurmountable obstacle for plastic slip. After a sufficient amount of dislocations piled-up at the GB, the GB flow condition is fulfilled and GB slip is permitted. For this microcontrolled GB state the discontinuity of the plastic slip evolves and two distinct solutions are obtained.

5.5.4 Investigation of size effect

In order to investigate the size effect of the periodic bicrystal the laminate width $h = h_{\mathrm{A}} = h_{\mathrm{B}} = h_{\mathrm{E}}$ is varied between $h = 0.25\mu\mathrm{m}$ and $h = 10\mu\mathrm{m}$. Traditionally, the experimental dependence of the strength of a polycrystal is described by the inverse square-root of grain size via the Hall-Patch relation, cf. Hall (1951). Li et al. (2016), however, investigate various datasets from literature and conclude, that their data strongly supports a simple inverse or logarithmic dependency. Arguments are made against the Hall-Patch approach, whereas the

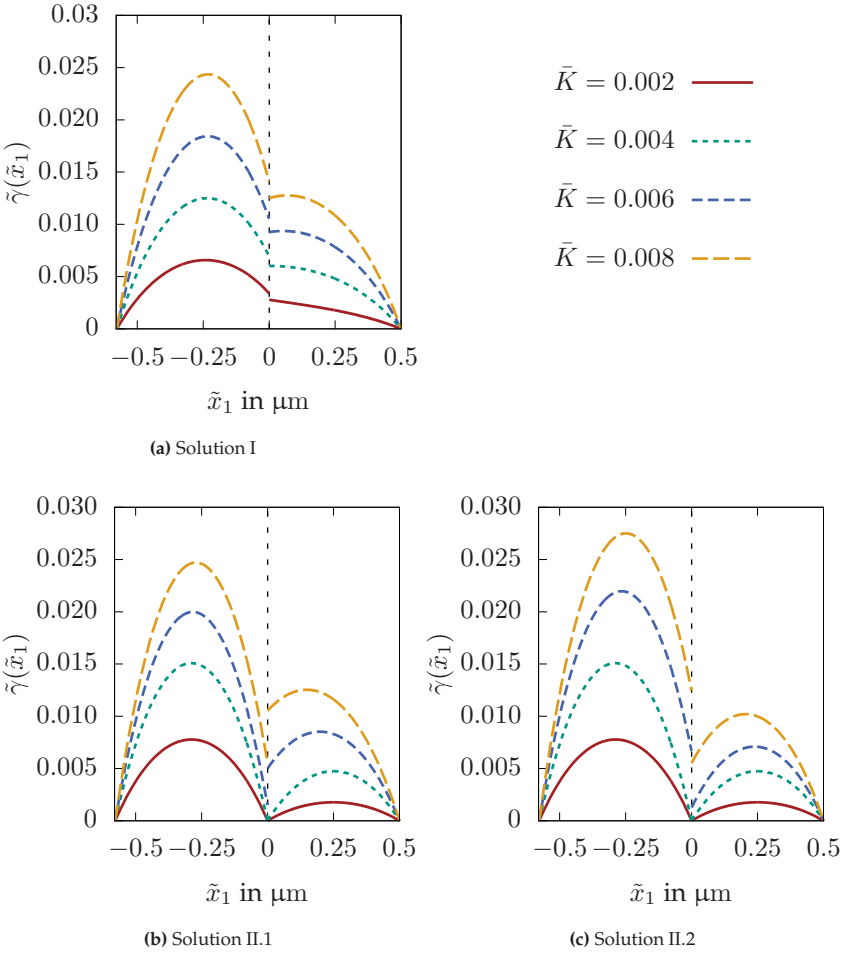

(a) Solution I

(b) Solution II.1

(c) Solution II.2

Figure 5.8: Exact solutions for the evolution of the plastic slip $\tilde{\gamma}(\tilde{x}_1)$ for GB flow condition approach I (top) and approach II (bottom) with grain misorientation $\vartheta_A = 30°$.

simple inverse and logarithmic dependency are supported by underlying dislocation theories. Following Li et al. (2016) the elastic strain $\bar{\varepsilon}_{\mathrm{el}} = \bar{\tau}/G$, i.e., stress normalized by the shear modulus, and normalized width $d = h/a_0$, i.e., laminate width normalized by a lattice constant a_0, are relevant parameters. The lattice constant is chosen to $a_0 = 0.361\mathrm{nm}$. Consequently, the following three size-dependence equations are investigated

$$\bar{\varepsilon}_{\mathrm{el1}} = \bar{\varepsilon}_{01} + \frac{k_1}{\sqrt{d}}\,, \qquad \bar{\varepsilon}_{\mathrm{el2}} = \bar{\varepsilon}_{02} + \frac{k_2}{d}\,, \qquad \bar{\varepsilon}_{\mathrm{el3}} = \bar{\varepsilon}_{03} + \frac{k_3 \ln(d)}{d}\,, \tag{5.66}$$

where $\bar{\varepsilon}_{01}, \bar{\varepsilon}_{02}, \bar{\varepsilon}_{03}$ and k_1, k_2, k_3 are the corresponding fitting parameters. The parameter fit is performed with the nonlinear least-squares fitting procedure in MATLAB.

Fig. 5.9 shows the fitting approaches of Eq. (5.66) for the dependence of elastic strain on the normalized laminate width for $\bar{K} = 0.01$ based on GB flow condition approach I (left) and GB flow condition approach II (right). The corresponding root-mean-square errors are listed in Table 5.1. All three fitting approaches show a good agreement with the analytical results, however, the Hall-Patch approach of $\bar{\varepsilon}_{\mathrm{el1}}$ shows a higher deviation from the analytical results, especially for bigger grain sizes. The simple inverse size-dependence equations, i.e., $\bar{\varepsilon}_{\mathrm{el2}}$, predicts the analytical results best.

The analytical results obtained with GB flow condition approach I and approach II show a similar size-dependency. For small grain sizes, however, the individual volume-averaged stress results differ. For larger sizes the behavior of the bulk material dominates the mechanical response of the periodic three-phase laminate. For small sizes, however, the GB flow condition approach stronger influences the mechanical response. The comparison of $\bar{\varepsilon}_{\mathrm{el}}$ for equal d shows higher strains obtained by GB flow condition approach II.

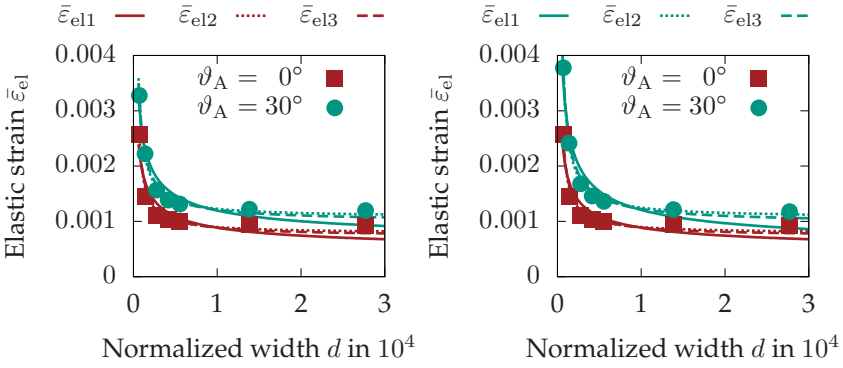

(a) Approach I

(b) Approach II

Figure 5.9: Dependence of the elastic strain $\bar{\varepsilon}_{\mathrm{el}} = \bar{\tau}/G$ on the normalized laminate width $d = h/a_0$ for $\bar{K} = 0.01$ based on GB flow condition approach I (left) and GB flow condition approach II (right). The analytical results are compared to the three fitting approaches of Eq. (5.66), exemplary shown for $\vartheta_{\mathrm{A}} = 0°$ (red) and $\vartheta_{\mathrm{A}} = 30°$ (green).

Table 5.1: Root-mean-square errors for size dependency of the elastic strain $\bar{\varepsilon}_{\mathrm{el}} = \bar{\tau}/G$ according to the three approaches of Eq. (5.66) with GB flow condition approach I and II.

	Approach I			
	$\vartheta_{\mathrm{A}} = 0°$	$\vartheta_{\mathrm{A}} = 10°$	$\vartheta_{\mathrm{A}} = 20°$	$\vartheta_{\mathrm{A}} = 30°$
$\bar{\varepsilon}_{\mathrm{el1}}$ in 10^{-4}	2.46	2.54	2.71	2.18
$\bar{\varepsilon}_{\mathrm{el2}}$ in 10^{-4}	1.15	1.13	1.04	0.55
$\bar{\varepsilon}_{\mathrm{el3}}$ in 10^{-4}	1.50	1.51	1.48	0.88
	Approach II			
	$\vartheta_{\mathrm{A}} = 0°$	$\vartheta_{\mathrm{A}} = 10°$	$\vartheta_{\mathrm{A}} = 20°$	$\vartheta_{\mathrm{A}} = 30°$
$\bar{\varepsilon}_{\mathrm{el1}}$ in 10^{-4}	2.46	2.58	2.82	2.46
$\bar{\varepsilon}_{\mathrm{el2}}$ in 10^{-4}	1.15	1.14	1.02	0.36
$\bar{\varepsilon}_{\mathrm{el3}}$ in 10^{-4}	1.50	1.52	1.50	0.82

5.6 Summary and conclusion

With the gradient crystal plasticity model the dislocation transmission through the GBs is investigated, which is of special interest during the plastic deformation of metal materials. For the modeling of the GBs two approaches are introduced. The common approach to model the interaction of dislocations with GBs as introduced by Gurtin (2008) is based on the assumption of independent plastic slip rates at the GB. It is shown that with the commonly made assumption of independent plastic slip rates at the GB the consistency check for coinciding slip systems is failed. In order to avoid this shortcoming, a second approach to derive the GB condition is introduced. In this new approach, an additional flow condition is applied, where the discontinuity of the plastic slip gradient at the GB correlates to a misorientation function. Applying the new approach to the limit case of vanishing misorientation results in two different solutions. While one solution is an artificial, non-physical solution with strong similarity to the solution obtained by the common approach, the second solution shows a single-crystal response with a continuous and symmetric parabolic distribution of the plastic slip even under variation of the grain size.

Additionally to the consistency check for the limit case of vanishing misorientation, the analytical solutions are compared for misaligned grains. While under assumption of independent plastic slip rates at the GB only a microcontrolled GB state is observed, an additional microhard GB state is identified for the new GB flow condition approach. This microhard state results in a pile-up of dislocations at the GB until the introduced flow condition is satisfied. After the flow condition is satisfied in the bulk as well as in the GB, transmission across the GB occurs and a discontinuous distribution of the plastic slip evolves. Consequently, the two stages of GB behavior which are observed in Sun et al. (1998), i.e., buildup of dislocations near the GB and a vanishing peak at higher strain levels, can be modeled. Both, the critical pile-

up stress for dislocation transmission as well as the amount of slip discontinuity across the GB depend on the GB flow condition, i.e., on the misorientation angle between the two grains.

For both GB flow condition approaches the effect of the laminate width on the mechanical response of the periodic three-phase laminate is investigated. The analytical results show a good agreement with a simple inverse or logarithmic approach, rather than the traditional inverse square-root Hall-Patch approach. This result is supported by Li et al. (2016) where arguments are made against the Hall-Patch approach and the simple inverse and logarithmic approach are supported by underlying dislocation theories.

Chapter 6

Accumulated plastic slip framework

6.1 Introduction and motivation

The following chapter is based on Erdle and Böhlke (2017). A gradient crystal plasticity theory is introduced in a thermo-mechanical framework based on the principle of virtual power. Hereby, the micromorphic approach, as developed in Forest (2009), is used. In the previous sections for each slip system one gradient-stress is introduced in order to account for long range dislocation interactions. Consequently, each slip system requires one additional DOF in the FE implementation for the nonlocal continuum model. Considering all plastic slips massively increases the computational cost compared to a classical continuum mechanical description. To reduce the DOF in crystal simulations, Wulfinghoff and Böhlke (2012) introduce an accumulated plastic slip gradient plasticity model. For details on the computational benefit regarding this approach it is referred to Wulfinghoff et al. (2013). Whereas the model preserves the single crystal slip kinematics, it is restricted to one gradient-stress, associated with the gradient of the accumulated plastic slip, in order to account for long range dislocation interactions. While the gradient of the plastic slip on an individual slip system has a direct physical interpretation in terms of the density of geometrically necessary dislocations, the gradient of the accumulated quantity can only

be interpreted as an approximated measure of the overall dislocation pile-up structure.

Experimental studies, e.g., Lee et al. (1990), have shown discontinuous plastic slips on individual slip systems across GBs. Whereas the accumulated plastic slip is assumed to be continuous in Wulfinghoff et al. (2013), the presented model accounts for discontinuities of the accumulated plastic slip at GBs. The GB flow rule is evaluated at sharp interfaces using discontinuous trial functions in the ABAQUS FE implementation. This approach is based on the theory of the extended FE method, as presented in Fries and Belytschko (2010).

6.2 Model approach

6.2.1 Basic assumptions

Taking the plastic slip on each slip system into account, one additional DOF for each slip system is required. The computational cost of the resulting strongly coupled system of generally non-linear equations is massively increased, compared to a classical continuum mechanical description. In order to reduce the DOF in crystal simulations, a simplified gradient crystal plasticity theory based on an accumulated plastic slip

$$\gamma_{\mathrm{ac}} = \sum_{\alpha=1}^{2N} \int |\dot{\lambda}_\alpha| \, \mathrm{d}t = \sum_{\alpha=1}^{2N} |\lambda_\alpha| \tag{6.1}$$

is introduced in Wulfinghoff et al. (2013). Hereby, for N slip systems $2N$ directional dependent plastic slips λ_α are introduced. The slip parameters are non-decreasing by definition, i.e., $\dot{\lambda}_\alpha \geq 0$. The plastic slip of a slip system is given by the difference between its two directional dependent plastic slips, i.e., $\gamma_\alpha = \lambda_\alpha - \lambda_{\alpha+N}$. Although formally a physical simplification may be associated with a framework based on an accu-

mulated plastic slip, the numerical efficiency is increased notably. The simplification by use of the accumulated plastic slip was tested in various simulations, e.g., Wulfinghoff and Böhlke (2012); Wulfinghoff et al. (2013), where it showed a good agreement with size effects observed in experiments.

Following the work of Forest (2009), the micromorphic variable $\breve{\gamma}_{\mathrm{ac}}$ associated with γ_{ac} is introduced as an additional DOF in order to account for microstructural effects. The concept of introducing a micromorphic medium to account for micro-structural effects is based on the early work of Eringen and Suhubi (1964); Mindlin (1964). The additional DOF, its gradient and the deviation of the micromorphic variable to its associated counterpart contribute to the power of internal forces. For an overview of the micromorphic concept and the general procedure of the enhancement of a continuum to incorporate generalized micromorphic gradient effects it is referred to Forest (2009); Forest et al. (2011).

6.2.2 Principle of virtual power

Based on Eq. (4.24) the following contributions of the bulk material and the GBs are assumed to define the microscopic system. The bulk material contributions are given by the Cauchy stress $\boldsymbol{\sigma}$ that expends power conjugate to the velocity gradient $\boldsymbol{L}$, by a scalar micromorphic stress π conjugate to $\dot{\breve{\gamma}}_{\mathrm{ac}}$ and by a vector valued micromorphic stress $\boldsymbol{\xi}$ conjugate to the rate of the micromorphic slip gradient grad $\left(\dot{\breve{\gamma}}_{\mathrm{ac}}\right)$. In addition to internal power in the bulk material, GB micromorphic tractions $\Pi^{\pm}$ are assumed to expend power conjugate to the left-hand limit $\dot{\breve{\gamma}}_{\mathrm{ac}}^{-}$ and the right hand limit $\dot{\breve{\gamma}}_{\mathrm{ac}}^{+}$ of the micromorphic accumulated plastic slip rate at the GBs. Consequently, the power of the internal forces reads

$$\begin{aligned}\mathcal{P}_{\mathrm{int}} = &\int_{\mathcal{V}} \left(\boldsymbol{\sigma}\cdot\boldsymbol{L} + \pi\dot{\breve{\gamma}}_{\mathrm{ac}} + \boldsymbol{\xi}\cdot\operatorname{grad}\left(\dot{\breve{\gamma}}_{\mathrm{ac}}\right)\right)\,\mathrm{d}v \\ &+ \int_{\mathcal{S}} \left(\Pi^{+}\dot{\breve{\gamma}}_{\mathrm{ac}}^{+} + \Pi^{-}\dot{\breve{\gamma}}_{\mathrm{ac}}^{-}\right)\,\mathrm{d}a\,.\end{aligned} \tag{6.2}$$

An alternative form of Eq. (6.2) is obtained with the use of the jump at a GB $\left[\!\left[\dot{\gamma}_{\mathrm{ac}}\right]\!\right] = \dot{\gamma}_{\mathrm{ac}}^{+} - \dot{\gamma}_{\mathrm{ac}}^{-}$ in combination with the mean value at a GB $\left\langle \dot{\gamma}_{\mathrm{ac}} \right\rangle = (\dot{\gamma}_{\mathrm{ac}}^{+} + \dot{\gamma}_{\mathrm{ac}}^{-})/2$. This description of the discontinuity provides an easier interpretation and comparability to existing theories with a continuous solution field, i.e., $\left[\!\left[\dot{\gamma}_{\mathrm{ac}}\right]\!\right] \to 0$, $\left\langle \dot{\gamma}_{\mathrm{ac}} \right\rangle \to \dot{\gamma}_{\mathrm{ac}}$. By using the jump and the mean value of the micromorphic accumulated plastic slip rate, the power of the internal forces reads

$$\begin{aligned} \mathcal{P}_{\mathrm{int}} = \int_{\mathcal{V}} \left(\boldsymbol{\sigma} \cdot \boldsymbol{L} + \pi \dot{\gamma}_{\mathrm{ac}} + \boldsymbol{\xi} \cdot \operatorname{grad}\left(\dot{\gamma}_{\mathrm{ac}}\right) \right) \mathrm{d}v \\ + \int_{\mathcal{S}} \left(\Pi_{\mathrm{j}} \left[\!\left[\dot{\gamma}_{\mathrm{ac}}\right]\!\right] + \Pi_{\mathrm{m}} \left\langle \dot{\gamma}_{\mathrm{ac}} \right\rangle \right) \mathrm{d}a \,, \end{aligned} \tag{6.3}$$

where the work conjugate quantities of the jump and the mean value

$$\Pi_{\mathrm{j}} = \frac{1}{2} \left(\Pi^{+} - \Pi^{-} \right), \qquad \Pi_{\mathrm{m}} = \Pi^{+} + \Pi^{-} \tag{6.4}$$

are introduced. The power of external forces is constructed based on Eq. (4.25). It is assumed that the macroscopic system is defined by a body force density $\varrho \boldsymbol{b}$ and a macroscopic surface traction $\bar{\boldsymbol{t}}$, both conjugate to $\dot{\boldsymbol{u}}$, and by a micromorphic surface traction $\bar{\Xi}$ conjugate to $\dot{\gamma}_{\mathrm{ac}}$. The corresponding parts of the external boundary are denoted by $\partial\mathcal{V}_{\mathrm{t}}$ and $\partial\mathcal{V}_{\Xi}$, respectively. Consequently, the external power has the form

$$\mathcal{P}_{\mathrm{ext}} = \int_{\mathcal{V}} \varrho \boldsymbol{b} \cdot \dot{\boldsymbol{u}} \, \mathrm{d}v + \int_{\partial\mathcal{V}_{\mathrm{t}}} \bar{\boldsymbol{t}} \cdot \dot{\boldsymbol{u}} \, \mathrm{d}a + \int_{\partial\mathcal{V}_{\Xi}} \bar{\Xi} \dot{\gamma}_{\mathrm{ac}} \, \mathrm{d}a \,. \tag{6.5}$$

The principle of virtual power is constructed in a similar manner to Section 4.3.1. With the application of divergence theorem the power

balance reads

$$\begin{aligned}\int_{\mathcal{V}} \left(\pi - \operatorname{div}(\boldsymbol{\xi})\right) \delta\dot{\breve{\gamma}}_{\mathrm{ac}} \,\mathrm{d}v - \int_{\mathcal{V}} \left(\varrho\boldsymbol{b} + \operatorname{div}(\boldsymbol{\sigma})\right) \cdot \delta\dot{\boldsymbol{u}} \,\mathrm{d}v \\ - \int_{\mathcal{S}} \left(\Pi_{\mathrm{j}} \left[\!\left[\delta\dot{\breve{\gamma}}_{\mathrm{ac}}\right]\!\right] + \Pi_{\mathrm{m}} \left\langle \delta\dot{\breve{\gamma}}_{\mathrm{ac}} \right\rangle - \left[\!\left[\boldsymbol{\xi}\delta\dot{\breve{\gamma}}_{\mathrm{ac}}\right]\!\right] \cdot \boldsymbol{n}_{\mathcal{S}}\right) \,\mathrm{d}a \\ + \int_{\partial\mathcal{V}_{\Xi}} \left(\boldsymbol{\xi}\cdot\boldsymbol{n} - \bar{\Xi}\right) \delta\dot{\breve{\gamma}}_{\mathrm{ac}} \,\mathrm{d}a + \int_{\partial\mathcal{V}_t} \left(\boldsymbol{\sigma}\boldsymbol{n} - \bar{\boldsymbol{t}}\right) \cdot \delta\dot{\boldsymbol{u}} \,\mathrm{d}a = 0\,,\end{aligned} \tag{6.6}$$

where the virtual solution fields $\{\delta\dot{\boldsymbol{u}}, \delta\dot{\breve{\gamma}}_{\mathrm{ac}}\}$ can be varied arbitrarily. The following local field equations, Neumann conditions and GB condition are obtained

$$\pi - \operatorname{div}(\boldsymbol{\xi}) = 0\,, \qquad \forall \boldsymbol{x} \in \mathcal{V}\,, \tag{6.7}$$

$$\varrho\boldsymbol{b} + \operatorname{div}(\boldsymbol{\sigma}) = \boldsymbol{0}\,, \qquad \forall \boldsymbol{x} \in \mathcal{V}\,, \tag{6.8}$$

$$\Pi_{\mathrm{j}} \left[\!\left[\dot{\breve{\gamma}}_{\mathrm{ac}}\right]\!\right] + \Pi_{\mathrm{m}} \left\langle \dot{\breve{\gamma}}_{\mathrm{ac}} \right\rangle - \left[\!\left[\boldsymbol{\xi}\dot{\breve{\gamma}}_{\mathrm{ac}}\right]\!\right] \cdot \boldsymbol{n}_{\mathcal{S}} = 0\,, \qquad \forall \boldsymbol{x} \in \mathcal{S}\,, \tag{6.9}$$

$$\boldsymbol{\xi}\cdot\boldsymbol{n} - \bar{\Xi} = 0\,, \qquad \forall \boldsymbol{x} \in \partial\mathcal{V}_{\Xi}\,, \tag{6.10}$$

$$\boldsymbol{\sigma}\boldsymbol{n} - \bar{\boldsymbol{t}} = \boldsymbol{0}\,, \qquad \forall \boldsymbol{x} \in \partial\mathcal{V}_t\,. \tag{6.11}$$

6.2.3 Helmholtz free energy

The mass specific Helmholtz free energy of the bulk material ψ is split into four contributions

$$\psi = \psi_{\mathrm{e}}(\boldsymbol{F}_{\mathrm{e}}) + \psi_{\mathrm{h}}(\gamma_{\mathrm{ac}}) + \psi_{\mathrm{g}}(\operatorname{Grad}(\breve{\gamma}_{\mathrm{ac}})) + \psi_{\chi}(\breve{\gamma}_{\mathrm{ac}} - \gamma_{\mathrm{ac}})\,, \tag{6.12}$$

i.e., elastic energy ψ_{e}, isotropic hardening energy ψ_{h}, gradient defect energy ψ_{g} and penalty energy ψ_{χ}, which is of numerical nature.
A Hooke-type elastic contribution is considered

$$\varrho_0\psi_{\mathrm{e}} = \frac{1}{2}\boldsymbol{E}_{\mathrm{e}} \cdot \tilde{\mathbb{C}}[\boldsymbol{E}_{\mathrm{e}}]\,, \tag{6.13}$$

where the reference mass density ϱ_0 is introduced.

Isotropic hardening effects of the bulk material are modeled through the phenomenological hardening energy

$$\begin{aligned} \varrho_0\psi_{\mathrm{h}} &= \frac{1}{2}\Theta_\infty\gamma_{\mathrm{ac}}^2 + (\tau_\infty - \tau_0)\gamma_{\mathrm{ac}} \\ &+ \frac{1}{\Theta_0 - \Theta_\infty}\left(\tau_\infty - \tau_0\right)^2 \exp\left(-\frac{(\Theta_0 - \Theta_\infty)\gamma_{\mathrm{ac}}}{\tau_\infty - \tau_0}\right), \end{aligned} \tag{6.14}$$

cf., e.g., Palm (1951). Hereby, the initial and asymptotic values of the critical resolved yield stress τ_0 and τ_∞ as well as the initial and asymptotic values of hardening modulus Θ_0 and Θ_∞ are introduced as material parameters. For monotonic loading processes, it can be shown that a direct connection exists between the Voce-type bulk material hardening energy and the dislocation-density-based Taylor formulation of hardening, cf. Bayerschen (2016).

Additionally, a gradient defect energy contribution introduces an internal length scale. Examples of defect energy contributions are given in Reddy (2011). Based on the small deformation framework of Wulfinghoff et al. (2013), a quadratic energy contribution based on the gradient of the micromorphic accumulated plastic slip is used

$$\varrho_0\psi_{\mathrm{g}} = \frac{1}{2}K_{\mathrm{g}}\|\mathrm{Grad}\left(\breve{\gamma}_{\mathrm{ac}}\right)\|^2 \tag{6.15}$$

with the defect parameter K_{g} to account for energy of geometrically necessary dislocations. A non-quadratic choice of a power-law defect energy based on the gradient of the accumulated plastic slip is investigated in Bayerschen and Böhlke (2016) for a single-crystal gradient plasticity theory. Note, that in contrary to a defect energy which depends on the sum over gradients of plastic slip, discussed, e.g., in Reddy (2011), Eq. (6.15) depends on the gradient of the sum over plastic slips.

Finally, based on the work of Forest (2009), a numerical penalty energy

$$\varrho_0\psi_\chi = \frac{1}{2}H_\chi(\breve{\gamma}_{\mathrm{ac}} - \gamma_{\mathrm{ac}})^2 \tag{6.16}$$

is introduced. The penalty energy penalizes deviations of the micromorphic accumulated plastic slip $\breve{\gamma}_{\mathrm{ac}}$ from the associated counterpart γ_{ac} by a large penalty factor H_χ and consequently ensures the coupling of both variables.

An additional energy contribution is assumed to arise from the GB resistance to plastic flow. The GB energy is assumed to depend on the jump and the mean value of the micromorphic accumulated plastic slip. In the following, the special case of a linear GB energy is considered

$$\varrho_{\mathcal{S}0}\psi_{\mathcal{S}} = K_{\mathrm{j}}\left[\!\left[\breve{\gamma}_{\mathrm{ac}}\right]\!\right] + K_{\mathrm{m}}\left\langle\breve{\gamma}_{\mathrm{ac}}\right\rangle , \tag{6.17}$$

with reference GB mass density $\varrho_{\mathcal{S}0}$ and material parameters K_{j} and K_{m}. The phenomenological approach of Eq. (6.17) accounts for a discontinuous distribution of the micromorphic accumulated plastic slip. This is an extension of the linear GB energy based on the accumulated plastic slip used in Wulfinghoff et al. (2013). As a consequence of the linear dependency of the GB energy on the jump and the mean value of the micromorphic accumulated plastic slip, GB hardening is neglected. The hardening extension of the GB with a quadratic GB energy contribution is investigated in Bayerschen et al. (2015). Since the parameters K_{j} and K_{m} do not depend on the misorientation of slip systems at GBs, orientational effects are neglected. This is a major difference to the GB energy of Gurtin (2008) investigated in Section 5.2.

6.2.4 Clausius-Duhem inequality and flow rules

The dissipation inequality for the bulk material and the GBs is given with Eq. (4.35) by

$$\int_{\mathcal{V}_0} \varrho_0\dot{\psi}\,\mathrm{d}V \leq \mathcal{P}_{\mathrm{ext}0}(\mathcal{V}_0)\,, \qquad \int_{\mathcal{S}_0} \varrho_{\mathcal{S}0}\dot{\psi}_{\mathcal{S}}\,\mathrm{d}A \leq \mathcal{P}_{\mathrm{ext}0}(\mathcal{S}_0)\,, \tag{6.18}$$

where $\mathcal{P}_{\text{ext0}}(\mathcal{V}_0)$ denotes the external power expended on the bulk material in the reference configuration and $\mathcal{P}_{\text{ext0}}(\mathcal{V}_0)$ denotes the external power expended on the GBs in the reference configuration. By a transformation of Eq. (6.3) the internal energy contribution with respect to the reference placement is obtained

$$\begin{aligned}\mathcal{P}_{\text{int0}} = \int_{\mathcal{V}_0} \left(\boldsymbol{S}\cdot\dot{\boldsymbol{E}} + \pi_0\dot{\breve{\gamma}}_{\text{ac}} + \boldsymbol{\xi}_0\cdot\text{Grad}\left(\dot{\breve{\gamma}}_{\text{ac}}\right)\right)\,\mathrm{d}V \\ + \int_{\mathcal{S}_0}\left(\Pi_{\text{j0}}\left[\dot{\breve{\gamma}}_{\text{ac}}\right] + \Pi_{\text{m0}}\left\langle\dot{\breve{\gamma}}_{\text{ac}}\right\rangle\right)\,\mathrm{d}A\,.\end{aligned} \tag{6.19}$$

The stresses in the reference placement read

$$\begin{aligned}\boldsymbol{S} = \det(\boldsymbol{F})\boldsymbol{F}^{-1}\boldsymbol{\sigma}\boldsymbol{F}^{-\mathsf{T}}\,,\quad \pi_0 = \det(\boldsymbol{F})\pi\,,\quad \boldsymbol{\xi}_0 = \det(\boldsymbol{F})\boldsymbol{F}^{-1}\boldsymbol{\xi}\,,\\ \Pi_{\text{j0}} = \det(\boldsymbol{F})\Pi_{\text{j}}\,,\quad \Pi_{\text{m0}} = \det(\boldsymbol{F})\Pi_{\text{m}}\,.\end{aligned} \tag{6.20}$$

Bulk material

With Eqs. (6.13)–(6.16) if follows

$$\begin{aligned}\dot{\psi} = \frac{\partial\psi_{\text{e}}}{\partial\boldsymbol{E}}\cdot\dot{\boldsymbol{E}} + \frac{\partial\psi_{\text{e}}}{\partial\boldsymbol{F}_{\text{p}}}\cdot\dot{\boldsymbol{F}}_{\text{p}} + \left(\frac{\partial\psi_{\text{h}}}{\partial\gamma_{\text{ac}}} + \frac{\partial\psi_{\chi}}{\partial\gamma_{\text{ac}}}\right)\dot{\gamma}_{\text{ac}} \\ + \frac{\partial\psi_{\chi}}{\partial\breve{\gamma}_{\text{ac}}}\dot{\breve{\gamma}}_{\text{ac}} + \frac{\partial\psi_{\text{g}}}{\partial\text{Grad}\left(\breve{\gamma}_{\text{ac}}\right)}\cdot\text{Grad}\left(\dot{\breve{\gamma}}_{\text{ac}}\right)\,.\end{aligned} \tag{6.21}$$

Inserting the derivation of the Helmholtz free energy into the Clausius Duhem inequality of the bulk material, given in Eq. (6.18), results in

$$\begin{aligned}\mathcal{D} = \left(\boldsymbol{S} - \frac{\partial\varrho_0\psi_{\text{e}}}{\partial\boldsymbol{E}}\right)\cdot\dot{\boldsymbol{E}} + \left(\pi_0 - \frac{\partial\varrho_0\psi_{\chi}}{\partial\breve{\gamma}_{\text{ac}}}\right)\dot{\breve{\gamma}}_{\text{ac}} \\ + \left(\boldsymbol{\xi}_0 - \frac{\partial\varrho_0\psi_{\text{g}}}{\partial\text{Grad}\left(\breve{\gamma}_{\text{ac}}\right)}\right)\cdot\text{Grad}\left(\dot{\breve{\gamma}}_{\text{ac}}\right) \\ - \frac{\partial\varrho_0\psi_{\text{e}}}{\partial\boldsymbol{F}_{\text{p}}}\cdot\dot{\boldsymbol{F}}_{\text{p}} - \left(\frac{\partial\varrho_0\psi_{\text{h}}}{\partial\gamma_{\text{ac}}} + \frac{\partial\varrho_0\psi_{\chi}}{\partial\gamma_{\text{ac}}}\right)\dot{\gamma}_{\text{ac}} \geq 0\,,\end{aligned} \tag{6.22}$$

where the power balance and Eq. (6.19) are used. The assumption of purely energetic stresses $\boldsymbol{S}$, π_0 and $\boldsymbol{\xi}_0$ results in the potential relations

$$\boldsymbol{S} = \frac{\partial \varrho_0 \psi_\mathrm{e}}{\partial \boldsymbol{E}_\mathrm{e}} \frac{\partial \boldsymbol{E}_\mathrm{e}}{\partial \boldsymbol{E}} = \boldsymbol{F}_\mathrm{p}^{-1} \tilde{\mathbb{C}}[\boldsymbol{E}_\mathrm{e}] \boldsymbol{F}_\mathrm{p}^{-\mathsf{T}} \,, \tag{6.23}$$

$$\pi_0 = \frac{\partial \varrho_0 \psi_\chi}{\partial \breve{\gamma}_\mathrm{ac}} = H_\chi (\breve{\gamma}_\mathrm{ac} - \gamma_\mathrm{ac}) \,, \tag{6.24}$$

$$\boldsymbol{\xi}_0 = \frac{\partial \varrho_0 \psi_\mathrm{g}}{\partial \mathrm{Grad}\,(\breve{\gamma}_\mathrm{ac})} = K_\mathrm{g} \mathrm{Grad}\,(\breve{\gamma}_\mathrm{ac}) \,. \tag{6.25}$$

Furthermore, the reduced dissipation inequality of the bulk material

$$\mathcal{D}_\mathrm{red} = -\frac{\partial \varrho_0 \psi_\mathrm{e}}{\partial \boldsymbol{F}_\mathrm{p}} \cdot \dot{\boldsymbol{F}}_\mathrm{p} - \left(\frac{\partial \varrho_0 \psi_\mathrm{h}}{\partial \gamma_\mathrm{ac}} + \frac{\partial \varrho_0 \psi_\chi}{\partial \gamma_\mathrm{ac}} \right) \dot{\gamma}_\mathrm{ac} \geq 0 \tag{6.26}$$

is obtained. The following notations are introduced for the derivative of the isotropic hardening energy density and the penalty energy by the accumulated plastic slip

$$\beta \coloneqq \frac{\partial \varrho_0 \psi_\mathrm{h}}{\partial \gamma_\mathrm{ac}} \,, \qquad \breve{p} \coloneqq \frac{\partial \varrho_0 \psi_\chi}{\partial \gamma_\mathrm{ac}} \,. \tag{6.27}$$

Consequently, Eq. (6.26) can be written as

$$\mathcal{D}_\mathrm{red} = \boldsymbol{M}_\mathrm{e} \cdot \boldsymbol{L}_\mathrm{p} - (\beta + \breve{p})\, \dot{\gamma}_\mathrm{ac} \geq 0 \,, \tag{6.28}$$

where the Mandel stress $\boldsymbol{M}_\mathrm{e} = \boldsymbol{F}_\mathrm{e}^{\mathsf{T}} \boldsymbol{F}_\mathrm{e} \boldsymbol{S}_\mathrm{e}$ is introduced. Based on the Mandel stress the resolved shear stress of slip system α is given as $\tau_\alpha = \boldsymbol{M}_\mathrm{e} \cdot \tilde{\boldsymbol{M}}_\alpha$. Eq. (6.28) motivates the bulk material flow rule

$$\dot{\lambda}_\alpha = \dot{\lambda}_0 \left\{ \frac{\tau_\alpha - \breve{p} - (\beta + \tau_0)}{\tau_\mathrm{D}} \right\}^p \,, \tag{6.29}$$

where $\{\cdot\}$ denotes the Macaulay bracket with property $\{\cdot\} = \max(\cdot, 0)$. Hereby, the reference shear rate $\dot{\lambda}_0$, the initial critical shear stress τ_0, the

drag stress τ_{D} and the slip rate sensitivity p are introduced as material parameters.

Grain boundaries

With Eqs. (6.17), (6.18) and (6.19) the GB dissipation per unit area reads

$$\mathcal{D}_{\mathcal{S}} = \left(\Pi_{\mathrm{j}0} - \frac{\partial \varrho_{\mathcal{S}0} \psi_{\mathcal{S}}}{\partial \left[\!\left[\breve{\gamma}_{\mathrm{ac}} \right]\!\right]} \right) \left[\!\left[\dot{\breve{\gamma}}_{\mathrm{ac}} \right]\!\right] + \left(\Pi_{\mathrm{m}0} - \frac{\partial \varrho_{\mathcal{S}0} \psi_{\mathcal{S}}}{\partial \left\langle \breve{\gamma}_{\mathrm{ac}} \right\rangle} \right) \left\langle \dot{\breve{\gamma}}_{\mathrm{ac}} \right\rangle \geq 0 \,. \tag{6.30}$$

The energetic GB micromorphic tractions are given as

$$\Pi^{\mathrm{e}}_{\mathrm{j}0} = \frac{\partial \varrho_{\mathcal{S}0} \psi_{\mathcal{S}}}{\partial \left[\!\left[\breve{\gamma}_{\mathrm{ac}} \right]\!\right]} = K_{\mathrm{j}} \,, \qquad \Pi^{\mathrm{e}}_{\mathrm{m}0} = \frac{\partial \varrho_{\mathcal{S}0} \psi_{\mathcal{S}}}{\partial \left\langle \breve{\gamma}_{\mathrm{ac}} \right\rangle} = K_{\mathrm{m}} \,. \tag{6.31}$$

With the GB condition, given in Eq. (6.9), and under the assumption of dissipation free GBs, the GB dissipation inequality results in

$$\begin{aligned} 0 = &\left(K_{\mathrm{g}} \left\langle \mathrm{Grad}\left(\breve{\gamma}_{\mathrm{ac}} \right) \right\rangle \cdot \boldsymbol{n}_{\mathcal{S}0} - K_{\mathrm{j}} \right) \left[\!\left[\dot{\breve{\gamma}}_{\mathrm{ac}} \right]\!\right] \\ &+ \left(K_{\mathrm{g}} \left[\!\left[\mathrm{Grad}\left(\breve{\gamma}_{\mathrm{ac}} \right) \right]\!\right] \cdot \boldsymbol{n}_{\mathcal{S}0} - K_{\mathrm{m}} \right) \left\langle \dot{\breve{\gamma}}_{\mathrm{ac}} \right\rangle . \end{aligned} \tag{6.32}$$

The rate independent GB yield criteria are specified by

$$\varphi_{\mathrm{j}} \coloneqq K_{\mathrm{g}} \left\langle \mathrm{Grad}\left(\breve{\gamma}_{\mathrm{ac}} \right) \right\rangle \cdot \boldsymbol{n}_{\mathcal{S}0} - K_{\mathrm{j}} \,, \tag{6.33}$$

$$\varphi_{\mathrm{m}} \coloneqq K_{\mathrm{g}} \left[\!\left[\mathrm{Grad}\left(\breve{\gamma}_{\mathrm{ac}} \right) \right]\!\right] \cdot \boldsymbol{n}_{\mathcal{S}0} - K_{\mathrm{m}} \,. \tag{6.34}$$

From this the loading conditions for Eq. (6.32) can be formulated in the Kuhn-Tucker form with

$$\varphi_{\mathrm{j}} \left[\!\left[\dot{\breve{\gamma}}_{\mathrm{ac}} \right]\!\right] = 0 \,, \qquad \varphi_{\mathrm{j}} \leq 0 \,, \qquad \left[\!\left[\dot{\breve{\gamma}}_{\mathrm{ac}} \right]\!\right] \geq 0 \,, \tag{6.35}$$

$$\varphi_{\mathrm{m}} \left\langle \dot{\breve{\gamma}}_{\mathrm{ac}} \right\rangle = 0 \,, \qquad \varphi_{\mathrm{m}} \leq 0 \,, \qquad \left\langle \dot{\breve{\gamma}}_{\mathrm{ac}} \right\rangle \geq 0 \,. \tag{6.36}$$

6.3 Finite element implementation

6.3.1 Enrichment of shape functions

In the following the enrichment of FEs for discontinuous solution fields across GBs is discussed. In order to model a discontinuous displacement field of crack simulations, an enrichment of the classical FE approximation is presented in Moës et al. (1999). A generalization of the model for arbitrary discontinuities, called extended FE method, is introduced in Belytschko et al. (2001). An alternative approach to the enrichment of FEs would be the cohesive interface approach, based on the pioneer works of Barenblatt (1959). This approach is widely used for a continuum mechanical theories, e.g., in Gurtin and Anand (2008) for dislocation-based inelastic processes by slip and separation at inter-crystalline GBs. The extended FE method used in this work, however, has the advantage that the FE mesh does not need to conform to the polycrystal topology, cf., e.g., Simone et al. (2006). This allows the modeling of various crystalline structures or evolving interfaces without remeshing.

The micromorphic accumulated plastic slip field is approximated by the standard FE $\breve{\gamma}_{\mathrm{ac}}(\boldsymbol{x}) = \underline{N}^{\gamma}(x)\underline{\hat{\gamma}}$ and the additional nodal unknowns $\underline{\hat{\delta}}$ to account for discontinuities. Therefore, the general structure of shape function enrichment reads

$$\breve{\gamma}_{\mathrm{ac}}(\boldsymbol{x}) = \underbrace{\sum_{i\in \mathrm{I}_{\mathcal{V}}} N_i^{\gamma}(\boldsymbol{x})\hat{\gamma}_i}_{\text{standard FE}} + \underbrace{\sum_{i\in \mathrm{I}_{\mathcal{V}}} \overbrace{\bar{N}_i^{\delta}(\boldsymbol{x})\left(\phi(\boldsymbol{x}) - \phi(\boldsymbol{x}_i)\right)}^{N_i^{\delta}(\boldsymbol{x})} \hat{\delta}_i}_{\text{enrichment}}, \tag{6.37}$$

where $\mathrm{I}_{\mathcal{V}}$ is the set of all nodes and $\phi(\boldsymbol{x})$ denotes the enrichment function, cf., Fries and Belytschko (2010). The enrichment function is evaluated at the integration points as well as at the nodes of the FE $\boldsymbol{x}_i, \forall i \in \mathrm{I}_{\mathcal{V}}$.

Due to the choice of the enrichment term, the standard FE approximation is retained for FEs which do not contain a GB. Based on the choice of the enrichment function, the solution field is either decoupled completely (strong discontinuity), or the solution is continuous while allowing for kinks across interfaces (weak discontinuity). Typical choices for the enrichment function for both weak discontinuities and strong discontinuities are given in Fries and Belytschko (2010). In this work the strong discontinuities of the accumulated plastic slip field are modeled with the sign of the level-set function

$$\phi(\boldsymbol{x}) = \begin{cases} -1, & (\boldsymbol{x} - \boldsymbol{x}_{\mathcal{S}}) \cdot \boldsymbol{n}_{\mathcal{S}} < 0\,, \\ 0, & (\boldsymbol{x} - \boldsymbol{x}_{\mathcal{S}}) \cdot \boldsymbol{n}_{\mathcal{S}} = 0\,, \\ 1, & (\boldsymbol{x} - \boldsymbol{x}_{\mathcal{S}}) \cdot \boldsymbol{n}_{\mathcal{S}} > 0\,. \end{cases} \tag{6.38}$$

In general, the level-set function is capable to model dynamic surfaces, cf., Osher and Fedkiw (2001). In the work at hand, however, GBs are assumed as fixed material singular surfaces.

6.3.2 Discretization of grain boundaries

In the following a mesh-independent GB discretization is introduced. The construction of grain structures is done by means of the grain-indices of the FE nodes, as illustrated in Fig. 6.1. Consequently, image data, e.g., Electron Backscattered Diffraction scans can be used as a starting point for the simulation. If the grain-indices of a FE vary, a GB is contained which is assigned to integration points depending on predefined cases. Because the structure within a FE is prescribed, the area of the GB inside the FE can be partitioned and allocated to the integration points. Additionally, it is ensured that within one FE, all values of the enrichment function, given in Eq. (6.38), are present. Consequently, the solution field discontinuities are modeled in agreement with Eq. (6.37). An additional DOF is introduced, which represents the

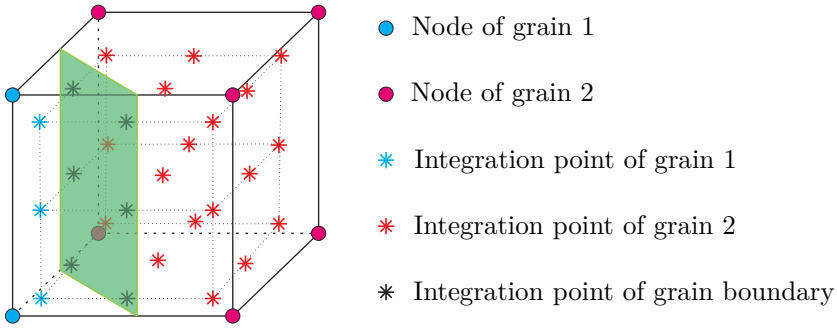

Figure 6.1: Exemplary distribution of nodes and integration points for a three-dimensional eight-node finite element containing a GB.

grain index of each node. In doing so, the local orientation of the GB is obtained by determining the gradient of this indices-field. The gradient of the indices-field is nonzero if and only if a GB is contained inside the FE. In that case, the orientation of the GB can be obtained by a mapping of the additional nodal index DOF with the shape function gradients onto the integration points. The normalization of this gradient results in the direction of the strongest variation of the grain indices which can be defined as the normal vector of the GB. Consequently, it is possible to implement curved or polyhedral surfaces, although the mesh size influences the quality of the surface approximation. As a result of the information about the local orientation of the GB and the discretization of the surfaces with the use of the integration points, a direct allocation and distribution of surface energy is enabled. The GB flow rule, given in Eq. (6.32), is evaluated accurately at the integration points.

6.3.3 Newton scheme

Local Newton scheme

The theory at hand is implemented using the user element interface of ABAQUS CAE. Equivalent to the standard FE procedure with elasto-plastic user materials, the local update of stresses is performed until defined residuals are reached. In this work the update of the Cauchy stress is covered by updating the elastic deformation gradient. With Eqs. (3.14) and (3.15) the first residual equation for the local Newton scheme reads

$$\boldsymbol{r}_1 = \boldsymbol{F}_\mathrm{e} - \boldsymbol{F}_\mathrm{e}^\mathrm{n} - \Delta t \left(\boldsymbol{L}\boldsymbol{F}_\mathrm{e} - \boldsymbol{F}_\mathrm{e} \sum_{\alpha=1}^{2N} \dot{\lambda}_\alpha \tilde{\boldsymbol{M}}_\alpha \right) . \tag{6.39}$$

The subscript n denotes the current time step. The subscript $\mathrm{n}+1$ for quantities of the subsequent time step is dropped. For the generalized relative stress $\breve{p}$, Equations (6.7) and (6.24) imply the additional residuum equation

$$r_2 = \breve{\gamma}_\mathrm{ac} + \frac{\breve{p}}{H_\chi} - \gamma_\mathrm{ac}^\mathrm{n} - \Delta t \sum_{\alpha=1}^{2N} |\dot{\lambda}_\alpha| . \tag{6.40}$$

Eq. (6.39) does not fulfill the necessary condition $\det(\boldsymbol{F}_\mathrm{e}) = \det(\boldsymbol{F})$ resulting from an isochoric plastic deformation, automatically. After an updated $\boldsymbol{F}_\mathrm{e}^*$ fulfilling Eqs. (6.39) and (6.40) is found, the determinant correction is performed

$$\boldsymbol{F}_\mathrm{e} = \boldsymbol{F}_\mathrm{e}^* \left(\frac{\det(\boldsymbol{F})}{\det(\boldsymbol{F}_\mathrm{e}^*)} \right)^{\frac{1}{3}} . \tag{6.41}$$

For consistency with the algorithmic implementation an array-matrix notation is used in the following, where 2nd-order tensors are repre-

sented as arrays, e.g., $\boldsymbol{r}_1 \rightarrow \underline{r}_1$. In order to determine the algorithmic tangent, the total derivatives of the residuum equations, given in Eqs. (6.39) and (6.40), are set to vanish, i.e.,

$$\underline{0} = \frac{\partial \underline{r}_1}{\partial \underline{F}_\mathrm{e}}[\,\mathrm{d}\underline{F}_\mathrm{e}] + \frac{\partial \underline{r}_1}{\partial \breve{p}}\,\mathrm{d}\breve{p} + \frac{\partial \underline{r}_1}{\partial \underline{L}}[\,\mathrm{d}\underline{L}] + \frac{\partial \underline{r}_1}{\partial \breve{\gamma}_\mathrm{ac}}\,\mathrm{d}\breve{\gamma}_\mathrm{ac}\,, \tag{6.42}$$

$$0 = \frac{\partial r_2}{\partial \underline{F}_\mathrm{e}} \cdot \mathrm{d}\underline{F}_\mathrm{e} + \frac{\partial r_2}{\partial \breve{p}}\,\mathrm{d}\breve{p} + \frac{\partial r_2}{\partial \underline{L}} \cdot \mathrm{d}\underline{L} + \frac{\partial r_2}{\partial \breve{\gamma}_\mathrm{ac}}\,\mathrm{d}\breve{\gamma}_\mathrm{ac}\,. \tag{6.43}$$

In matrix-vector notation this reads

$$\begin{pmatrix} \dfrac{\partial \underline{r}_1}{\partial \underline{F}_\mathrm{e}} & \dfrac{\partial \underline{r}_1}{\partial \breve{p}} \\[2ex] \dfrac{\partial r_2}{\partial \underline{F}_\mathrm{e}} & \dfrac{\partial r_2}{\partial \breve{p}} \end{pmatrix} \begin{pmatrix} \mathrm{d}\underline{F}_\mathrm{e} \\[2ex] \mathrm{d}\breve{p} \end{pmatrix} = - \begin{pmatrix} \dfrac{\partial \underline{r}_1}{\partial \underline{L}} & \dfrac{\partial \underline{r}_1}{\partial \breve{\gamma}_\mathrm{ac}} \\[2ex] \dfrac{\partial r_2}{\partial \underline{L}} & \dfrac{\partial r_2}{\partial \breve{\gamma}_\mathrm{ac}} \end{pmatrix} \begin{pmatrix} \mathrm{d}\underline{L} \\[2ex] \mathrm{d}\breve{\gamma}_\mathrm{ac} \end{pmatrix}. \tag{6.44}$$

As a result, the algorithmic tangent for the local Newton scheme is given by

$$\begin{pmatrix} \dfrac{\mathrm{d}\underline{F}_\mathrm{e}}{\mathrm{d}\underline{L}} & \dfrac{\mathrm{d}\underline{F}_\mathrm{e}}{\mathrm{d}\breve{\gamma}_\mathrm{ac}} \\[2ex] \dfrac{\mathrm{d}\breve{p}}{\mathrm{d}\underline{L}} & \dfrac{\mathrm{d}\breve{p}}{\mathrm{d}\breve{\gamma}_\mathrm{ac}} \end{pmatrix} = - \begin{pmatrix} \dfrac{\partial \underline{r}_1}{\partial \underline{F}_\mathrm{e}} & \dfrac{\partial \underline{r}_1}{\partial \breve{p}} \\[2ex] \dfrac{\partial r_2}{\partial \underline{F}_\mathrm{e}} & \dfrac{\partial r_2}{\partial \breve{p}} \end{pmatrix}^{-1} \begin{pmatrix} \Delta t(\underline{I} \square \underline{F}_\mathrm{e}) & 0 \\[2ex] 0 & -1 \end{pmatrix}. \tag{6.45}$$

Global Newton scheme

The computation of the field variables $\underline{u} = \underline{\underline{N}}^u\ \hat{\underline{u}}$ and $\breve{\gamma}_\mathrm{ac} = \underline{N}^\gamma\ \hat{\underline{\gamma}} + \underline{N}^\delta\ \hat{\underline{\delta}}$ on the global level within a FE framework, requires the use of a Newton scheme with associated algorithmic tangent. The weak form of the balance of linear momentum, given in Eq. (6.8), is obtained with a trial

function $\delta \underline{w}^u = \underline{\underline{N}}^u \, \underline{\hat{w}}$ by an integration over an arbitrary volume $\mathcal{V}$

$$0 = \int_{\mathcal{V}} \operatorname{div}(\underline{\sigma}) \cdot \delta \underline{w}^u \, \mathrm{d}v \,, \tag{6.46}$$

$$\underline{r}^u = \int_{\mathcal{V}} \underline{\underline{B}}^{u\,\mathsf{T}} \underline{\sigma} \, \mathrm{d}v - \int_{\mathcal{V}_t} \underline{\underline{N}}^{u\,\mathsf{T}} \bar{\underline{t}} \, \mathrm{d}a \,. \tag{6.47}$$

Hereby, body forces are neglected and the matrix of shape function gradients $\underline{\underline{B}}^u$ is introduced. The weak form of the micromorphic field equation, given in Eq. (6.7), is obtained with the trial function $\delta w^\gamma = \underline{N}^\gamma \, \hat{\underline{w}}$, GB condition and GB flow rule as

$$0 = \int_{\mathcal{V}} \left(\beta - \breve{p} - K_{\mathrm{g}} \operatorname{div}\left(\operatorname{grad}\left(\breve{\gamma}_{\mathrm{ac}}\right)\right)\right) \delta w^\gamma \, \mathrm{d}v \,, \tag{6.48}$$

$$\begin{aligned} r^\gamma = &\int_{\mathcal{V}} \underline{N}^{\gamma\,\mathsf{T}} \left(\beta - \breve{p}\right) \, \mathrm{d}v + \int_{\mathcal{V}} \underline{B}^{\gamma\,\mathsf{T}} K_{\mathrm{g}} \left(\underline{B}^\gamma \hat{\underline{\gamma}} + \underline{B}^\delta \hat{\underline{\delta}}\right) \, \mathrm{d}v \\ &- \int_{\partial \mathcal{V}_\Xi} \underline{N}^{\gamma\,\mathsf{T}} \bar{\Xi} \, \mathrm{d}a + \int_{\mathcal{S}_{\mathrm{act}}} K_{\mathrm{m}} \, \mathrm{d}a \,, \end{aligned} \tag{6.49}$$

where $\mathcal{S}_{\mathrm{act}}$ denotes the plastically active part of the GBs. The enrichment of the accumulated plastic slip by Eq. (6.37) results in an additional equation

$$0 = \int_{\mathcal{V}} \left(\beta - \breve{p} - K_{\mathrm{g}} \operatorname{div}\left(\operatorname{grad}\left(\breve{\gamma}_{\mathrm{ac}}\right)\right)\right) \delta w^\delta \, \mathrm{d}v \,, \tag{6.50}$$

$$\begin{aligned} r^\delta = &\int_{\mathcal{V}} \underline{N}^{\delta\,\mathsf{T}} \left(\beta - \breve{p}\right) \, \mathrm{d}v + \int_{\mathcal{V}} \underline{B}^{\delta\,\mathsf{T}} K_{\mathrm{g}} \left(\underline{B}^\gamma \hat{\underline{\gamma}} + \underline{B}^\delta \hat{\underline{\delta}}\right) \, \mathrm{d}v \\ &- \int_{\partial \mathcal{V}_\Xi} \underline{N}^{\delta\,\mathsf{T}} \bar{\Xi} \, \mathrm{d}a + \int_{\mathcal{S}_{\mathrm{act}}} K_{\mathrm{j}} \, \mathrm{d}a \,, \end{aligned} \tag{6.51}$$

with the trial function $\delta w^\delta = \underline{N}^\delta \, \underline{\hat{w}}$. The residuum equations, given in Eqs. (6.47), (6.49) and (6.51), are solved for $\{\underline{\hat{u}}, \hat{\underline{\gamma}}, \hat{\underline{\delta}}\}$ by a Newton scheme within ABAQUS CAE. Details on the global algorithmic tangent, which is required for this procedure are given in Appendix A.2.

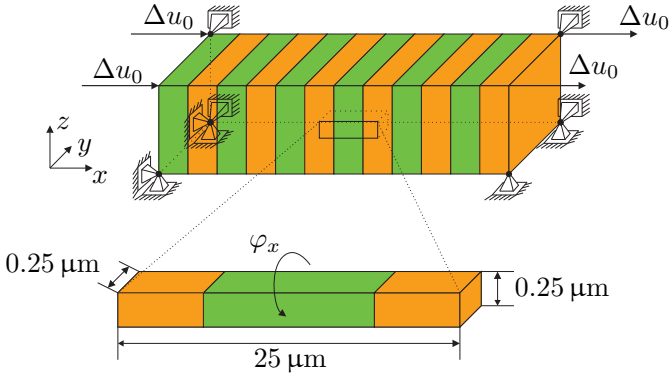

Figure 6.2: Illustration of boundary conditions of laminate microstructure (top) and representative bicrystal (bottom) with periodic boundary conditions.

6.4 Simulation setup

FE simulations are performed for a laminate microstructure, illustrated in Fig. 6.2 (top). By the use of periodic boundary conditions, a representative bicrystal with $25\mu\text{m} \times 0.25\mu\text{m} \times 0.25\mu\text{m}$ in dimension, as illustrated in Fig. 6.2 (bottom), is investigated.

At first, the bicrystal is loaded displacement controlled along the x-axis up to an overall shear strain of 0.05. In order to account for an approximated stationary slip case, an adaptive time stepping algorithm is used during the simulation time of 10^8s. An active set search is performed on the GBs in order to control the convergence of the global Newton scheme. The global Newton scheme is considered to be converged, if the residual tolerance is sufficiently small, and if the set of plastically active GB integration points has not been changed during an iteration. For details on the active set search on the GBs it is referred to Wulfinghoff et al. (2013).

A FCC crystal structure is considered. The stiffness tensor is characterized by the elastic constants $C_{1111} = 168\text{GPa}$, $C_{1122} = 121\text{GPa}$ and

Table 6.1: Model parameters for simple shear simulations of periodic bicrystal.

τ_0	τ_∞	Θ_0	Θ_∞
6MPa	0MPa	330MPa	330MPa
τ_D	$\dot{\gamma}_0$	p	K_g
10MPa	$10^{-3}\mathrm{s}^{-1}$	5	$10^{-2}\mathrm{N}$
K_m	K_j	H_χ	
$100\mathrm{Nm}^{-1}$	$10\mathrm{Nm}^{-1}$	$10^6\mathrm{MPa}$	

$C_{1212} = 75\mathrm{GPa}$. The slip directions and normal vectors of the slip systems are listed in Appendix A.1. The mismatch of slip systems at the GB is realized by a misorientation of adjacent grains. One grain is oriented in a standard $\langle 100 \rangle$-orientation with respect to the x-axis of the Cartesian coordinate system. The adjacent grain is rotated by various angles between $\varphi_x = 0°$ and $\varphi_x = 90°$ along the x-axis. The material parameters of the bulk material and GBs are varied in order to study parameter influences on the mechanical response of the crystalline structure. If not further specified the material parameters are chosen based on Wulfinghoff et al. (2013), where the model parameters for simulations of copper microwire tensile tests were fitted to the experimental data of Yang et al. (2012). The material parameters of this work are listed in Table 6.1. The FE mesh is structured and composed of user-defined, cube-shaped hexahedrons with 27 integration points. For the DOF of the displacement field, quadratic shape functions are used. All additional DOF which represent plastic strain fields or are used for numerical reasons (e.g., indices field), are interpolated with linear shape functions. A convergence study is performed for the simple shear loading of the laminate microstructure with mesh discretizations between 10^3 DOF and 10^5 DOF. The mismatch of adjacent grains is induced by a grain

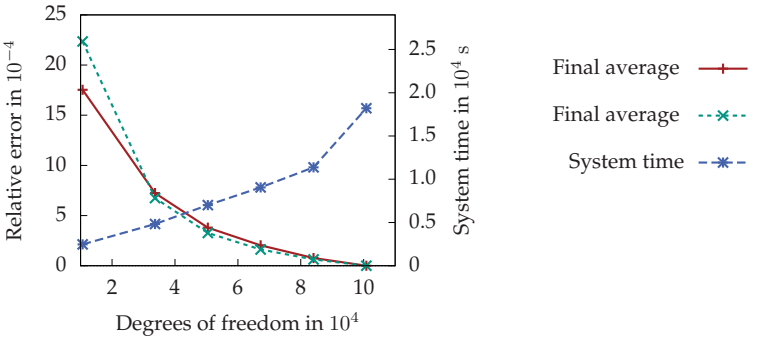

Figure 6.3: Convergence study for a varying mesh discretization of the crystalline structure. A good compromise of the computational time and the accuracy of the results is given for a FE mesh with about 6×10^4 DOF.

rotation angle of $\varphi_x = 45°$. In Fig. 6.3 the influence of a varying mesh on the final average true stress σ_{xz} and on the final average accumulated plastic slip γ_{ac} is shown. A good compromise of the computational time and the accuracy of the results is given for a FE mesh with about 6×10^4 DOF. Consequently, this discretization is used for the following simulations.

6.5 Finite element results

6.5.1 Influence of grain misorientation

In Fig. 6.4 (left) the resulting stress-strain curves are shown for various grain misorientation angles. The three domains of the shear stress evolution, i.e., elastic, microhard and microcontrolled are recognizable. The first domain, until the initial critical shear stress τ_0 is reached, the shear stress only depends on the shear modulus which is almost identical for each grain structure. The critical yield stress at which plastic deformation of the bulk material is initialized, however, varies for different crys-

tal orientations. As soon as the bulk material deforms plastically and while the GB still acts as an insurmountable obstacle for plastic slip, the hardening of the bulk material is a combination of linear isotropic hardening and the hardening induced by dislocation pile-ups. This domain is strongly influenced by the misorientation angle. Even though the misorientation of neighboring grains is not contained in the GB energy in a natural way, the misorientation angle strongly influences the shear stress which allows for dislocation transition across the GB and consequently initializes the third domain. In contrary to Section 5.2, however, the GB does not vanish for a grain misorientation angle $\varphi_x = 0°$. The misorientation of neighboring grains and the orientation of the GBs is not contained in the GB energy in a natural way. Admittedly, no GB would exist between adjacent grains, nonetheless, a resistance of a virtual boundary to the passing of dislocations is considered. A separate consideration of orientational effects is required for a consistent theoretical framework. As soon as the GB flow rule is fulfilled and the loading condition is satisfied, GB slip is permitted. Due to linear dependency of the GB energy and the herewith resulting neglection of GB hardening, the subsequent stress evolution is barely influenced by the misorientation angle of adjacent grains. Additional dislocations arising inside the bulk material are allowed to glide across GBs without additional hindrance.

Fig. 6.4 (right) shows the corresponding final distributions of the micromorphic accumulated plastic slip over the x-axis of the grain structure for various grain misorientation angles φ_x. Due to the symmetry of the periodic bicrystal only one half with a GB located at $x = 6.25\mu\mathrm{m}$ is shown. For equally oriented grains, i.e., $\varphi_x = 0°$, a continuous and symmetric distribution of the micromorphic accumulated plastic slip is obtained. The virtual GB in-between both grains acts as an obstacle until a critical amount of dislocations piled-up and the critical state $\left[\!\left[\boldsymbol{\xi}\right]\!\right] \cdot \boldsymbol{n}_{\mathcal{S}} = K_{\mathrm{j}}$, $\left\langle \boldsymbol{\xi} \right\rangle \cdot \boldsymbol{n}_{\mathcal{S}} = K_{\mathrm{m}}$ is reached. This critical state is not depen-

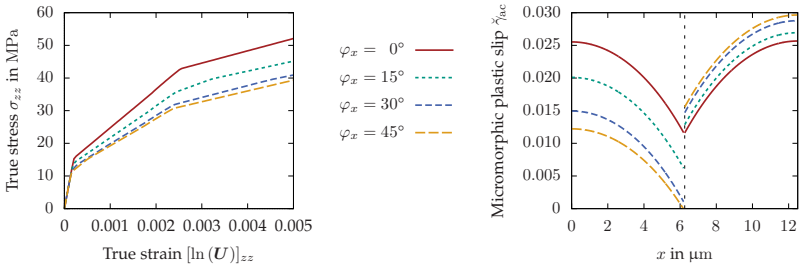

Figure 6.4: Influence of grain misorientation angle φ_x on the mechanical response (left) and corresponding distribution of the final micromorphic accumulated plastic slip $\breve{\gamma}_{\mathrm{ac}}$ over the length of the periodic bicrystal (right).

dent on the misorientation angle between the two grains, consequently, the jump and mean value of the slip gradient in normal direction of the GB are the same for various φ_x values. The discontinuity of the micromorphic accumulated plastic slip, however, strongly depends on the misorientation angle.

6.5.2 Size effect for equally oriented grains

For the following investigations, tensile test simulations are performed for the periodic microstructure, illustrated in Fig. 6.2. The bicrystal is loaded strain controlled up to an overall strain of 0.1 along the z-axis. An adaptive time stepping algorithm is used during the total simulation time of $100\mathrm{s}$. Both grains are considered to be oriented equally in a standard $\langle 100 \rangle$-orientation with respect to the x-axis of the Cartesian coordinate system. In order to investigate the influence of model parameters while neglecting orientational effects, this special case of $\varphi_x = 0°$ is considered. As a consequence of equally oriented grains, a comparison of the numerical results to existing investigations with a GB energy independent of the discontinuity of the accumulated plastic slip at the GB, e.g., Wulfinghoff et al. (2013), is possible. In the following simula-

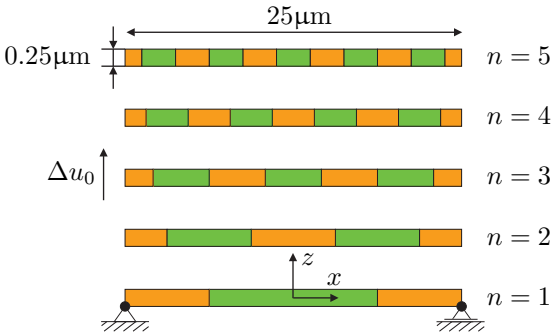

Figure 6.5: Illustration of simulated grain sizes. The grain size is modified by a variation of the number of laminates n inside the $25\mu\mathrm{m}$ periodic structure.

tions, the GB energy parameter associated with the discontinuity of the accumulated plastic slip is neglected, i.e., $K_\mathrm{j} = 0\mathrm{Nm}^{-1}$. The remaining model parameters are chosen as listed in Table 6.1. As illustrated in Fig. 6.5, the size effect is investigated by the variation of the laminate width inside the periodic structure.

Fig. 6.6 shows the influence of the number of laminates n inside the $25\mu\mathrm{m}$ periodic structure on the mechanical response. For a decreasing grain size, the model responds with an increased strength. Consequently, size-effects occurring on the microscale are reproduced. The elastic range of the bulk material is independent of the investigated grain size. The hardening of the bulk material induced by dislocation pile-ups, however, is strongly influenced by the grain size. After GB slip is permitted, the stress evolution is identical for the different grain sizes. Due to the identical orientation of adjacent grains, additional dislocations arising inside the bulk material are allowed to glide across GBs without hindrance.

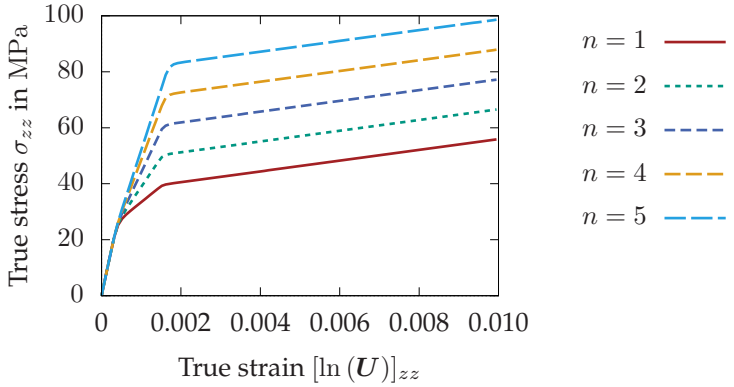

Figure 6.6: Influence of the number of equally sized grains within a crystal structure of identical width on the mechanical response. As illustrated in Fig. 6.5, a higher n correlates to a smaller grain size which results in a higher stress response of the periodic bicrystal under tensile load.

6.5.3 Parameter influences for equally oriented grains

In the following, the influence of the GB energy parameter K_{m} and the defect energy parameter K_{g} on the mechanical response of the periodic bicrystal under tensile load is discussed. In Fig. 6.7 the GB energy parameter K_{m} is varied in a range between $K_{\mathrm{m}} = 0\mathrm{Nm}^{-1}$ and $K_{\mathrm{m}} = 200\mathrm{Nm}^{-1}$, while all other parameters are kept constant. In Fig. 6.7 (left), the stress-strain curves are shown. For $K_{\mathrm{m}} = 0$, no resistance of the GB to the passing of dislocations exists. Consequently, no dislocations pile-up at the GBs. As shown in Fig. 6.7 (right), the corresponding distribution of the final micromorphic accumulated plastic slip is homogeneous over the x-axis of the grain structure. Upon an increase of K_{m}, the second domain of the stress-strain curve in which plastic deformation occurs in the bulk material and the GBs still act as insurmountable obstacles for plastic slip extends, leading to a stiffer material response. The effect of the GB energy parameter on the amount of

dislocations which pile-up at the GBs before the GB flow rule is fulfilled, is clearly evident in Fig. 6.7 (right). As soon as GB slip is permitted, the stress evolution only depends on the multiplication and annihilation effects of statistically stored dislocations. These effects are modeled by the isotropic bulk material hardening energy which is identical for the different GB energy parameters. Consequently, the evolution of the stress-strain curve in the third domain is independent of the choice of K_{m}.

In Fig. 6.8, the parameter of the defect energy K_{g} is varied between $K_{\mathrm{g}} = 10^{-4}\mathrm{N}$ and $K_{\mathrm{g}} = 1\mathrm{N}$, while the GB energy and all other parameters are kept constant. Note that the choice of $K_{\mathrm{g}} = 0\mathrm{N}$ is not valid due to the evaluation of the GB yield condition. The defect energy parameter K_{g} only shows an influence on the second domain of the stress-strain curve. After the GB flow rule is fulfilled, the stress-strain curves coincide. Upon an increase of K_{g}, the pile-up of dislocations at GBs is penalized with an increased energy contribution. Consequently, a higher value of K_{g} results in a more homogeneous distribution of the final micromorphic accumulated plastic slip $\breve{\gamma}_{\mathrm{ac}}$ over the x-axis of the grain structure. For $K_{\mathrm{g}} = 1\mathrm{N}$, the GBs still act as insurmountable obstacles for plastic slip at a true strain of 0.01.

Finally, the influence of the isotropic hardening energy parameter Θ_0 is illustrated in Fig. 6.9. By increasing the isotropic hardening energy, the slope of the stress-strain curve in the third domain is increased. At the same time, the slope in the second domain is slightly increased, as well. Physically, these dependencies are explained by the multiplication and annihilation effects of statistically stored dislocations which occur during the whole plastic range. The effect of dislocation pile-ups at the GBs, however, dominate in the second domain. The corresponding distributions of the micromorphic accumulated plastic slips are shifted along the y-axis to lower slip values, while the influence of the GB is hardly affected.

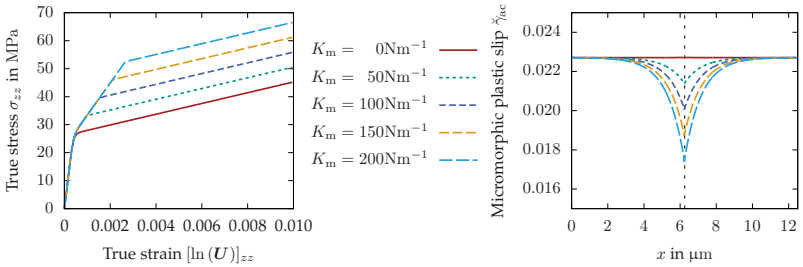

Figure 6.7: Influence of the GB energy parameter K_m on the mechanical response (left) and corresponding distribution of the final micromorphic accumulated plastic slip $\breve{\gamma}_\mathrm{ac}$ over the length of the periodic bicrystal (right).

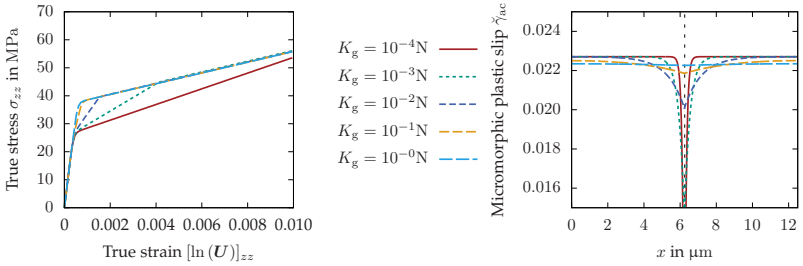

Figure 6.8: Influence of the defect energy parameter K_g on the mechanical response (left) and corresponding distribution of the final micromorphic accumulated plastic slip $\breve{\gamma}_\mathrm{ac}$ over the length of the periodic bicrystal (right).

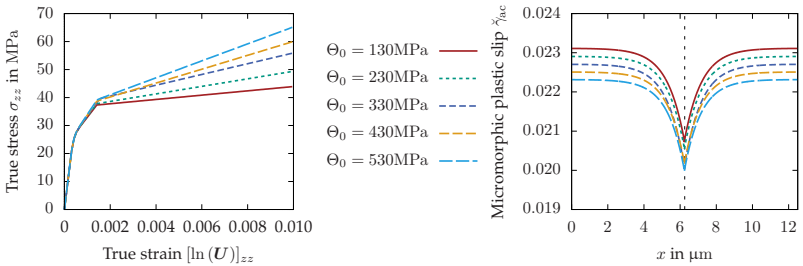

Figure 6.9: Influence of the isotropic hardening energy parameter Θ_0 on the mechanical response (left) and corresponding distribution of the final micromorphic accumulated plastic slip $\breve{\gamma}_\mathrm{ac}$ over the length of the periodic bicrystal (right).

6.6 Summary and conclusion

The presented gradient crystal plasticity, finite strain theory of Erdle and Böhlke (2017) allows the modeling of dislocation phenomena on the microscale of the material. Instead of considering slip gradients on individual slip systems, a gradient-stress associated with the gradient of the micromorphic accumulated plastic slip accounts for long range dislocation interactions. The use of the discontinuous trial function in the FE implementation allows the evaluation of a GB flow rule in due consideration of the misorientation of adjacent grains. In doing so, an energetic contribution of GBs controls the pile-ups of dislocations, without the evaluation of a GB dislocation density tensor. In contrary to the GB energy considered in Chapter 5, the misorientation of neighboring grains and the orientation of the GBs is not contained in the GB energy in a natural way. A separate consideration of orientational effects is required for a consistent theoretical framework.

Different types of energy contributions of the micromorphic, discontinuous field variable and its gradient are modeled. The FE implementation is discussed as well as the influence of the energy parameters on the mechanical response and corresponding distributions of the plastic slip over periodic laminate structures. The presented approach provides a promising numerically efficient framework for large scale FE simulations which includes the grain size dependence of the yield strength.

Chapter 7

Transport mechanisms and grain boundaries

7.1 Introduction and motivation

Recent studies by Hochrainer et al. (2014) introduce the production of the total dislocation density dependent on line curvature as well as the ability to account for dislocation transport within a higher-dimensional continuum dislocation dynamics framework. Based on this framework a thermodynamic formulation is constructed in Hochrainer (2016). By taking the kinematics of dislocations by continuous field variables into account, a physically based theory of crystal plasticity is obtained. Single crystal continuum dislocation dynamic simulations show a good agreement with the experimental studies of micro-bending tests and the discrete dislocation dynamic simulations of Motz et al. (2008). Schulz et al. (2017) show by a comparison with discrete dislocation analyses that the continuum description can capture dislocation interaction processes in a heterogeneous materials. A first three-dimensional numerical implementation with a discontinuous Galerkin scheme is presented in Sandfeld et al. (2015). Wulfinghoff and Böhlke (2015) formulate a three-dimensional FE implementation of the dislocation continuum theory within a gradient crystal plasticity framework. On the basis of the gradient of an accumulated plastic slip, the model is still coupled to 24 partial differential evolution equations of the total dislocation densities

in a FCC crystal. In the following chapter an approach is presented in order to regain a physically motivated framework while preserving the computational benefit of accumulated field variables.

7.2 Dislocation field evolution

7.2.1 Equation of motion

In the following dislocations are considered on a scale where they can be identified individually. Nevertheless, a coarse-grained description is obtained again in a phenomenological sense (cf., e.g., Monavari and Zaiser (2018)). Dislocation climb and dislocation cross-slip is neglected. The motion of a dislocation on a slip system α is considered as a propagating front moving normal to itself with velocity $\boldsymbol{\nu}_\alpha$, i.e., the velocity is orthogonal to the line direction $\boldsymbol{t}_\alpha$ of the dislocation at each point. This implies that the line direction is on the corresponding slip plane α, i.e., $\boldsymbol{t}_\alpha \cdot \boldsymbol{n}_\alpha = 0$. Consequently, the drag force $\boldsymbol{f}_\alpha$ of a dislocation (per unit length) on a slip system α, is related with its velocity $\boldsymbol{\nu}_\alpha$ by a viscous drag coefficient B_α via the relation

$$\boldsymbol{f}_\alpha = -B_\alpha \boldsymbol{\nu}_\alpha = -B_\alpha \nu_\alpha (\boldsymbol{n}_\alpha \times \boldsymbol{t}_\alpha)\,, \tag{7.1}$$

cf. El-Azab (2000). The evolution of a dislocation line is caused by two major effects. On the one hand, the application of external stresses and stresses generated by other crystal defects results in a force acting on a dislocation line. On the other hand, however, the curvature of a dislocation line can also be considered as a contribution to the local internal stress of the dislocation, cf. Mughrabi (2001). Consequently, the velocity of the dislocation line may be a function of the self-interaction caused by the line curvature and of an underlying flow generated by external stresses and by other crystal defects.

In Osher and Sethian (1988) it is shown that equations of motion of propagating fronts with such velocity dependencies resemble Hamilton-Jacobi equations. Let $\Gamma(t)$ be a family of curves, generated by the evolution of a reference curve along an in-plane vector field with velocity v_Γ. The evolution equation of propagating fronts constructed in Osher and Sethian (1988), the so called level-set equation, is based on the level-set function $\phi_\Gamma(\boldsymbol{x}, t)$. The shape and position of a propagating front is uniquely determined as the zero-set of the corresponding level-set function: $\Gamma(t) = \{\boldsymbol{x} \mid \phi_\Gamma(\boldsymbol{x}, t) = 0\}$. A level-set framework for the movement of a curve by curvature is constructed by Ambrosio and Soner (1996), where the mean curvature is introduced as

$$k_\Gamma = -\mathrm{div}\left(\mathrm{grad}\left(\phi_\Gamma\right) \|\mathrm{grad}\left(\phi_\Gamma\right)\|^{-1}\right) . \tag{7.2}$$

Note that $\mathrm{grad}\left(\phi_\Gamma\right)$ is ambiguous for a given zero-set of the level-set function, however, the mean curvature k_Γ is uniquely defined. The level-set equation, constructed by Osher and Sethian (1988), results as

$$\frac{\partial \phi_\Gamma}{\partial t} - v_\Gamma \|\mathrm{grad}\left(\phi_\Gamma\right)\| = 0 . \tag{7.3}$$

For a detailed discussion of the level-set method it is referred to the review article of Osher and Fedkiw (2001).

7.2.2 Local form of the dislocation transport

After a single dislocation has moved through a volume of the crystal on a slip system α, a distortion of the crystalline lattice remains. The absolute value of the Burgers vector b defines the distance of slip caused by the dislocation. The angle φ describes the angle between the line direction and Burgers vector of the dislocation. By the introduction of this angle φ as an additional dimension, dislocations can be described in a higher-dimensional configuration space. The total dislocation den-

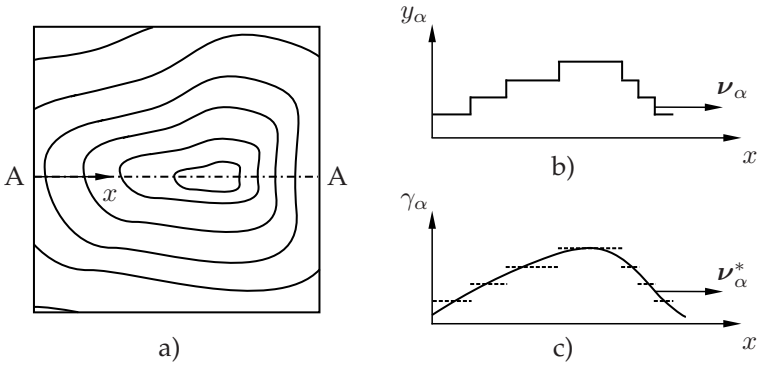

Figure 7.1: a) Discrete dislocation network on slip system α, b) Discrete distortion of the crystal lattice along line A-A with dislocation velocity $\boldsymbol{\nu}_\alpha$, c) Continuous plastic slip along line A-A with velocity of plastic slip field $\boldsymbol{\nu}^*_\alpha$.

sity $\rho^{\mathrm{t}}_\alpha(\boldsymbol{x}, t)$ is expressed in terms of a orientation distribution function $\rho_\alpha(\boldsymbol{x}, t, \varphi)$ for dislocations

$$\rho^{\mathrm{t}}_\alpha(\boldsymbol{x}, t) = \frac{1}{2\pi} \int_0^{2\pi} \varrho_\alpha(\boldsymbol{x}, t, \varphi)\, \mathrm{d}\varphi\,, \tag{7.4}$$

cf. Hochrainer (2013). With the assumption of an isotropic dislocation velocity $\nu_\alpha(\boldsymbol{x}, t, \varphi)$, i.e., $\nu_\alpha(\boldsymbol{x}, t) = \nu_\alpha(\boldsymbol{x}, t, \varphi)$, Hochrainer et al. (2014) construct an evolution of the total dislocation density based on a statistical dislocation density measure. The statistical measure is restricted to dislocation networks where all dislocations form circular loops or straight lines, cf. Hochrainer et al. (2007).

In this work, instead of the construction of an evolution equation based on the higher-dimensional configuration space, continuous plastic slip fields ζ_α representing the distortion of the crystal lattice caused by a network of discrete dislocation lines are considered. For an illustration of this transfer, see Fig. 7.1. As illustrated in Xiang (2009) the density distribution of discrete dislocation lines on each slip plane is identified

by contour curves of a dislocation density potential function after local homogenization. Zhu and Xiang (2015) introduce an additional potential function in order to account for the distribution of the slip planes in the averaged dislocation continuum. In this work, however, it is sufficient to describe the plastic slip on each slip plane and identify the density distribution of dislocation curves in the averaged dislocation continuum. This approach results in a connection between the net length per volume dislocation density on each slip system over a representative volume and the in-plane gradients of plastic slip. Ashby (1970) introduces the density of GND ρ_α^{G} based on the absolute value of the in-plane gradient of plastic slip as

$$\| \mathrm{Grad}^{\mathrm{p}} (\zeta_\alpha) \| = \rho_\alpha^{\mathrm{G}} b \,, \tag{7.5}$$

where $\mathrm{Grad}^{\mathrm{p}} (\zeta_\alpha) = (\boldsymbol{I} - \boldsymbol{n}_\alpha \otimes \boldsymbol{n}_\alpha) \mathrm{Grad} (\zeta_\alpha)$ denotes the in-plane gradient of plastic slip. In Monneau and Patrizi (2012) Hamilton-Jacobi equations which describe dislocations by the Peierls-Nabarro model, cf. Nabarro (1997), are homogenized in order to construct non-local equations for densities of dislocations on the macroscopic scale. This study motivates the application of the level-set approach of Osher and Sethian (1988) to the evolution of the micromorphic plastic slip

$$\frac{\partial \zeta_\alpha}{\partial t} = -\boldsymbol{\nu}_\alpha^* \cdot \mathrm{Grad}^{\mathrm{p}} (\zeta_\alpha) \,, \qquad \boldsymbol{\nu}_\alpha^* = -\nu_\alpha^* \frac{\mathrm{Grad}^{\mathrm{p}} (\zeta_\alpha)}{\| \mathrm{Grad}^{\mathrm{p}} (\zeta_\alpha) \|} \,. \tag{7.6}$$

Hereby $\boldsymbol{\nu}_\alpha^*$ denotes the velocity of the continuous plastic slip field (see also Fig. 7.1). The combination of Eqs. (7.6) and (7.5) results in

$$\frac{\partial \zeta_\alpha}{\partial t} = \rho_\alpha^{\mathrm{G}} b \nu_\alpha^* \,. \tag{7.7}$$

By taking the time derivative on both sides of Eq. (7.5) it follows

$$\frac{\partial \rho_\alpha^{\mathrm{G}}}{\partial t} = -\mathrm{Div}\left(\rho_\alpha^{\mathrm{G}} \boldsymbol{\nu}_\alpha^*\right) - \rho_\alpha^{\mathrm{G}} \nu_\alpha^* \mathrm{Div}\left(\frac{\mathrm{Grad}^{\mathrm{P}}(\zeta_\alpha)}{\|\mathrm{Grad}^{\mathrm{P}}(\zeta_\alpha)\|}\right). \tag{7.8}$$

The first part of the right-hand side of Eq. (7.8) accounts for dislocation transport, while the second part accounts for curvature induced production by the curvature

$$k_\alpha^* = -\mathrm{Div}\left(\frac{\mathrm{Grad}^{\mathrm{P}}(\zeta_\alpha)}{\|\mathrm{Grad}^{\mathrm{P}}(\zeta_\alpha)\|}\right), \tag{7.9}$$

cf., e.g., Xiang (2009). The basic equation of the local dislocation transport is obtained

$$\frac{\partial \rho_\alpha^{\mathrm{G}}}{\partial t} = -\mathrm{Div}\left(\rho_\alpha^{\mathrm{G}} \boldsymbol{\nu}_\alpha^*\right) + \rho_\alpha^{\mathrm{G}} \nu_\alpha^* k_\alpha^*. \tag{7.10}$$

7.3 Coarse-grained dislocation transport

7.3.1 Details on the coarse graining operator

Let V_{c} be a suitable representative volume element whose centroid is located at the origin. Points in V_{c} are denoted by $\boldsymbol{Z}$. The coarse graining operator

$$\bar{\Psi}(\boldsymbol{X}, t) = \langle \Psi(\boldsymbol{Z}, t) \rangle_{\mathrm{c}} := \frac{1}{V_{\mathrm{c}}} \int_{V_{\mathrm{c}}} g(\boldsymbol{X} - \boldsymbol{Z}(t)) \Psi(\boldsymbol{Z}, t)\, \mathrm{d}V \tag{7.11}$$

with the weighting function $g(\boldsymbol{x})$ is introduced. The weighting function is normalized, smooth and vanishes smoothly at points close to $\partial\Omega_{\mathrm{c}}$, i.e.,

$$\frac{1}{V_{\mathrm{c}}} \int_{V_{\mathrm{c}}} g(\boldsymbol{X})\, \mathrm{d}V = 1\,, \qquad \lim_{\|\boldsymbol{X}\| \to \inf} g(\boldsymbol{X}) = 0\,. \tag{7.12}$$

The weighting function is assumed to be isotropic. For details on the coarse graining operator, it is referred to section 2.6 in Nemat-Nasser and Hori (1993). In the following, dependencies of quantities are dropped due to better readability. By introducing the coarse-grained densities of dislocations $\bar{\rho}_\alpha = \langle \rho_\alpha^{\mathrm{G}} \rangle_{\mathrm{c}}$, the time derivative results in

$$\frac{\partial \bar{\rho}_\alpha}{\partial t} = \frac{1}{V_{\mathrm{c}}} \int_{V_{\mathrm{c}}} \frac{\partial g}{\partial t} \rho_\alpha^{\mathrm{G}} + g \frac{\partial \rho_\alpha^{\mathrm{G}}}{\partial t} \, \mathrm{d}V \,. \tag{7.13}$$

It follows

$$\frac{\partial g}{\partial t} = -\frac{\partial g}{\partial (\boldsymbol{X} - \boldsymbol{Z})} \cdot \frac{\partial \boldsymbol{Z}}{\partial t} = -\frac{\partial g}{\partial \boldsymbol{X}} \cdot \frac{\partial \boldsymbol{Z}}{\partial t} \,. \tag{7.14}$$

Consequenty, the first part of Eq. (7.13) results in

$$\begin{aligned} \frac{1}{V_{\mathrm{c}}} \int_{V_{\mathrm{c}}} \frac{\partial g}{\partial t} \rho_\alpha^{\mathrm{G}} \, \mathrm{d}V = \frac{1}{V_{\mathrm{c}}} \int_{V_{\mathrm{c}}} -\frac{\partial g}{\partial \boldsymbol{X}} \cdot \frac{\partial \boldsymbol{z}}{\partial t} \rho_\alpha^{\mathrm{G}} \, \mathrm{d}V \\ = -\frac{1}{V_{\mathrm{c}}} \int_{V_{\mathrm{c}}} \mathrm{Div} \left(g \rho_\alpha^{\mathrm{G}} \frac{\partial \boldsymbol{z}}{\partial t} \right) \mathrm{d}V = -\frac{1}{V_{\mathrm{c}}} \int_{\partial V_{\mathrm{c}}} g \rho_\alpha^{\mathrm{G}} \frac{\partial \boldsymbol{z}}{\partial t} \cdot \, \mathrm{d}\boldsymbol{A} \,. \end{aligned} \tag{7.15}$$

The flux integral over the area of the representative volume element $\partial \Omega_{\mathrm{c}}$ vanishes. It follows that the order of applying the coarse graining operator and differential operators $\mathrm{Div}\,(\cdot)$ and $\mathrm{Grad}\,(\cdot)$ are interchangeable, i.e., $\langle \mathrm{Div}\,(\Psi) \rangle_{\mathrm{c}} = \mathrm{Div}\,(\langle \Psi \rangle_{\mathrm{c}})$ and $\langle \mathrm{Grad}\,(\Psi) \rangle_{\mathrm{c}} = \mathrm{Grad}\,(\langle \Psi \rangle_{\mathrm{c}})$.

7.3.2 Semi-phenomenological dislocation transport

Eq. (7.10) is coarse-grained by means of a representative volume Ω_{c}. This volume is assumed to be time independent. Coarse grained quantities are denoted by $\bar{\Psi} = \langle \Psi \rangle_{\mathrm{c}}$. The coarse-grained form of Eq. (7.10) results in

$$\frac{\partial \bar{\rho}_\alpha}{\partial t} = -\mathrm{Div} \left(\left\langle \rho_\alpha^{\mathrm{G}} \boldsymbol{\nu}_\alpha^* \right\rangle_{\mathrm{c}} \right) + \left\langle \rho_\alpha^{\mathrm{G}} \nu_\alpha^* k_\alpha^* \right\rangle_{\mathrm{c}} \,. \tag{7.16}$$

The velocity ν_α^* is assumed to be homogeneous inside Ω_{c}, i.e. $\nu_\alpha^* = \bar{\nu}_\alpha$, cf. Hochrainer et al. (2014); Monavari and Zaiser (2018). Consequently,

Eq. (7.16) results in

$$\frac{\partial \bar{\rho}_\alpha}{\partial t} = -\mathrm{Div}\left(\bar{\rho}_\alpha \bar{\boldsymbol{\nu}}_\alpha\right) + \left\langle \rho_\alpha^{\mathrm{G}} \nu_\alpha^* k_\alpha^* \right\rangle_{\mathrm{c}} \,, \tag{7.17}$$

with the coarse-grained velocity

$$\bar{\boldsymbol{\nu}}_\alpha = \frac{\left\langle \rho_\alpha^{\mathrm{G}} \boldsymbol{\nu}_\alpha^* \right\rangle_{\mathrm{c}}}{\bar{\rho}_\alpha} = -\frac{\bar{\nu}_\alpha}{b\bar{\rho}_\alpha} \left\langle \mathrm{Grad}^{\mathrm{p}}\left(\zeta_\alpha\right) \right\rangle_{\mathrm{c}} \,. \tag{7.18}$$

The coarse-grained in-plane gradient of plastic slip on slip system α is given by

$$\left\langle \mathrm{Grad}^{\mathrm{p}}\left(\zeta_\alpha\right) \right\rangle_{\mathrm{c}} = \boldsymbol{P}_\alpha \mathrm{Grad}\left(\left\langle \zeta_\alpha \right\rangle_{\mathrm{c}}\right) \,. \tag{7.19}$$

Applying the coarse graining operator to Eq. (7.7), the Orowan equation is obtained

$$\left\langle \frac{\partial \zeta_\alpha}{\partial t} \right\rangle_{\mathrm{c}} = \frac{\partial \langle \zeta_\alpha \rangle_{\mathrm{c}}}{\partial t} = \left\langle \rho_\alpha^{\mathrm{G}} b \nu_\alpha^* \right\rangle_{\mathrm{c}} = \bar{\rho}_\alpha b \bar{\nu}_\alpha \,. \tag{7.20}$$

Micromorphic plastic slips $\breve{\gamma}_\alpha = \langle \zeta_\alpha \rangle_{\mathrm{c}}$ carry the microstructure effect, i.e. the targeted gradient effects. As discussed in Forest (2009), a close connection exists between the micromorphic quantities and the corresponding macro counterparts, i.e. γ_α.

In this work an approach is presented in order to adopt the above physically motivated framework to preserve the computational benefit of accumulated field variables. The numerical implementation by Wulfinghoff and Böhlke (2015) requires 24 dislocation field variables. As opposed to this high computational cost, in this work only two additional field variables, i.e., the accumulated density of dislocations and the accumulated mean curvature, are introduced in order to account for the dislocation transport of Eq. (7.10). Under the assumption of proportional loading with respect to each slip system, Eq. (7.10) can be expressed in terms of accumulated plastic slips on each slip system $\breve{\gamma}_{\mathrm{ac}\alpha}$

and the corresponding in-plane gradient as

$$\frac{\partial \bar{\rho}_\alpha}{\partial t} = \mathrm{Div}\left(\frac{\partial \breve{\gamma}_{\mathrm{ac}\alpha}}{\partial t}\frac{1}{\bar{\rho}_\alpha b^2}\mathrm{Grad}^{\mathrm{p}}\left(\breve{\gamma}_{\mathrm{ac}\alpha}\right)\right) + \left\langle \rho_\alpha^{\mathrm{G}} \nu_\alpha^* k_\alpha^* \right\rangle_{\mathrm{c}} . \tag{7.21}$$

This simplification allows the construction of a model based on the accumulated plastic slip similar to Chapter 6. Note that this assumption does not imply monotonic loading processes, implicitly, but monotonic evolutions of plastic slip on each slip system. As a consequence, if the slip direction of a slip system changes its sign, for example due to a cyclic loading process, no annihilation of dislocations occurs.

In order to formulate the model based on the accumulated plastic slip, it is necessary to formulate an approach connecting the in-plane gradient of the slip on slip system α with the in-plane gradient of the accumulated plastic slip. As an approach the gradient of the accumulated plastic slip is prorated on the individual slip systems by

$$\boldsymbol{P}_\alpha \left(\frac{\partial \breve{\gamma}_{\mathrm{ac}\alpha}}{\partial t}\mathrm{Grad}\left(\breve{\gamma}_{\mathrm{ac}\alpha}\right) - \frac{\bar{\rho}_\alpha}{\bar{\rho}_{\mathrm{ac}}}\frac{\partial \breve{\gamma}_{\mathrm{ac}}}{\partial t}\mathrm{Grad}\left(\breve{\gamma}_{\mathrm{ac}}\right)\right) = \boldsymbol{0} , \tag{7.22}$$

where the accumulated density of dislocations $\bar{\rho}_{\mathrm{ac}} = \sum_\alpha \bar{\rho}_\alpha$ is introduced and $\boldsymbol{P}_\alpha = (\boldsymbol{I} - \boldsymbol{n}_\alpha \otimes \boldsymbol{n}_\alpha)$ denotes the projector onto the slip system α. The approach preserves the slip kinematics of in-plane glide of dislocations on slip systems. It is ensured that the direction of in-plane gradient of slip is preserved. Note, that the sum of the gradients of plastic slip on the individual slip systems is only equal to the sum of the gradient of the accumulated plastic slip if $\sum_\alpha \sum_{\beta\neq\alpha} \dot{\breve{\gamma}}_{\mathrm{ac}\alpha}\mathrm{Grad}\left(\breve{\gamma}_{\beta\mathrm{c}}\right) = \boldsymbol{0}$ is valid. By using this approach it is possible to construct a numerically efficient micromechanical framework based on accumulated field variables which accounts for the transport of dislocations on a coarse-grained scale. Whereas in the model of Wulfinghoff and Böhlke (2015) 24 partial differential evolution equations of the total dislocation

densities in a FCC crystal are introduced, only one additional DOF is needed in the following.

By combining Eqs. (7.7), (7.21) and (7.22), and using $\sum_\alpha \boldsymbol{P}_\alpha = 8\boldsymbol{I}$, the evolution of the density of dislocations on slip system α results in

$$\frac{\partial \bar{\rho}_{\mathrm{ac}}}{\partial t} = \mathrm{Div}\left(\frac{\partial \breve{\gamma}_{\mathrm{ac}}}{\partial t}\frac{8}{\bar{\rho}_{\mathrm{ac}} b^2}\mathrm{Grad}\left(\breve{\gamma}_{\mathrm{ac}}\right)\right) + \sum_{\alpha=1}^{N}\left\langle \rho_\alpha^{\mathrm{G}} \nu_\alpha^* k_\alpha^* \right\rangle_{\mathrm{c}} . \tag{7.23}$$

In the following the coarse-grained curvature induced line length production is neglected inside the representative volume element V_{c}

$$\sum_{\alpha=1}^{N}\left\langle \rho_\alpha^{\mathrm{G}} \nu_\alpha^* k_\alpha^* \right\rangle_{\mathrm{c}} = 0 . \tag{7.24}$$

Small velocities are assumed which results in the identity of the partial time derivative and the material time derivative (cf. Eq. (3.2)). With the introduction of the accumulated dislocation velocity

$$\nu_{\mathrm{ac}} = 8\frac{\dot{\breve{\gamma}}_{\mathrm{ac}}}{\bar{\rho}_{\mathrm{ac}} b} , \tag{7.25}$$

the semi-phenomenological dislocation transport equation is obtained

$$\dot{\bar{\rho}}_{\mathrm{ac}} = \mathrm{Div}\left(\nu_{\mathrm{ac}}\frac{1}{b}\mathrm{Grad}\left(\breve{\gamma}_{\mathrm{ac}}\right)\right) . \tag{7.26}$$

7.3.3 Principle of virtual power

Two adjustments are made in comparison to Eq. (6.2). The vector valued micromorphic stresses $\boldsymbol{\xi}_\alpha$ is introduced conjugate to the rate of the in-plane micromorphic accumulated plastic slip gradient $\mathrm{grad}^{\mathrm{p}}\left(\dot{\breve{\gamma}}_{\mathrm{ac}}\right)$. In addition, the micromorphic accumulated plastic slip rate is assumed be

continuous at GBs. Consequently, the power balance is is postulated by

$$\int_{\mathcal{V}} \left(\pi - \sum_{\alpha=1}^{N} \operatorname{div}\left(\boldsymbol{P}_\alpha \boldsymbol{\xi}_\alpha\right) \right) \delta\dot{\breve{\gamma}}_{\mathrm{ac}} \,\mathrm{d}v - \int_{\mathcal{V}} \left(\varrho \boldsymbol{b} + \operatorname{div}\left(\boldsymbol{\sigma}\right)\right) \cdot \delta\dot{\boldsymbol{u}} \,\mathrm{d}v \\ - \int_{\mathcal{S}} \left(\Pi - \Big\{ \sum_{\alpha=1}^{N} \boldsymbol{P}_\alpha \boldsymbol{\xi}_\alpha \Big\} \cdot \boldsymbol{n}_{\mathcal{S}} \right) \delta\dot{\breve{\gamma}}_{\mathrm{ac}} \,\mathrm{d}a \\ + \int_{\partial\mathcal{V}_\Xi} \left(\sum_{\alpha=1}^{N} \boldsymbol{P}_\alpha \boldsymbol{\xi}_\alpha \cdot \boldsymbol{n} - \bar{\Xi} \right) \delta\dot{\breve{\gamma}}_{\mathrm{ac}} \,\mathrm{d}a + \int_{\partial\mathcal{V}_t} \left(\boldsymbol{\sigma}\boldsymbol{n} - \bar{\boldsymbol{t}}\right) \cdot \delta\dot{\boldsymbol{u}} \,\mathrm{d}a = 0 \,, \tag{7.27}$$

where the virtual solution fields $\{\delta\dot{\boldsymbol{u}}, \delta\dot{\breve{\gamma}}_{\mathrm{ac}}\}$ can be varied arbitrarily. The field equations, GB condition and Neumann conditions read

$$\operatorname{div}\left(\boldsymbol{\sigma}\right) = \boldsymbol{0} \,, \qquad \forall \boldsymbol{x} \in \mathcal{V} \,, \tag{7.28}$$

$$\pi - \sum_{\alpha=1}^{N} \operatorname{div}\left(\boldsymbol{P}_\alpha \boldsymbol{\xi}_\alpha\right) = 0 \,, \qquad \forall \boldsymbol{x} \in \mathcal{V} \,, \tag{7.29}$$

$$\Xi - \Big\{ \sum_{\alpha=1}^{N} \boldsymbol{P}_\alpha \boldsymbol{\xi}_\alpha \Big\} \cdot \boldsymbol{n}_{\mathcal{S}} = 0 \,, \qquad \forall \boldsymbol{x} \in \mathcal{S} \,, \tag{7.30}$$

$$\boldsymbol{\sigma}\boldsymbol{n} - \bar{\boldsymbol{t}} = \boldsymbol{0} \,, \qquad \forall \boldsymbol{x} \in \partial\mathcal{V}_t \,, \tag{7.31}$$

$$\sum_{\alpha=1}^{N} \boldsymbol{P}_\alpha \boldsymbol{\xi}_\alpha \cdot \boldsymbol{n} - \bar{\Xi} = 0 \,, \qquad \forall \boldsymbol{x} \in \partial\mathcal{V}_\Xi \,. \tag{7.32}$$

7.3.4 Helmholtz free energy

The mass specific Helmholtz free energy of the bulk material ψ is split into three contributions:

$$\psi = \psi_{\mathrm{e}}(\boldsymbol{F}_{\mathrm{e}}) + \sum_{\alpha=1}^{N} \psi_{\mathrm{h}}(\bar{\rho}_{\mathrm{ac}}, \mathrm{Grad}^{\mathrm{p}}\left(\breve{\gamma}_{\mathrm{ac}\alpha}\right)) + \psi_\chi(\breve{\gamma}_{\mathrm{ac}}, \gamma_{\mathrm{ac}}), \tag{7.33}$$

i.e., the classic, elastic energy ψ_{e}, the hardening energy ψ_{h} and the penalty energy ψ_{χ}, which is of numerical nature.

Following Section 6.2.3, a Hooke-type elastic contribution is considered

$$\varrho_0 \psi_{\mathrm{e}} = \frac{1}{2} \boldsymbol{E}_{\mathrm{e}} \cdot \tilde{\mathbb{C}}[\boldsymbol{E}_{\mathrm{e}}] \,. \tag{7.34}$$

Zaiser (2015) identifies three contributions to the energy of a dislocation system. A non-local contribution based on the density of GND ψ_{g}, a self-energy contribution ψ_{s} and a correlation contribution ψ_{c}. With these contributions the hardening energy is given as

$$\psi_{\mathrm{h}} = \psi_{\mathrm{g}} + \psi_{\mathrm{s}} + \psi_{\mathrm{c}} \,. \tag{7.35}$$

In the work of Hochrainer (2016) small densities of GND are assumed. Consequently, the non-local contribution based on the density of GND is neglected, however, this term is bound to stay, cf. Zaiser (2015).

For complex dislocation structures explicit expressions of the line tension of a dislocation, the self-energy per unit length, as constructed in Hirth et al. (1966), are not applicable. For such cases Hirth and Lothe (1982) give an approximation for the line tension of a dislocation by $T \sim \mu b^2$. Based on this relation the non-local energy is introduced in Ohno et al. (2008) based on the density of GND. A gradient theory for single-crystal plasticity using this approach is derived from the principle of virtual power by Gurtin et al. (2010); Gurtin and Ohno (2011). For monotonic loading processes this approach is consistent with the work of Ortiz and Repetto (1999); Hurtado and Ortiz (2013), where the non-local energy is formulated based on the absolute values of in-plane gradients of plastic slips in a linear form. In this work a non-local energy contribution is introduced in a quadratic form

$$\varrho_0 \psi_{\mathrm{g}} = \mu b^2 \left(\frac{K_{\mathrm{g}}}{2} \sum_{\alpha=1}^{N} \| \mathrm{Grad}^{\mathrm{p}} \left(\breve{\gamma}_{\mathrm{ac}} \right) \|^2 \right) \,, \tag{7.36}$$

with the energy parameter K_{g}. This form is based on the previous gradient plasticity theories dependent on the accumulated plastic slip, e.g., Erdle and Böhlke (2017); Wulfinghoff et al. (2013); Bayerschen et al. (2015). Note that despite the formulation of Eq. (7.36) based on the accumulated micromorphic plastic slip, the non-local energy contribution is introduced by means of in-plane slip gradients in order to account for the in-plane glide of dislocations on slip systems. The energy contribution is proposed using the Lagrangian gradient. For a discussion regarding alternative formulations using the Eulerian gradient and the gradient with respect to the intermediate configuration it is referred to Ling et al. (2018).

Based on the work of Groma et al. (2007), where the dislocation energy is obtained by a statistical theory of dislocations, and motivated by Zaiser (2015); Hochrainer (2016), the self-energy

$$\varrho_0 \psi_{\mathrm{s}} = \mu b^2 \left(-K_{\mathrm{s}} \bar{\rho}_{\mathrm{ac}} \ln \left(\frac{\bar{\rho}_{\mathrm{ac}}}{\rho_0} \right) \right) , \tag{7.37}$$

and the correlation energy

$$\varrho_0 \psi_{\mathrm{c}} = \mu b^2 \left(\frac{K_{\mathrm{c}}}{2 \bar{\rho}_{\mathrm{ac}} b^2} \sum_{\alpha=1}^{N} \| \mathrm{Grad}^{\mathrm{p}} \left(\breve{\gamma}_{\mathrm{ac}} \right) \|^2 \right) , \tag{7.38}$$

with the constants of order one K_{s} and K_{c} are introduced. As discussed by Hochrainer (2016) the reference dislocation density ρ_0 is not a scaling parameter, but a well defined physical quantity, namely, the saturation value for the density of admissible dislocations. A comparison of the energy contribution to the dislocation energy derived by Wilkens (1969) results in $\rho_0 = b^{-2}$.

Finally, following Section 6.2.3, a numerical penalty contribution based on Forest (2009) is introduced in the form

$$\varrho_0 \psi_\chi = \frac{1}{2} H_\chi (\breve{\gamma}_{\mathrm{ac}} - \gamma_{\mathrm{ac}})^2 \,, \tag{7.39}$$

with the penalty modulus H_χ. By use of a large penalty modulus, the coupling of the accumulated plastic slip to its micromorphic counterpart is ensured.

For resistance of GBs to plastic flow the GB energy approach of Wulfinghoff et al. (2013) is used. Hereby, the assumption of a continuous accumulated plastic slip field across the GBs is made. The GB energy is assumed to depend on the micromorphic accumulated plastic slip a linear form

$$\varrho_{\mathcal{S}0} \psi_{\mathcal{S}} = K_{\mathrm{m}} \breve{\gamma}_{\mathrm{ac}} \,, \tag{7.40}$$

with a GB energy parameter K_{m}. Microhard and microfree GBs are represented by the two limit cases $K_{\mathrm{m}} \to \infty$ and $K_{\mathrm{m}} = 0$ respectively. As a consequence of the linear dependency of the GB energy, a hardening of the GBs is neglected once GB slip is activated.

7.3.5 Clausius-Duhem inequality and flow rules

The Clausis-Duhem inequality is constructed in a similar manner to Section 6.2.4 with the internal energy contribution with respect to the reference placement

$$\begin{aligned} \mathcal{P}_{\mathrm{int}0} = \int_{\mathcal{V}_0} \left(\boldsymbol{S} \cdot \dot{\boldsymbol{E}} + \pi_0 \dot{\breve{\gamma}}_{\mathrm{ac}} + \sum_{\alpha=1}^{N} \boldsymbol{\xi}_{\alpha 0} \cdot \mathrm{Grad}^{\mathrm{p}} \left(\dot{\breve{\gamma}}_{\mathrm{ac}} \right) \right) \mathrm{d}V \\ + \int_{\mathcal{S}_0} \Pi_0 \dot{\breve{\gamma}}_{\mathrm{ac}} \, \mathrm{d}A \,. \end{aligned} \tag{7.41}$$

Bulk material

With Eqs. (7.34)–(7.39) the derivation of the Helmholtz free energy of the bulk material is given by

$$\begin{aligned}\dot{\psi} = \frac{\partial \psi_{\mathrm{e}}}{\partial \boldsymbol{E}} \cdot \dot{\boldsymbol{E}} + \frac{\partial \psi_{\mathrm{e}}}{\partial \boldsymbol{F}_{\mathrm{p}}} \cdot \dot{\boldsymbol{F}}_{\mathrm{p}} + \frac{\partial \psi_{\mathrm{h}}}{\partial \bar{\rho}_{\mathrm{ac}}} \dot{\bar{\rho}}_{\mathrm{ac}} + \frac{\partial \psi_{\chi}}{\partial \gamma_{\mathrm{ac}}} \dot{\gamma}_{\mathrm{ac}} \\ + \frac{\partial \psi_{\chi}}{\partial \breve{\gamma}_{\mathrm{ac}}} \dot{\breve{\gamma}}_{\mathrm{ac}} + \frac{\partial \psi_{\mathrm{g}}}{\partial \mathrm{Grad}^{\mathrm{p}}\left(\breve{\gamma}_{\mathrm{ac}}\right)} \cdot \mathrm{Grad}^{\mathrm{p}}\left(\dot{\breve{\gamma}}_{\mathrm{ac}}\right) \,.\end{aligned} \tag{7.42}$$

Inserting into the Clausius Duhem inequality of the bulk material, given in Eq. (6.18), results in

$$\begin{aligned}\mathcal{D} = \left(\boldsymbol{S} - \frac{\partial \varrho_0 \psi_{\mathrm{e}}}{\partial \boldsymbol{E}}\right) \cdot \dot{\boldsymbol{E}} + \left(\pi_0 - \frac{\partial \varrho_0 \psi_{\chi}}{\partial \breve{\gamma}_{\mathrm{ac}}}\right) \dot{\breve{\gamma}}_{\mathrm{ac}} \\ + \sum_{\alpha=1}^{N} \left(\boldsymbol{\xi}_{\alpha 0} - \frac{\partial \varrho_0 \psi_{\mathrm{h}}}{\partial \mathrm{Grad}^{\mathrm{p}}\left(\breve{\gamma}_{\mathrm{ac}}\right)}\right) \cdot \mathrm{Grad}^{\mathrm{p}}\left(\dot{\breve{\gamma}}_{\mathrm{ac}}\right) \\ - \frac{\partial \varrho_0 \psi_{\mathrm{e}}}{\partial \boldsymbol{F}_{\mathrm{p}}} \cdot \dot{\boldsymbol{F}}_{\mathrm{p}} - \frac{\partial \varrho_0 \psi_{\mathrm{h}}}{\partial \bar{\rho}_{\mathrm{ac}}} \mathrm{Div}\left(\nu_{\mathrm{ac}} \frac{1}{b} \mathrm{Grad}\left(\breve{\gamma}_{\mathrm{ac}}\right)\right) - \frac{\partial \varrho_0 \psi_{\chi}}{\partial \gamma_{\mathrm{ac}}} \dot{\gamma}_{\mathrm{ac}} \geq 0 \,,\end{aligned} \tag{7.43}$$

where the dislocation transport equation, given in Eq. (7.26), is used. The divergence theorem is applied to the last part of the volume integral, resulting in

$$\begin{aligned}\mathcal{D} = \left(\boldsymbol{S} - \frac{\partial \varrho_0 \psi_{\mathrm{e}}}{\partial \boldsymbol{E}}\right) \cdot \dot{\boldsymbol{E}} + \sum_{\alpha=1}^{N} \left(\boldsymbol{\xi}_{\alpha 0} - \frac{\partial \varrho_0 \psi_{\mathrm{h}}}{\partial \mathrm{Grad}^{\mathrm{p}}\left(\breve{\gamma}_{\mathrm{ac}}\right)}\right) \cdot \mathrm{Grad}^{\mathrm{p}}\left(\dot{\breve{\gamma}}_{\mathrm{ac}}\right) \\ + \left(\pi_0 + \frac{8}{\bar{\rho}_{\mathrm{ac}} b^2} \mathrm{Grad}\left(\frac{\partial \varrho_0 \psi_{\mathrm{h}}}{\partial \bar{\rho}_{\mathrm{ac}}}\right) \cdot \mathrm{Grad}\left(\breve{\gamma}_{\mathrm{ac}}\right) - \frac{\partial \varrho_0 \psi_{\chi}}{\partial \breve{\gamma}_{\mathrm{ac}}}\right) \dot{\breve{\gamma}}_{\mathrm{ac}} \\ - \frac{\partial \varrho_0 \psi_{\mathrm{e}}}{\partial \boldsymbol{F}_{\mathrm{p}}} \cdot \dot{\boldsymbol{F}}_{\mathrm{p}} - \frac{\partial \varrho_0 \psi_{\chi}}{\partial \gamma_{\mathrm{ac}}} \dot{\gamma}_{\mathrm{ac}} \geq 0 \,.\end{aligned} \tag{7.44}$$

Additionally, the following Neumann condition is obtained

$$\frac{\partial \varrho_0 \psi_\mathrm{h}}{\partial \bar{\rho}_\mathrm{ac}} \nu_\mathrm{ac} \frac{1}{b} \mathrm{Grad}\left(\breve{\gamma}_\mathrm{ac}\right) \cdot \boldsymbol{n} = 0\,, \qquad \forall \boldsymbol{x} \in \partial V\,. \tag{7.45}$$

The assumption of purely energetic stresses $\boldsymbol{S}$, π_0 and $\boldsymbol{\xi}_{\alpha 0}$ results in the potential relations

$$\begin{aligned} \boldsymbol{S} &= \frac{\partial \varrho_0 \psi_\mathrm{e}}{\partial \boldsymbol{E}_\mathrm{e}} \frac{\partial \boldsymbol{E}_\mathrm{e}}{\partial \boldsymbol{E}} = \boldsymbol{F}_\mathrm{p}^{-1} \tilde{\mathbb{C}}[\boldsymbol{E}_\mathrm{e}] \boldsymbol{F}_\mathrm{p}^{-\mathsf{T}}\,, \\ \pi_0 &= -\frac{8}{\bar{\rho}_\mathrm{ac} b^2} \mathrm{Grad}\left(\frac{\partial \varrho_0 \psi_\mathrm{h}}{\partial \bar{\rho}_\mathrm{ac}}\right) \cdot \mathrm{Grad}\left(\breve{\gamma}_\mathrm{ac}\right) - \breve{p}\,, \\ \boldsymbol{\xi}_{\alpha 0} &= \frac{\partial \varrho_0 \psi_\mathrm{h}}{\partial \mathrm{Grad}^\mathrm{p}\left(\breve{\gamma}_\mathrm{ac}\right)} = \left(\frac{K_\mathrm{c}\mu}{\bar{\rho}_\mathrm{ac}} + K_\mathrm{g}\mu b^2\right) \mathrm{Grad}^\mathrm{p}\left(\breve{\gamma}_\mathrm{ac}\right)\,. \end{aligned} \tag{7.46}$$

Furthermore, the reduced dissipation inequality of the bulk material

$$\mathcal{D}_\mathrm{red} = \boldsymbol{M}_\mathrm{e} \cdot \boldsymbol{L}_\mathrm{p} - \breve{p}\, \dot{\gamma}_\mathrm{ac} \geq 0 \tag{7.47}$$

is obtained. The herewith motivated bulk material flow rule

$$\dot{\lambda}_\alpha = \dot{\lambda}_0 \left\{ \frac{\tau_\alpha - \breve{p} - \tau_0}{\tau_\mathrm{D}} \right\}^p \tag{7.48}$$

strongly resembles Eq. (6.29). Due to the missing energy contribution dependent on the accumulated plastic slip, however, no hardening contribution of β is included.

Grain boundaries

With Eq. (7.40) and the divergence theorem which resulted in Eq. (7.45) the GB dissipation per unit area is obtained

$$\mathcal{D}_\mathcal{S} = \left(\Xi_0 + \left[\frac{\partial \varrho_0 \psi_\mathrm{h}}{\partial \bar{\rho}_\mathrm{ac}} \frac{8}{\bar{\rho}_\mathrm{ac} b^2} \mathrm{Grad}\left(\breve{\gamma}_\mathrm{ac}\right) \right] \cdot \boldsymbol{n}_\mathcal{S} - \frac{\partial \varrho_{\mathcal{S}0} \psi_\mathcal{S}}{\partial \breve{\gamma}_\mathrm{ac}} \right) \dot{\breve{\gamma}}_\mathrm{ac} \geq 0\,. \tag{7.49}$$

The following notation is introduced for the derivative of the hardening energy density by coarse-grained densities of dislocations

$$\beta_\rho \coloneqq \frac{\partial \varrho_0 \psi_\mathrm{h}}{\partial \bar{\rho}_\mathrm{ac}} \,. \tag{7.50}$$

In this work, dissipative effects are neglected and the GB condition, given in Eq. (7.30), has to be fulfilled. The rate independent GB yield criterion is specified by

$$\varphi \coloneqq \Big[\sum_{\alpha=1}^{N} \left(\frac{K_\mathrm{c}\mu}{\bar{\rho}_\mathrm{ac}} + K_\mathrm{g}\mu b^2 + \frac{8}{\bar{\rho}_\mathrm{ac} b^2}\beta_\rho \right) \mathrm{Grad}^\mathrm{p}\left(\breve{\gamma}_\mathrm{ac}\right) \Big] \cdot \boldsymbol{n}_\mathcal{S} - K_\mathrm{m} \tag{7.51}$$

The loading conditions read in the Kuhn-Tucker form

$$\varphi \dot{\breve{\gamma}}_\mathrm{ac} = 0 \,, \qquad \varphi \leq 0 \,, \qquad \dot{\breve{\gamma}}_\mathrm{ac} \geq 0 \,. \tag{7.52}$$

7.4 Finite element implementation

The enrichment of shape functions, discretization of GBs as well as the local newton scheme is consistent with Section 6.3. On a global level, however, the equations for the bulk material to compute the field variables for any given time increment Δt differ.

- Balance of linear momentum with neclection of body forces

$$\int_\mathcal{V} \mathrm{div}\left(\boldsymbol{\sigma}\right) \, \mathrm{d}v = \boldsymbol{0} \tag{7.53}$$

- Auxiliary equation for β_ρ

$$\int_\mathcal{V} \left(\beta_\rho + K_\mathrm{s}\mu b^2 \left(\ln\left(\frac{\bar{\rho}_\mathrm{ac}}{\rho_0} \right) + 1 \right) + \frac{4K_\mathrm{c}\mu}{\bar{\rho}_\mathrm{ac}^2} \| \mathrm{grad}\left(\breve{\gamma}_\mathrm{ac}\right) \|^2 \right) \, \mathrm{d}v = 0 \tag{7.54}$$

- Field equation for micromorphic accumulated plastic slip

$$\int_{\mathcal{V}} H_{\chi}\left(\breve{\gamma}_{\mathrm{ac}}-\gamma_{\mathrm{ac}}\right)\,\mathrm{d}v=\int_{\mathcal{V}}\operatorname{div}\left(8\left(\frac{K_{\mathrm{c}}\mu}{\bar{\rho}_{\mathrm{ac}}}+K_{\mathrm{g}}\mu b^{2}\right)\operatorname{grad}\left(\breve{\gamma}_{\mathrm{ac}}\right)\right)\,\mathrm{d}v + \int_{\mathcal{V}}\frac{8}{\bar{\rho}_{\mathrm{ac}}b^{2}}\operatorname{grad}\left(\beta_{\rho}\right)\cdot\operatorname{grad}\left(\breve{\gamma}_{\mathrm{ac}}\right)\,\mathrm{d}v \tag{7.55}$$

- Field equation for dislocation transport

$$\int_{\mathcal{V}}\left(\bar{\rho}_{\mathrm{ac}}-\bar{\rho}_{\mathrm{ac}}^{n}\right)\,\mathrm{d}v=\int_{\mathcal{V}}\operatorname{div}\left(8\frac{\breve{\gamma}_{\mathrm{ac}}-\breve{\gamma}_{\mathrm{ac}}^{n}}{\bar{\rho}_{\mathrm{ac}}b^{2}}\operatorname{grad}\left(\breve{\gamma}_{\mathrm{ac}}\right)\right)\,\mathrm{d}v \tag{7.56}$$

In total the ABAQUS user-element has eight DOF: Three for the displacement field $\boldsymbol{u}$, one for the auxiliary quantity β_{ρ}, one for the micromorphic accumulated plastic slip $\breve{\gamma}_{\mathrm{ac}}$, one for the accumulated density of dislocations $\bar{\rho}_{\mathrm{ac}}$ and an additional grain indices-field in order to implement curved or polyhedral GBs. For details on the FE discretization and the computation of the local and the global Newton scheme it is referred to Section 6.3.

7.5 Simulation setup

For the FE simulations a FCC crystal with $N=12$ slip systems is used. The elastic material behavior is characterized by the three elastic constants $C_{1111}=108\mathrm{GPa}$, $C_{1122}=62\mathrm{GPa}$ and $C_{1212}=28.3\mathrm{GPa}$. As discussed in Wulfinghoff and Böhlke (2015), these elastic constants describe a nearly isotropic elastic material behavior with a shear modulus of $\mu=26.12\mathrm{GPa}$. Based on Wulfinghoff and Böhlke (2015) the bulk material flow rule is characterized with reference shear rate $\dot{\gamma}_0=10^{-3}\mathrm{s}^{-1}$, drag stress $\tau_{\mathrm{D}}=1\mathrm{MPa}$ and slip rate sensitivity $p=20$. For the initial critical resolved yield stress the Taylor approach $\tau_0=a_0\mu b\sqrt{\bar{\rho}_{\mathrm{ini}}}$ is used,

cf. Taylor (1934). Hereby, following the work of Wulfinghoff and Böhlke (2015), the initial dislocation density of each slip system is chosen as $\bar{\rho}_{\mathrm{ini}} = 300\mu\mathrm{m}^{-2}$ and the absolute value of the Burgers vector is set to $b = 0.234\mathrm{nm}$. With the dimensionless parameter $a_0 = 0.3$ the initial critical resolved yield stress results as $\tau_0 \approx 32\mathrm{MPa}$.

The hardening energy material constants are chosen as $K_{\mathrm{s}} = K_{\mathrm{c}} = 1$ and $K_{\mathrm{g}} = \left(\bar{\rho}_{\mathrm{ini}} b^2\right)^{-1}$. This choice results in a equal contribution of ψ_{g} and ψ_{s} for $\bar{\rho} = \bar{\rho}_{\mathrm{ini}}$. The GB flow rule is described by the GB energy parameter K_{m} which is chosen as $K_{\mathrm{m}} = 100\mathrm{Nm}^{-1}$. The remaining, numerical parameter, is chosen sufficiently large as $H_{\chi} = 10^8\mathrm{MPa}$.

Displacement controlled FE simulations are performed for a laminate microstructure, illustrated in Fig. 7.2 (top). By the use of periodic boundary conditions it is sufficient to investigate a representative bicrystal with dimension $1\mu\mathrm{m} \times 1.25\mathrm{nm} \times 1.25\mathrm{nm}$, as illustrated in Fig. 7.2 (bottom). The bicrystal is loaded along the z-axis up to an overall strain of 0.01. Both grains are oriented in a standard $\langle 100 \rangle$-orientation with respect to the x-axis of the Cartesian coordinate system.

7.6 Finite element results

In Fig. 7.3 (top), the stress-strain curve for the tensile test simulation is shown. The volume-averaged true stress σ_{zz} is plotted over the volume-averaged true strain $\ln(\boldsymbol{U}) = \ln\sqrt{\boldsymbol{F}^{\mathsf{T}}\boldsymbol{F}}$. Hereby, three domains are recognizable. Fig. 7.3 (left) shows the distributions of the accumulated plastic slip over the length of the periodic bicrystal for the three stress-strain states at times t_1, t_2 and t_3, labeled in Fig. 7.3 (top). The corresponding distributions of the accumulated density of dislocations are shown in Fig. 7.3 (right). Due to the periodicity of the bicrystal only one half of the length is shown, with the GB located at $x = 0.25\mu\mathrm{m}$.

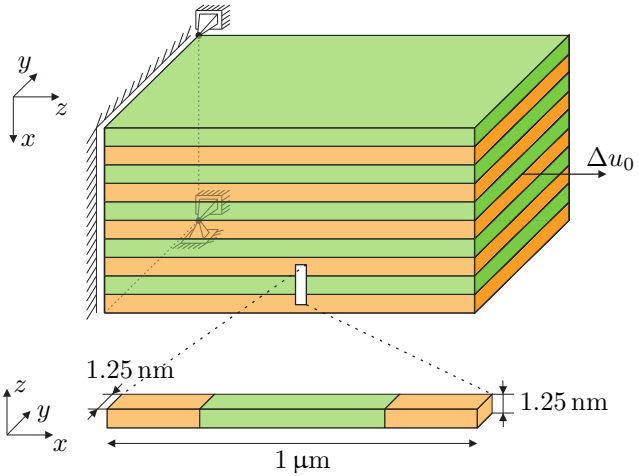

Figure 7.2: Illustration of boundary conditions of laminate microstructure (top) and representative bicrystal (bottom) with periodic boundary conditions.

At first the bulk material as well as the GBs deform elastically. Due to the absence of plastic slip in this domain the bulk material elastic-plastic transition point only depends on the initial critical shear stress τ_0. As soon as plastic deformation occurs inside the bulk material, dislocations arise inside the bulk material, transport of dislocations occurs and dislocation pile-up at the GBs. The GBs are still microhard in this domain, meaning, they act as insurmountable obstacles for plastic slip. The hardening of the bulk material is a combination of isotropic hardening of dislocations and dislocation pile-up at the GBs. After the critical GB state is reached, the GB flow rule is fulfilled and the loading condition is satisfied, dislocation transport across the GB is permitted and, consequently, a plastic deformation of the GB occurs. This activation point of the GB slip is mainly influenced by the self-energy parameter K_s. For small values of K_s, the resistance of the GB to the passing of dislocations is reduced. The corresponding distribution of the final micromorphic

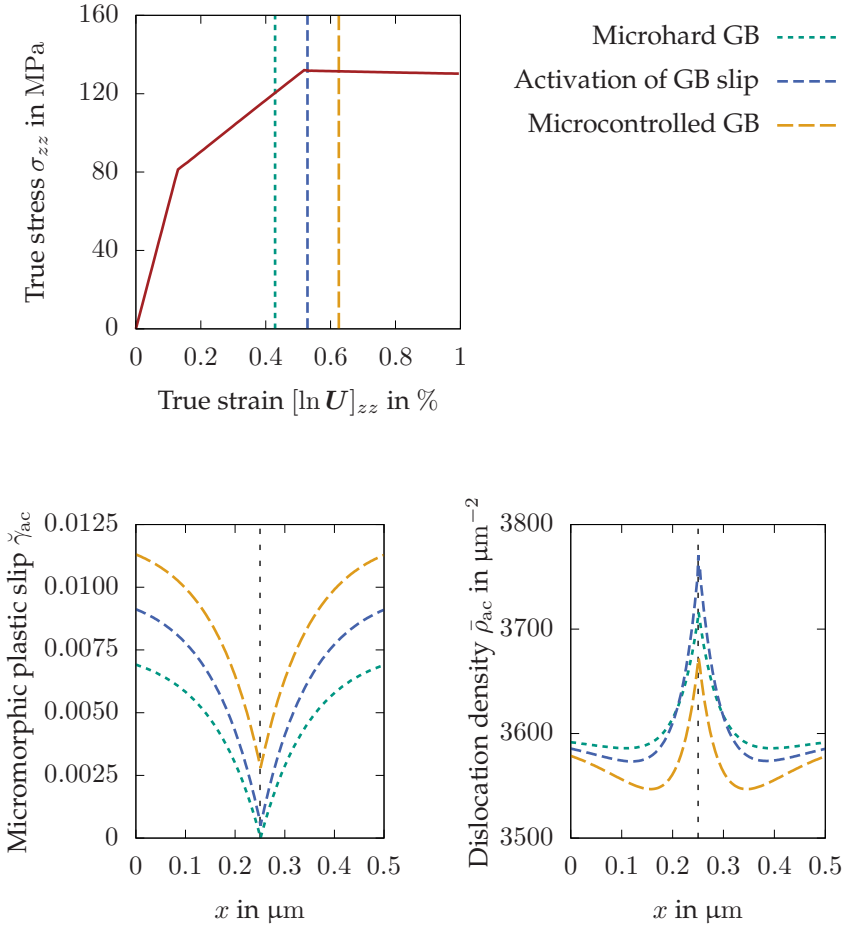

Figure 7.3: Mechanical response (volume-averaged) of tensile test simulation (top). The three vertical lines correspond to the three different GB states as indicated. Distribution of the micromorphic accumulated plastic slip $\breve{\gamma}_{\mathrm{ac}}$ (left) and distribution of the accumulated density of dislocations $\bar{\rho}_{\mathrm{ac}}$ (right) over the length of the periodic bicrystal. The GB is located at $x = 0.25\mu\mathrm{m}$

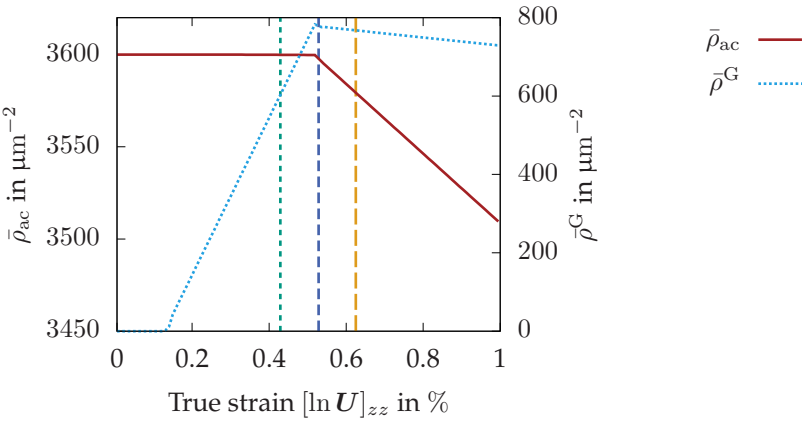

Figure 7.4: Evolution of the volume-averaged accumulated density of dislocations $\bar{\rho}_{\mathrm{ac}}$ and volume-averaged accumulated density of GND $\bar{\rho}^{\mathrm{G}} = \|\mathrm{Grad}^{\mathrm{p}}\,(\breve{\gamma}_{\mathrm{ac}})\,\|b^{-1}$. The three vertical lines correspond to a microhard GB, the activation of GB slip and a microcontrolled GB.

accumulated plastic slip is more homogeneous over the length of the grain structure. Due to the linear form of the GB energy, additional dislocations arising inside the bulk material are allowed to glide across GBs without additional hindrance. Consequently, no hardening of the GB occurs and the resulting force on the evolution of plastic slip is constant. The corresponding distribution of the micromorphic accumulated plastic slip is shifted to higher slip values for increasing strain, see Fig. 7.3 (left). Dislocations which are piled-up at the GBs annihilate as soon as GB slip is permitted, see Fig. 7.3 (right). This decrease of the average accumulated density of dislocations, shown in Fig. 7.4, results in a softening in the microcontrolled GB state, as shown in Fig. 7.3 (top). In contrary to phenomenological gradient plasticity frameworks the dislocation transport equation assures, without consideration of production terms, that the averaged dislocation density is constant in the microhard GB regime. As soon as GB slip is activated, piled-up dislocation

annihilate at the GB, which results in a decline of number of dislocations within the simulated grain structure. Additionally, the evolution of the volume-averaged accumulated density of GND $\bar{\rho}^{\mathrm{G}} = \|\mathrm{Grad}^{\mathrm{p}}\,(\breve{\gamma}_{\mathrm{ac}})\,\|b^{-1}$ is shown. The results show that the portion of GND densities on the total density of dislocations is small, however, can not be neglected.

Additionally to the tensile test simulation of the laminate microstructure a simple shear simulation is performed for a fiber-matrix composite material as shown in Fig. 7.5. Periodic boundary conditions are applied to a representative segment of the composite material, which is loaded along the x-axis up to an overall displacement of $\Delta u_0 = 10\mathrm{nm}$. The composite material consists of elastic fibers of diameter $650\mathrm{nm}$ embedded in an elasto-plastic matrix material in a periodic manner. For simplicity, the fibers are assumed to have the same elastic properties as the matrix material. In the matrix material dislocations pile-up at the GBs until the GB yield condition is fulfilled. Even after the activation of GB slip, however, the boundaries still act as insurmountable obstacles for plastic slip. Due to the elastic behavior of the fibers plastic slip occurs only in the matrix material. Consequently, the pile-up structure of the dislocations at the GBs, i.e., the amount of GND $\bar{\rho}^{\mathrm{G}} = \|\mathrm{Grad}\,(\breve{\gamma}_{\mathrm{ac}})\,\|b^{-1}$, enlarges in the matrix material. Inside the fibers the density of dislocations does not evolve and hence has a homogeneous value of $\bar{\rho}_{\mathrm{ini}}$. The small band inside the fibers with dislocation density values between $\bar{\rho}_{\mathrm{ini}}$ and the piled-up dislocation density of the matrix material side is of artificial nature due to an interpolation between the integration points. Due to the dislocation transport equation the total amount of dislocations is preserved inside the fiber-matrix composite. Consequently, due to the pile-up of dislocations at the fiber-matrix interfaces, the density of dislocations sinks in areas of homogeneous plastic slip inside the matrix material.

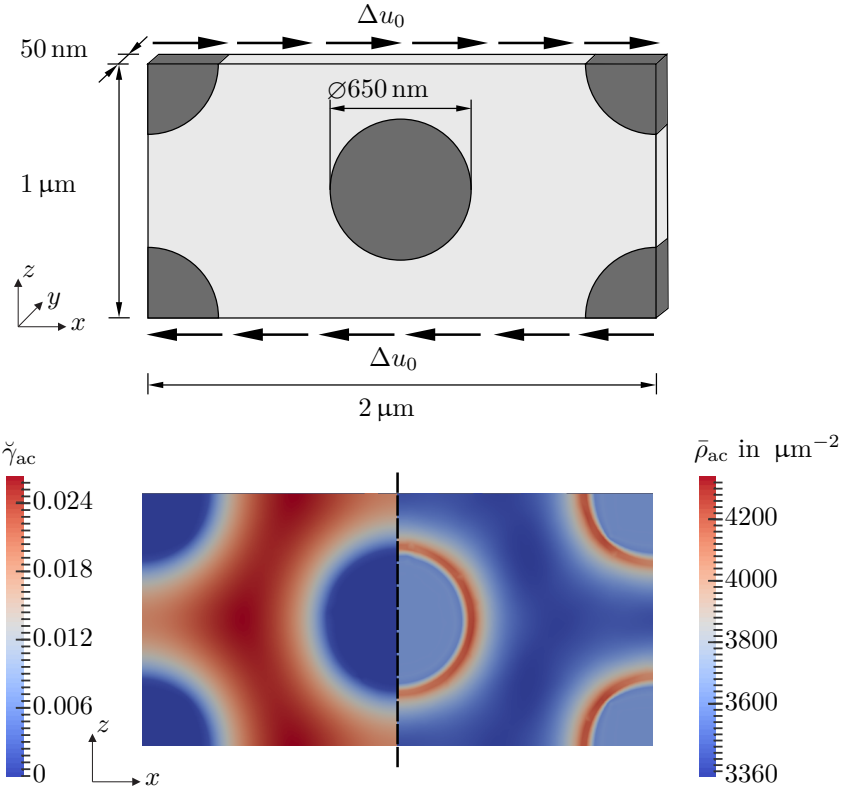

Figure 7.5: Illustration of the simple shear of a fiber-matrix composite material with periodic boundary conditions (top) and FE results shown in the xz-plane (bottom). The left-hand side shows the final micromorphic accumulated plastic slip $\breve{\gamma}_{\mathrm{ac}}$. The right-hand side shows the corresponding coarse-grained accumulated density of dislocations $\bar{\rho}_{\mathrm{ac}}$.

7.7 Summary and conclusion

An approach is presented which allows to model the transport of dislocations on a coarse-grained scale within a numerically efficient framework based on accumulated field variables. With the approach of Eq. (7.22) the in-plane gradient of the accumulated plastic slip is prorated on the individual slip systems which preserves the slip kinematics of in-plane dislocation gliding. Additionally to the accumulated plastic slip the coarse-grained accumulated density of dislocations is introduced. With an energetic GB the dislocation pile-up at GBs (microhard) and the dislocation annihilation after activation of GB slip (microcontrolled) is modeled. This is consistent to the experimental work of Sun et al. (1998), where the buildup of dislocations near the GB and a vanishing peak at higher strain levels is observed. The FE implementation is discussed as well as the distributions of the plastic slip and dislocation density over a periodic laminate structure and a fiber-matrix composite material. The presented approach provides a promising numerically efficient framework for further investigations, for example investigations on the curvature induced line length production, which is neglected in this work.

Regarding the continuity of plastic slip across GBs the following has to be considered: For the special case of equally oriented grains, as considered in this chapter, the accumulated plastic slip is continuous across GBs. As discussed in Chapter 5 for misoriented grains, however, a discontinuous solution field is required. One possible approach for misoriented grains is the enrichment of trial functions with a discontinuous enrichment function as presented in Chapter 6.

Chapter 8

Summary and outlook

This thesis addresses several open questions of dislocation-GB interactions within gradient crystal plasticity frameworks. The behavior polycrystalline microstructures under consideration of dislocation pile-ups at GBs was realized by a model approach based on an extended energy balance according to Prahs and Böhlke (2020a;b). An equivalence to the model approach based on an extended principle of virtual power according to Gurtin (2002) was obtained under the assumption of isothermal processes, a homogeneous distribution of the temperature and a temperature-independent Helmholtz free energy for the bulk material and the GBs. Under these assumptions, however, it was shown that both the bulk material as well as the GBs are dissipation free.

The gradient crystal plasticity framework was applied to a three-phase periodic laminate microstructure in order to investigate dislocation transmission through GBs. The analytical solution of a boundary value problem was investigated for the special case of single slip. A GB energy according to Gurtin (2008) based on the geometric dislocation tensor was used in order to account for a GB resistance based on the grain misorientation angle For the limit case of a vanishing grain misorientation the single crystal consistency check is failed with the commonly used GB flow condition approach based on the assumption of independent plastic slips. In order to account for this shortcoming a new model approach for the GB flow condition was presented in this work. An additional flow rule is introduced in which the discontinuity

of the plastic slip gradient at the GB is correlated to a grain misorientation function.

Applying the new approach to the limit case of a vanishing grain misorientation results in two different solutions. While one solution is an artificial, non-physical solution identical to the solution obtained by the common approach, the second solution showed a single-crystal response with a continuous and symmetric parabolic distribution of the plastic slip even under variation of the grain size. The effect of the grain size on the mechanical response was investigated. A good agreement is found with a simple inverse or logarithmic approach, which is suggested in Li et al. (2016) based on underlying dislocation theories.

With the introduced GB flow condition approach at first, a microhard state results in a pile-up of dislocations at the GB until a critical state is reached. The transition to a microcontrolled GB state where dislocation transmission across the GB occurs strongly depends on the misorientation angle between adjacent grains. The presented approach provides a promising framework the modeling of polycrystalline materials within a finite element implementation, where various misorientation angles and grain sizes are involved. For each slip system, however, one gradient-stress associated with the in-plane gradient of plastic slip has to be introduced. This results in a high computation cost, which is increased even more under consideration of the discontinuous distributions of the plastic slips which result from an orientation dependent dislocation transmission across GB.

The approach of Erdle and Böhlke (2017) was presented where one gradient-stress associated with the accumulated plastic slip is used as an overall measure of long range dislocation interactions within a finite strain setting. This provides a promising numerically efficient framework for large scale three-dimensional FE simulations. Discontinuous trial function were introduced in order to evaluate a GB flow rule in due consideration of a discontinuous distribution of the accumulated plastic

slip across GBs. The FE implementation of a periodic bicrystal was used to investigate the influence of energy parameters and size effects.

An extension to the accumulated plastic slip framework was presented which allows to model the transport of dislocations on a coarse-grained scale. The in-plane gradient of the accumulated plastic slip is prorated on the individual slip systems which preserves the slip kinematics of in-plane dislocation gliding. A dislocation transport equation based on the coarse-grained accumulated density of dislocations was introduced. With the presented framework the two stages of GB behavior which are observed in Sun et al. (1998), i.e., buildup of dislocations near the GB and a vanishing peak at higher strain levels, was modeled based on energetic GBs. The dislocation pile-up at GBs (microhard) and the dislocation annihilation after activation of GB slip (microcontrolled) was observed for laminate microstructures and fiber-matrix composites.

Even though multiple relevant results regarding dislocation-GB interactions have been obtained within this work, further investigations are necessary. In detail, these are:

- Investigation of dislocation behavior at GBs under cyclic loading
- Modeling of temperature dependent dislocation and GB effects
- Comparison of gradient crystal plasticity framework based on individual slip gradients with the framework based on the gradient of the accumulated plastic slip
- Modeling of an orientation-dependent GB flow rule in the accumulated plastic slip framework
- Investigation of curvature induced line length production in the dislocation transport equation
- Direct validation of dislocation-GB interactions with experimental investigations and discrete dislocation dynamics simulation

Appendix A

Appendix

A.1 Slip system convention of face-centered cubic unit cell

The slip system convention in reference configuration, which is used for the implementation of the FCC materials, is listed in Table A.1. The slip systems are labeled according to the Schmid-Boas slip system convention, cf. Schmid and Boas (1935).

Table A.1: Slip system convention for FCC in Schmid-Boas notation.

α	1	2	3	4	5	6
$\boldsymbol{n}_\alpha$	(111)	(111)	(111)	$(\bar{1}11)$	$(\bar{1}11)$	$(\bar{1}11)$
$\boldsymbol{d}_\alpha$	$[01\bar{1}]$	$[\bar{1}01]$	$[1\bar{1}0]$	$[01\bar{1}]$	$[101]$	$[\bar{1}\bar{1}0]$
α	7	8	9	10	11	12
$\boldsymbol{n}_\alpha$	$(\bar{1}1\bar{1})$	$(\bar{1}1\bar{1})$	$(\bar{1}1\bar{1})$	$(11\bar{1})$	$(11\bar{1})$	$(11\bar{1})$
$\boldsymbol{d}_\alpha$	$[011]$	$[10\bar{1}]$	$[\bar{1}\bar{1}0]$	$[011]$	$[1\bar{1}0]$	$[101]$

A.2 Details on the global algorithmic tangent

The total derivatives of Eqs. (6.47), (6.49) and (6.51) for the nodal DOF $\{\hat{\underline{u}}, \hat{\underline{\gamma}}, \hat{\underline{\delta}}\}$ read in matrix-vector notation

$$\begin{pmatrix} \mathrm{d}\underline{r}^u \\ \mathrm{d}r^\gamma \\ \mathrm{d}r^\delta \end{pmatrix} = \begin{pmatrix} \dfrac{\partial \underline{r}^u}{\partial \hat{\underline{u}}} & \dfrac{\partial \underline{r}^u}{\partial \hat{\underline{\gamma}}} & \dfrac{\partial \underline{r}^u}{\partial \hat{\underline{\delta}}} \\ \dfrac{\partial r^\gamma}{\partial \hat{\underline{\gamma}}} & \dfrac{\partial r^\gamma}{\partial \hat{\underline{\gamma}}} & \dfrac{\partial r^\gamma}{\partial \hat{\underline{\gamma}}} \\ \dfrac{\partial r^\delta}{\partial \hat{\underline{\delta}}} & \dfrac{\partial r^\delta}{\partial \hat{\underline{\delta}}} & \dfrac{\partial r^\delta}{\partial \hat{\underline{\delta}}} \end{pmatrix} \begin{pmatrix} \mathrm{d}\hat{\underline{u}} \\ \mathrm{d}\hat{\underline{\gamma}} \\ \mathrm{d}\hat{\underline{\delta}} \end{pmatrix} . \tag{A.1}$$

The entries of the global algorithmic tangent are computed by

$$\frac{\partial \underline{r}^u}{\partial \hat{\underline{u}}} = \int_{\mathcal{V}} \underline{\underline{B}}^{u\,\mathsf{T}} \frac{\partial \underline{\sigma}}{\partial \underline{E}} \underline{\underline{B}}^u \,\mathrm{d}v \,, \tag{A.2}$$

$$\frac{\partial \underline{r}^u}{\partial \hat{\underline{\gamma}}} = \int_{\mathcal{V}} \underline{\underline{B}}^{u\,\mathsf{T}} \frac{\partial \underline{\sigma}}{\partial \breve{\gamma}_{\mathrm{ac}}} \underline{N}^\gamma \,\mathrm{d}v \,, \tag{A.3}$$

$$\frac{\partial \underline{r}^u}{\partial \hat{\underline{\delta}}} = \int_{\mathcal{V}} \underline{\underline{B}}^{u\,\mathsf{T}} \frac{\partial \underline{\sigma}}{\partial \breve{\gamma}_{\mathrm{ac}}} \underline{N}^\delta \,\mathrm{d}v \,, \tag{A.4}$$

$$\frac{\partial r^\gamma}{\partial \hat{\underline{u}}} = \int_{\mathcal{V}} \underline{N}^{\gamma\,\mathsf{T}} \left(-\frac{\partial \breve{p}}{\partial \underline{E}} \right) \underline{\underline{B}}^u \,\mathrm{d}v \,, \tag{A.5}$$

$$\frac{\partial r^\gamma}{\partial \hat{\underline{\gamma}}} = \int_{\mathcal{V}} \underline{N}^{\gamma\,\mathsf{T}} \underline{N}^\gamma \left(\frac{\partial \beta}{\partial \breve{\gamma}_{\mathrm{ac}}} - \frac{\partial \breve{p}}{\partial \breve{\gamma}_{\mathrm{ac}}} \right) \mathrm{d}v + \int_{\mathcal{V}} \underline{B}^{\gamma\,\mathsf{T}} \underline{B}^\gamma K_{\mathrm{g}} \,\mathrm{d}v \,, \tag{A.6}$$

$$\frac{\partial r^\gamma}{\partial \hat{\underline{\delta}}} = \int_{\mathcal{V}} \underline{N}^{\gamma\,\mathsf{T}} \underline{N}^\delta \left(\frac{\partial \beta}{\partial \breve{\gamma}_{\mathrm{ac}}} - \frac{\partial \breve{p}}{\partial \breve{\gamma}_{\mathrm{ac}}} \right) \mathrm{d}v + \int_{\mathcal{V}} \underline{B}^{\gamma\,\mathsf{T}} \underline{B}^\delta K_{\mathrm{g}} \,\mathrm{d}v \,, \tag{A.7}$$

$$\frac{\partial r^\delta}{\partial \hat{\underline{u}}} = \int_{\mathcal{V}} \underline{N}^{\delta\,\mathsf{T}} \left(-\frac{\partial \breve{p}}{\partial \underline{E}} \right) \underline{\underline{B}}^u \,\mathrm{d}v \,, \tag{A.8}$$

$$\frac{\partial r^\delta}{\partial \hat{\underline{\gamma}}} = \int_{\mathcal{V}} \underline{N}^{\delta\,\mathsf{T}} \underline{N}^\gamma \left(\frac{\partial \beta}{\partial \breve{\gamma}_{\mathrm{ac}}} - \frac{\partial \breve{p}}{\partial \breve{\gamma}_{\mathrm{ac}}} \right) \mathrm{d}v + \int_{\mathcal{V}} \underline{B}^{\delta\,\mathsf{T}} \underline{B}^\gamma K_{\mathrm{g}} \,\mathrm{d}v \,, \tag{A.9}$$

$$\frac{\partial r^\delta}{\partial \hat{\underline{\delta}}} = \int_{\mathcal{V}} \underline{N}^{\delta\,\mathsf{T}} \underline{N}^\delta \left(\frac{\partial \beta}{\partial \breve{\gamma}_{\mathrm{ac}}} - \frac{\partial \breve{p}}{\partial \breve{\gamma}_{\mathrm{ac}}} \right) \mathrm{d}v + \int_{\mathcal{V}} \underline{B}^{\delta\,\mathsf{T}} \underline{B}^\delta K_{\mathrm{g}} \,\mathrm{d}v \,. \tag{A.10}$$

Bibliography

Aifantis, E. C., 1987. The physics of plastic deformation. International Journal of Plasticity 3 (3), 211–247.

Alipour, A., Reese, S., Svendsen, B., Wulfinghoff, S., 2020. A grain boundary model considering the grain misorientation within a geometrically nonlinear gradient-extended crystal viscoplasticity theory. Proceedings of the Royal Society A: Mathematical, Physical and Engineering Sciences 476 (2235), 20190581.

Ambrosio, L., Soner, H. M., 1996. Level set approach to mean curvature flow in arbitrary codimension. Journal of Differential Geometry 43 (4), 693–737.

Anand, L., Gurtin, M. E., Reddy, B. D., 2015. The stored energy of cold work, thermal annealing, and other thermodynamic issues in single crystal plasticity at small length scales. International Journal of Plasticity 64, 1–25.

Armstrong, R., Codd, I., Douthwaite, R. M., Petch, N. J., 1962. The plastic deformation of polycrystalline aggregates. The Philosophical Magazine: A Journal of Theoretical Experimental and Applied Physics 7 (73), 45–58.

Arzt, E., 1998. Size effects in materials due to microstructural and dimensional constraints: A comparative review. Acta Materialia 46 (16), 5611–5626.

Ashby, M. F., 1970. The deformation of plastically non-homogeneous materials. Philosophical Magazine 21 (170), 399–424.

Aslan, O., Cordero, N. M., Gaubert, A., Forest, S., 2011. Micromorphic approach to single crystal plasticity and damage. International Journal of Engineering Science 49 (12), 1311–1325.

Barenblatt, G. I., 1959. The formation of equilibrium cracks during brittle fracture. General ideas and hypotheses. Axially-symmetric cracks. Journal of Applied Mathematics and Mechanics 23 (3), 622–636.

Bayerschen, E., 2016. Single-crystal Gradient Plasticity With an Accumulated Plastic Slip: Theory and Applications. Doctoral thesis, KIT Scientific Publishing, Karlsruhe.

Bayerschen, E., Böhlke, T., 2016. Power-law defect energy in a single-crystal gradient plasticity framework: A computational study. Computational Mechanics 58 (1), 13–27.

Bayerschen, E., McBride, A. T., Reddy, B. D., Böhlke, T., 2016. Review on slip transmission criteria in experiments and crystal plasticity models. Journal of Materials Science 51 (5), 2243–2258.

Bayerschen, E., Stricker, M., Wulfinghoff, S., Weygand, D., Böhlke, T., 2015. Equivalent plastic strain gradient plasticity with grain boundary hardening and comparison to discrete dislocation dynamics. Proceedings of the Royal Society A: Mathematical, Physical and Engineering Sciences 471 (2184), 20150388.

Belytschko, T., Moës, N., Usui, S., Parimi, C., 2001. Arbitrary discontinuities in finite elements. International Journal for Numerical Methods in Engineering 50 (4), 993–1013.

Bergman, T. L., Lavine, A. S., Incropera, F. P., DeWitt, D. P., 2017. Fundamentals of Heat and Mass Transfer, 8th Edition. Wiley, New York.

Bertram, A., 2008. Elasticity and Plasticity of Large Deformations: An Introduction, 2nd Edition. Springer, Berlin Heidelberg.

Bishop, J. F. W., Hill, R., 1951. A theory of the plastic distortion of a polycrystalline aggregate under combined stresses. The London, Edinburgh, and Dublin Philosophical Magazine and Journal of Science 42 (327), 414–427.

Britton, T. B., Randman, D., Wilkinson, A. J., 2009. Nanoindentation study of slip transfer phenomenon at grain boundaries. Journal of Materials Research 24 (3), 607–615.

Cermelli, P., Fried, E., Gurtin, M. E., 2005. Transport relations for surface integrals arising in the formulation of balance laws for evolving fluid interfaces. Journal of Fluid Mechanics 544, 339–351.

Cermelli, P., Gurtin, M. E., 2001. On the characterization of geometrically necessary dislocations in finite plasticity. Journal of The Mechanics and Physics of Solids 49, 1539–1568.

Cermelli, P., Gurtin, M. E., 2002. Geometrically necessary dislocations in viscoplastic single crystals and bicrystals undergoing small deformations. International Journal of Solids and Structures 39 (26), 6281–6309.

Coleman, B. D., Noll, W., 1963. The thermodynamics of elastic materials with heat conduction and viscosity. Archive for Rational Mechanics and Analysis 13 (1), 167–178.

Conrad, H., Feuerstein, S., Rice, L., 1967. Effects of grain size on the dislocation density and flow stress of niobium. Materials Science and Engineering 2 (3), 157–168.

Cordero, N. M., Gaubert, A., Forest, S., Busso, E. P., Gallerneau, F., Kruch, S., 2010. Size effects in generalised continuum crystal plasticity for two-phase laminates. Journal of the Mechanics and Physics of Solids 58 (11), 1963–1994.

El-Azab, A., 2000. Statistical mechanics treatment of the evolution of dislocation distributions in single crystals. Physical Review B 61 (18), 11956–11966.

Erdle, H., Böhlke, T., 2017. A gradient crystal plasticity theory for large deformations with a discontinuous accumulated plastic slip. Computational Mechanics 60 (6), 923–942.

Eringen, A., Suhubi, E., 1964. Nonlinear theory of simple micro-elastic solids - I. International Journal of Engineering Science 2, 189–203.

Estrin, Y., Tóth, L. S., Molinari, A., Bréchet, Y., 1998. A dislocation-based model for all hardening stages in large strain deformation. Acta Materialia 46 (15), 5509–5522.

Fleck, N. A., Muller, G. M., Ashby, M. F., Hutchinson, J. W., 1994. Strain gradient plasticity: Theory and experiment. Acta Metallurgica et Materialia 42 (2), 475–487.

Forest, S., 2008. Some links between Cosserat, strain gradient crystal plasticity and the statistical theory of dislocations. Philosophical Magazine 88 (30-32), 3549–3563.

Forest, S., 2009. Micromorphic approach for gradient elasticity, viscoplasticity, and damage. Journal of Engineering Mechanics 135 (3), 117–131.

Forest, S., Ammar, K., Appolaire, B., 2011. Micromorphic vs. phase-field approaches for gradient viscoplasticity and phase transformations. In: Markert, B. (Ed.), Advances in Extended and Multifield Theories for Continua. Springer, Berlin Heidelberg.

Forest, S., Guéninchault, N., 2013. Inspection of free energy functions in gradient crystal plasticity. Acta Mechanica Sinica 29 (6), 763–772.

Forest, S., Sedláček, R., 2003. Plastic slip distribution in two-phase laminate microstructures: Dislocation-based versus generalized-continuum approaches. Philosophical Magazine 83 (2), 245–276.

Fries, T.-P., Belytschko, T., 2010. The extended/generalized finite element method: An overview of the method and its applications. International Journal for Numerical Methods in Engineering 84 (3), 253–304.

Gottschalk, D., McBride, A., Reddy, B. D., Javili, A., Wriggers, P., Hirschberger, C. B., 2016. Computational and theoretical aspects of a grain-boundary model that accounts for grain misorientation and grain-boundary orientation. Computational Materials Science 111, 443–459.

Groma, I., Györgyi, G., Kocsis, B., 2007. Dynamics of coarse grained dislocation densities from an effective free energy. Philosophical Magazine 87 (8-9), 1185–1199.

Gurtin, M. E., 2002. A gradient theory of single-crystal viscoplasticity that accounts for geometrically necessary dislocations. Journal of the Mechanics and Physics of Solids 50 (1), 5–32.

Gurtin, M. E., 2008. A theory of grain boundaries that accounts automatically for grain misorientation and grain-boundary orientation. Journal of the Mechanics and Physics of Solids 56 (2), 640–662.

Gurtin, M. E., Anand, L., 2008. Nanocrystalline grain boundaries that slip and separate: A gradient theory that accounts for grain-boundary stress and conditions at a triple-junction. Journal of the Mechanics and Physics of Solids 56 (1), 184–199.

Gurtin, M. E., Fried, E., Anand, L., 2010. The Mechanics and Thermodynamics of Continua. Cambridge University Press, Cambridge.

Gurtin, M. E., Needleman, A., 2005. Boundary conditions in small-deformation, single-crystal plasticity that account for the Burgers vector. Journal of the Mechanics and Physics of Solids 53 (1), 1–31.

Gurtin, M. E., Ohno, N., 2011. A gradient theory of small-deformation, single-crystal plasticity that accounts for GND-induced interactions between slip systems. Journal of the Mechanics and Physics of Solids 59 (2), 320–343.

Hall, E. O., 1951. The deformation and ageing of mild steel: III Discussion of results. Proceedings of the Physical Society B 64 (9), 747–753.

Hamid, M., Lyu, H., Schuessler, B. J., Wo, P. C., Zbib, H. M., 2017. Modeling and characterization of grain boundaries and slip transmission in dislocation density-based crystal plasticity. Crystals 7 (6), 152.

Haouala, S., Alizadeh, R., Bieler, T. R., Segurado, J., LLorca, J., 2020. Effect of slip transmission at grain boundaries in Al bicrystals. International Journal of Plasticity 126, 102600.

Hill, R., 1966. Generalized constitutive relations for incremental deformation of metal crystals by multislip. Journal of the Mechanics and Physics of Solids 14 (2), 95–102.

Hirth, J. P., Jøssang, T., Lothe, J., 1966. Dislocation energies and the concept of line tension. Journal of Applied Physics 37 (1), 110–116.

Hirth, J. P., Lothe, J., 1982. Theory of Dislocations. Krieger Publishing Company, Malabar.

Hochrainer, T., 2013. Higher order alignment tensors for continuum dislocation dynamics. In: MRS Online Proceedings Library. Vol. 1535. Cambridge University Press, Cambridge.

Hochrainer, T., 2016. Thermodynamically consistent continuum dislocation dynamics. Journal of the Mechanics and Physics of Solids 88, 12–22.

Hochrainer, T., Sandfeld, S., Zaiser, M., Gumbsch, P., 2014. Continuum dislocation dynamics: Towards a physical theory of crystal plasticity. Journal of the Mechanics and Physics of Solids 63, 167–178.

Hochrainer, T., Zaiser, M., Gumbsch, P., 2007. A three-dimensional continuum theory of dislocation systems: Kinematics and mean-field formulation. Philosophical Magazine 87 (8-9), 1261–1282.

Hull, D., Bacon, D. J., 2011. Introduction to Dislocations, 5th Edition. Butterworth-Heinemann, Amsterdam.

Hurtado, D. E., Ortiz, M., 2013. Finite element analysis of geometrically necessary dislocations in crystal plasticity. International Journal for Numerical Methods in Engineering 93 (1), 66–79.

Kacher, J., Robertson, I. M., 2014. In situ and tomographic analysis of dislocation/grain boundary interactions in α-titanium. Philosophical Magazine 94 (8), 814–829.

Kalidindi, S. R., Vachhani, S. J., 2014. Mechanical characterization of grain boundaries using nanoindentation. Current Opinion in Solid State and Materials Science 18 (4), 196–204.

Kocks, F., Mecking, H., 2003. Physics and phenomenology of strain hardening: The FCC case. Progress in Materials Science 48, 171–273.

Kondo, S., Mitsuma, T., Shibata, N., Ikuhara, Y., 2016. Direct observation of individual dislocation interaction processes with grain boundaries. Science Advances 2 (11), e1501926.

Lagow, B., Robertson, I. M., Jouiad, M., Lassila, D., Lee, T. C., Birnbaum, H., 2001. Observation of dislocation dynamics in the electron microscope. Materials Science and Engineering A-structural Materials Properties Microstructure and Processing 309, 445–450.

Lee, T. C., Robertson, I. M., Birnbaum, H. K., 1990. TEM in situ deformation study of the interaction of lattice dislocations with grain boundaries in metals. Philosophical Magazine A 62 (1), 131–153.

Levine, I., 2009. Physical Chemistry, 6th Edition. McGraw-Hill Education, New York.

Li, Y., Bushby, A. J., Dunstan, D. J., 2016. The Hall-Petch effect as a manifestation of the general size effect. Proceedings of the Royal Society A: Mathematical, Physical and Engineering Sciences 472 (2190), 20150890.

Ling, C., Forest, S., Besson, J., Tanguy, B., Latourte, F., 2018. A reduced micromorphic single crystal plasticity model at finite deformations. Application to strain localization and void growth in ductile metals. International Journal of Solids and Structures 134, 43–69.

Liu, W., Liu, Y., Sui, H., Chen, L., Yu, L., Yi, X., Duan, H., 2020. Dislocation-grain boundary interaction in metallic materials: Competition between dislocation transmission and dislocation source activation. Journal of the Mechanics and Physics of Solids 145, 104158.

McBride, A., Bargmann, S., Reddy, B. D., 2015. A computational investigation of a model of single-crystal gradient thermoplasticity that accounts for the stored energy of cold work and thermal annealing. Computational Mechanics 55 (4), 755–769.

Mecking, H., Lücke, K., 1970. A new aspect of the theory of flow stress of metals. Scripta Metallurgica 4, 427–432.

Miehe, C., 2011. A multi-field incremental variational framework for gradient-extended standard dissipative solids. Journal of the Mechanics and Physics of Solids 59 (4), 898–923.

Miehe, C., Schröder, J., 2001. A comparative study of stress update algorithms for rate-independent and rate-dependent crystal plasticity. International Journal for Numerical Methods in Engineering 50 (2), 273–298.

Mindlin, R. D., 1964. Micro-structure in linear elasticity. Archive for Rational Mechanics and Analysis 16 (1), 51–78.

Moës, N., Dolbow, J., Belytschko, T., 1999. A finite element method for crack growth without remeshing. International Journal for Numerical Methods in Engineering 46 (1), 131–150.

Monavari, M., Zaiser, M., 2018. Annihilation and sources in continuum dislocation dynamics. Materials Theory 2 (1), 3.

Monneau, R., Patrizi, S., 2012. Homogenization of the Peierls-Nabarro model for dislocation dynamics. Journal of Differential Equations 253 (7), 2064–2105.

Motz, C., Weygand, D., Senger, J., Gumbsch, P., 2008. Micro-bending tests: A comparison between three-dimensional discrete dislocation dynamics simulations and experiments. Acta Materialia 56 (9), 1942–1955.

Mughrabi, H., 2001. Self-consistent experimental determination of the dislocation line tension and long-range internal stresses in deformed copper crystals by analysis of dislocation curvatures. Materials Science and Engineering: A 309-310, 237–245.

Müller, I., 1985. Thermodynamics. Interaction of Mechanics and Mathematics Series. Pitman, Boston.

Nabarro, F. R. N., 1997. Fifty-year study of the Peierls-Nabarro stress. Materials Science and Engineering: A 234-236, 67–76.

Nemat-Nasser, S., Hori, M., 1993. Micromechanics: Overall Properties of Heterogeneous Materials. North Holland, Amsterdam.

Ohmura, T., Tsuzaki, K., 2007. Plasticity initiation and subsequent deformation behavior in the vicinity of single grain boundary investigated through nanoindentation technique. Journal of Materials Science 42 (5), 1728–1732.

Ohno, N., Okumura, D., Shibata, T., 2008. Grain-size dependent yield behavior under loading, unloading and reverse loading. International Journal of Modern Physics B 22, 5937–5942.

Orowan, E., 1934. Zur Kristallplastizität. III. Zeitschrift für Physik 89 (9), 634–659.

Ortiz, M., Repetto, E. A., 1999. Nonconvex energy minimization and dislocation structures in ductile single crystals. Journal of the Mechanics and Physics of Solids 47 (2), 397–462.

Osher, S., Fedkiw, R. P., 2001. Level set methods: An overview and some recent results. Journal of Computational Physics 169 (2), 463–502.

Osher, S., Sethian, J. A., 1988. Fronts propagating with curvature-dependent speed: Algorithms based on Hamilton-Jacobi formulations. Journal of Computational Physics 79 (1), 12–49.

Özdemir, İ., Yalçinkaya, T., 2014. Modeling of dislocation-grain boundary interactions in a strain gradient crystal plasticity framework. Computational Mechanics 54 (2), 255–268.

Palm, J. H., 1951. Stress-strain relations for uniform monotonic deformation under triaxial loading. Applied Scientific Research 2 (1), 54.

Peng, X.-L., Huang, G.-Y., Bargmann, S., 2019. Gradient crystal plasticity: A grain boundary model for slip transmission. Materials 12 (22), 3761.

Polanyi, M., 1934. Über eine Art Gitterstörung, die einen Kristall plastisch machen könnte. Zeitschrift für Physik 89 (9), 660–664.

Prahs, A., Böhlke, T., 2020a. On interface conditions on a material singular surface. Continuum Mechanics and Thermodynamics 32 (5), 1417–1434.

Prahs, A., Böhlke, T., 2020b. On invariance properties of an extended energy balance. Continuum Mechanics and Thermodynamics 32 (3), 843–859.

Prahs, A., Böhlke, T., 2022. The role of dissipation regarding the concept of purely mechanical theories in plasticity. Mechanics Research Communications 119, 103832.

Reddy, B. D., 2011. The role of dissipation and defect energy in variational formulations of problems in strain-gradient plasticity. Part 2: Single-crystal plasticity. Continuum Mechanics and Thermodynamics 23 (6), 551.

Sandfeld, S., Thawinan, E., Wieners, C., 2015. A link between microstructure evolution and macroscopic response in elasto-plasticity: Formulation and numerical approximation of the higher-dimensional continuum dislocation dynamics theory. International Journal of Plasticity 72, 1–20.

Schmid, E., Boas, W., 1935. Kristallplastizität: Mit Besonderer Berücksichtigung der Metalle. Springer, Berlin Heidelberg.

Schulz, K., Sudmanns, M., Gumbsch, P., 2017. Dislocation-density based description of the deformation of a composite material. Modelling and Simulation in Materials Science and Engineering 25 (6), 064003.

Sedláček, R., Forest, S., 2000. Non-local plasticity at microscale: A dislocation-based and a Cosserat model. Physica Status Solidi (B) 221 (2), 583–596.

Shi, J., Zikry, M. A., 2011. Modeling of grain boundary transmission, emission, absorption and overall crystalline behavior in $\Sigma 1$, $\Sigma 3$, and $\Sigma 17b$ bicrystals. Journal of Materials Research 26 (14), 1676–1687.

Simo, J. C., Hughes, T. J. R., 1998. Computational Inelasticity. Interdisciplinary Applied Mathematics 7. Springer, New York.

Simone, A., Duarte, C. A., Van der Giessen, E., 2006. A generalized finite element method for polycrystals with discontinuous grain boundaries. International Journal for Numerical Methods in Engineering 67 (8), 1122–1145.

Slattery, J. C., 1990. Interfacial Transport Phenomena, 2nd Edition. Springer, New York.

Soer, W. A., Aifantis, K. E., De Hosson, J. T. M., 2005. Incipient plasticity during nanoindentation at grain boundaries in body-centered cubic metals. Acta Materialia 53 (17), 4665–4676.

Soer, W. A., De Hosson, J. T. M., 2005. Detection of grain-boundary resistance to slip transfer using nanoindentation. Materials Letters 59 (24), 3192–3195.

Spearot, D. E., Sangid, M. D., 2014. Insights on slip transmission at grain boundaries from atomistic simulations. Current Opinion in Solid State and Materials Science 18 (4), 188–195.

Sun, S., Adams, B., Shet, C., Saigal, S., King, W., 1998. Mesoscale investigation of the deformation field of an aluminum bicrystal. Scripta Materialia 39, 501–508.

Sun, S., Adams, B. L., King, W. E., 2000. Observations of lattice curvature near the interface of a deformed aluminium bicrystal. Philosophical Magazine A 80 (1), 9–25.

Svendsen, B., 2002. Continuum thermodynamic models for crystal plasticity including the effects of geometrically-necessary dislocations. Journal of the Mechanics and Physics of Solids 50 (6), 1297–1329.

Taylor, G. I., 1934. The mechanism of plastic deformation of crystals. Part I. - Theoretical. Proceedings of the Royal Society of London A: Mathematical, Physical and Engineering Sciences 145 (855), 362–387.

Wang, M. G., Ngan, A. H. W., 2004. Indentation strain burst phenomenon induced by grain boundaries in niobium. Journal of Materials Research 19 (8), 2478–2486.

Werner, E., Prantl, W., 1990. Slip transfer across grain and phase boundaries. Acta Metallurgica et Materialia 38 (3), 533–537.

Wilkens, M., 1969. Das mittlere Spannungsquadrat $\langle\sigma\rangle$ begrenzt regellos verteilter Versetzungen in einem zylinderförmigen Körper. Acta Metallurgica 17 (9), 1155–1159.

Wo, P. C., Ngan, A. H. W., 2004. Investigation of slip transmission behavior across grain boundaries in polycrystalline Ni3Al using nanoindentation. Journal of Materials Research 19 (1), 189–201.

Wulfinghoff, S., Bayerschen, E., Böhlke, T., 2013. A gradient plasticity grain boundary yield theory. International Journal of Plasticity 51, 33–46.

Wulfinghoff, S., Böhlke, T., 2012. Equivalent plastic strain gradient enhancement of single crystal plasticity: Theory and numerics. Proceedings of the Royal Society A: Mathematical, Physical and Engineering Sciences 468 (2145), 2682–2703.

Wulfinghoff, S., Böhlke, T., 2015. Gradient crystal plasticity including dislocation-based work-hardening and dislocation transport. International Journal of Plasticity 69, 152–169.

Wulfinghoff, S., Forest, S., Böhlke, T., 2015. Strain gradient plasticity modeling of the cyclic behavior of laminate microstructures. Journal of the Mechanics and Physics of Solids 79, 1–20.

Xiang, Y., 2009. Continuum approximation of the Peach-Koehler force on dislocations in a slip plane. Journal of the Mechanics and Physics of Solids 57 (4), 728–743.

Yang, B., Motz, C., Rester, M., Dehm, G., 2012. Yield stress influenced by the ratio of wire diameter to grain size - a competition between the effects of specimen microstructure and dimension in micro-sized polycrystalline copper wires. Philosophical Magazine 92 (25-27), 3243–3256.

Zaiser, M., 2015. Local density approximation for the energy functional of three-dimensional dislocation systems. Physical Review B 92, 174120.

Zhu, T. T., Bushby, A. J., Dunstan, D. J., 2008. Materials mechanical size effects: A review. Materials Technology 23 (4), 193–209.

Zhu, Y., Xiang, Y., 2015. A continuum model for dislocation dynamics in three dimensions using the dislocation density potential functions and its application to micro-pillars. Journal of the Mechanics and Physics of Solids 84, 230–253.

Schriftenreihe Kontinuumsmechanik im Maschinenbau
Karlsruher Institut für Technologie (KIT)
(ISSN 2192-693X)

Band 1 Felix Fritzen
Microstructural modeling and computational homogenization of the physically linear and nonlinear constitutive behavior of micro-heterogeneous materials.
ISBN 978-3-86644-699-1

Band 2 Rumena Tsotsova
Texturbasierte Modellierung anisotroper Fließpotentiale.
ISBN 978-3-86644-764-6

Band 3 Johannes Wippler
Micromechanical finite element simulations of crack propagation in silicon nitride.
ISBN 978-3-86644-818-6

Band 4 Katja Jöchen
Homogenization of the linear and non-linear mechanical behavior of polycrystals.
ISBN 978-3-86644-971-8

Band 5 Stephan Wulfinghoff
Numerically Efficient Gradient Crystal Plasticity with a Grain Boundary Yield Criterion and Dislocation-based Work-Hardening.
ISBN 978-3-7315-0245-6

Band 6 Viktor Müller
Micromechanical modeling of short-fiber reinforced composites.
ISBN 978-3-7315-0454-2

Die Bände sind unter www.ksp.kit.edu als PDF frei verfügbar oder als Druckausgabe bestellbar.

Band 7 Florian Rieger
Work-hardening of dual-phase steel.
ISBN 978-3-7315-0513-6

Band 8 Vedran Glavas
Micromechanical Modeling and Simulation of Forming Processes.
ISBN 978-3-7315-0602-7

Band 9 Eric Bayerschen
Single-crystal gradient plasticity with an accumulated plastic slip: Theory and applications.
ISBN 978-3-7315-0606-5

Band 10 Bartholomäus Brylka
Charakterisierung und Modellierung der Steifigkeit von langfaserverstärktem Polypropylen.
ISBN 978-3-7315-0680-5

Band 11 Rudolf Neumann
Two-Scale Thermomechanical Simulation of Hot Stamping.
ISBN 978-3-7315-0714-7

Band 12 Mauricio Lobos Fernández
Homogenization and materials design of mechanical properties of textured materials based on zeroth-, first- and second-order bounds of linear behavior.
ISBN 978-3-7315-0770-3

Band 13 Malte Schemmann
Biaxial Characterization and Mean-field Based Damage Modeling of Sheet Molding Compound Composites.
ISBN 978-3-7315-0818-2

Band 14 Jürgen Albiez
Finite element simulation of dislocation based plasticity and diffusion in multiphase materials at high temperature.
ISBN 978-3-7315-0918-9

Band 15 Maria Loredana Kehrer
Thermomechanical Mean-Field Modeling and Experimental Characterization of Long Fiber-Reinforced Sheet Molding Compound Composites.
ISBN 978-3-7315-0924-0

Band 16 Peter Hölz
A dynamic and statistical analysis of the temperature- and fatigue behavior of a race power unit – The effect of different thermodynamic states.
ISBN 978-3-7315-0988-2

Band 17 Andreas Prahs
A Gradient Crystal Plasticity Theory Based on an Extended Energy Balance.
ISBN 978-3-7315-1025-3

Band 18 Johannes Ruck
Modeling martensitic phase transformation in dual phase steels based on a sharp interface theory.
ISBN 978-3-7315-1072-7

Band 19 Hannes Erdle
Modeling of Dislocation - Grain Boundary Interactions in Gradient Crystal Plasticity Theories.
ISBN 978-3-7315-1196-0

The formulation and implementation of novel material models on the micro-scale of polycrystalline materials gives a deeper understanding of inner- and inter-crystalline effects. In this work a physically-based dislocation theory of plasticity is derived within an extended continuum mechanical context. With an analytical solution of a three-phase periodic laminate the dislocation pile-up at grain boundaries and dislocation transmission through the grain boundaries is investigated, which is of special interest during the plastic deformation of metal materials. It is shown that in contrary to the common approach of grain boundary modeling the introduced grain boundary flow rule passes the single crystal consistency check for the limit case of coinciding slip systems. For the finite element implementation, numerically efficient approaches are introduced based on accumulated field variables. The evolving distributions of plastic slip and dislocation density are consistent to experimental observations and show the importance of energy expressions and flow rules based on underlying dislocation theories for the modeling of dislocation-grain boundary interactions.

ISSN 2192-693X
ISBN 978-3-7315-1196-0

Gedruckt auf FSC-zertifiziertem Papier

ISBN 978-3-7315-1196-0
9 783731 511960 >